An Examination of Satellite-Based Cropland Canopy Water Content Maps for Yield Ratio Prediction

A Dissertation
Presented in Partial Fulfillment of the Requirements for the
Degree of Doctor of Philosophy
with a
Major in Natural Resources
in the
College of Graduate Studies
University of Idaho
by
Erik J. Boren

Approved by:
Major Professor: Luigi Boschetti, Ph.D.
Committee Members: Dan Johnson, Ph.D.; Jan Eitel, Ph.D.; Paul Gessler, Ph.D.
Department Administrator: Charles Goebel, Ph.D.

December 2021

Abstract

While difficult to characterize, drought has been defined as a period of water shortage compared to normal conditions. Soil water availability has a larger impact on agricultural productivity than any other abiotic factor. It is critical to develop research which tracks the spatial and temporal patterns of drought as droughts become more frequent and severe, particularly in regions of high agricultural productivity. Traditional drought monitoring indices are based on point measurements of weather conditions from weather station instruments, which increase in uncertainty when extrapolating the measurements to spatially delineate the drought event, especially in data sparse regions. Satellite-based measurements, such as rainfall, evapotranspiration (ET), soil moisture, or vegetation health have increased in use to gap-fill the uncertainty from point-based measurements and increase the scale of drought monitoring. The spatial and temporal requirements for farm-level agricultural monitoring, however, create challenges when implementing remote sensing technology for drought and yield monitoring.

The research in this dissertation proposes a transferable method for using moderate resolution satellite imagery in physical-based radiative transfer model (RTM) inversion methods for retrieving cropland canopy water content (CCWC) as a direct indicator of crop water status for predicting yield. The method aims to alleviate the "ill-posed" nature of inversion problem solving by using phenology and crop species *a priori* information to dynamically constrain the inversion of the RTM, PRO4SAIL, for estimating CCWC at the 30-m pixel level. The 30-m CCWC product is integrated into a framework for predicting drought stress and yield loss by combining a previously published relationship between leaf water content (LWC) and available soil water content (ASWC) with the crop water use definitions outlined in Food and Agriculture Organization (FAO) Irrigation and Drainage paper 56 .

The leaf structure parameter (N_s) accounts for a large proportion of uncertainty in PRO4SAIL inversion problems as it is the only biophysical parameter that is not physically measurable. Chapter 1 examined whether there is statistically significant variation in N_s as a function of phenology, crop species type, and water status with the purpose of generating reference values of N_s to be used as *a priori* information in subsequent research. A total of 230 spectral measurements were taken from three monocotyledon species (hard red wheat, soft white wheat, and upland rice) and one dicotyledon species (soy) over two full growth seasons at the University of Idaho Pitkin's Nursery. The spectral measurements were used to characterize N_s over phenology, crop species type, and water status. The study demonstrated that a significant relationship exists between phenology and N_s as well as a significant relationship between crop species type and N_s. No significant relationship was found

between the water treatments of the study and N_s , providing evidence that water status and N_s are independent.

In chapter 2, a novel PRO4SAIL inversion approach was proposed and tested using the Harmonized Landsat-Sentinel (HLS) surface reflectance product to estimate CCWC in wheat, barley, and garbanzo fields outside of Genesee, Idaho over three growing seasons. The inversion strategy used information about phenology and crop species to generate a set of Look-up Tables (LUTs) for each overpass date. A set of 225 leaf measurements were used to train the LUTs, and 102 independent field measurements were used to validate the inversion. The novel crop and time dependent strategy had the best performance when compared to a phenology specific LUT strategy, and single nominal range LUT inversion strategy. The results showed the potential of an operational HLS-based CCWC product which may serve as the basis for further improvement.

Chapter 3 presents a study which examines the feasibility of using a satellite derived time series of CCWC to predict the yield ratio in maize, defined as the ratio between actual harvested yield and maximum potential yield. The paper establishes the relationships between CCWC, drought stress, and yield ratio by combining a logistic relationship between LWC and ASWC with FAO-56 definitions of water balance, drought, and yield. Using these definitions, and known relationships between PRO4SAIL biophysical parameters, CCWC, NDVI, and yield ratio were modeled for different treatments of an independent irrigation experiment which created late drought conditions in Inner Mongolia, China. Coincident Landsat-8 Operational Land Imager (OLI) scenes were used to create the PRO4SAIL estimated CCWC and observed NDVI time series. The results demonstrated the first steps towards s farm-level yield ratio prediction using physical-based estimation of CCWC with FAO-56 soil water balance methods. The implications of the study highlight a potential for using CCWC in yield ratio prediction and justify future field-level irrigation treatment research with ground measured yield for testing the CCWC-yield relationship.

Acknowledgements

I would like to thank my major advisor, Dr. Luigi Boschetti, for all his support, patience, and the opportunity to be under his mentorship; Dr. Dan Johnson for his insights, paper contributions, and encouragement; and Dr. Jan Eitel and Dr. Paul Gessler, for their support and advice.

I would also like to thank all the those who mentored me throughout my professional career while pursuing my graduate studies including Dr. Jessica McCarty and Dr. Valeriy Kovalskyy. I cannot wait to pay it forward!

Dedication

I would like to dedicate this to my wife, Claire. This would not have been possible without her support and strength.

Table of Contents

List of Tables

List of Figures

Statement of Contribution

Chapter 1: Published in *Remote Sensing* as:

Boren, E.J., Boschetti, L. and Johnson, D.M., 2019. Characterizing the variability of the structure parameter in the PROSPECT leaf optical properties model. Remote Sensing, 11(10), p.1236.

E.J.B. and L.B. conceived the experiments; E.J.B. collected the experimental dataset and performed the data analysis; E.J.B. structured and drafted the manuscript with assistance from L.B. and D.M.J.

Chapter 2: Published in *Remote Sensing* as:

Boren, E.J. and Boschetti, L., 2020. Landsat-8 and Sentinel-2 Canopy Water Content Estimation in Croplands through Radiative Transfer Model Inversion. Remote Sensing, 12(17), p.2803.

Conceptualization, E.J.B. and L.B.; methodology, E.J.B. and L.B.; software, E.J.B.; validation, E.J.B.; formal analysis, E.J.B.; investigation, E.J.B.; resources, L.B.; data curation, E.J.B.; writing—original draft preparation, E.J.B.; and writing—review and editing, L.B.; All authors have read and agreed to the published version of the manuscript.

Introduction

Water is a vital component in all plant physiological processes, including photosynthesis, nutrient transportation, transpiration, and cellular growth. These processes are tailored to the specific climatic regimes unique to the plant's region for increasing survivability and competitiveness. Deficit in water availability may induce stress responses to mitigate the impact of water scarcity, such as constrained plant growth and cellular metabolism, while an overabundance of water creates anoxic conditions which limit plant physiological processes and promotes disease.

The availability of water restricts terrestrial plant productivity more than any other factor (Lambers et al. 2008). In the context of agriculture, drought-induced crop losses exceed losses by all other factors combined (Boyer 1982). The simplest definition of drought is a period where a deficit of water is experienced relative to normal conditions (Lloyd-Hughes 2014). In agriculture, drought represents a deficit in available soil water content for uptake by the crops which results in yield reductions or failure. This is especially important in vulnerable agricultural regions where food security and primary source of income are dependent on agricultural yield. Increasing food demands driven by a growing population is intensified by limited water supply needed for agricultural use (Amprako 2016; Somerville and Briscoe 2001). Increasing weather pattern variability brought on by climate change, resulting in more frequent and severe occurrences of extreme heat and drought are projected to increase during the twenty first century over most of the global land surface, with a global increase of 1.5˚C resulting in double the frequency of 50-year drought events over 58% of the land surface (Gu et al. 2020). A drying trend has also been observed in central equatorial Africa where rainfall associated with the observed growing seasons decreased by 20% from 1983-2012 (Diem et al. 2014). Given that the latest IPCC report project rising temperatures and shifting regional precipitation in the coming decades as a result of global climate change (Kirtman et al. 2013), research that seeks to improve scalable drought monitoring for yield loss prediction is of paramount importance.

Droughts are characterized as being difficult to quantify and analyze due to their slow development and prolonged impacts (West et al. 2019). Up until the end of the 20th century, drought monitoring approaches were primarily based on computed indices like the Palmer Drought Severity Index (PDSI; Palmer (1965)) and Standardized Precipitation Index (SPI; McKee et al. (1993)) using in-situ station measurements of key meteorological variables. The difficulty of in-situ station data for capturing the complex dynamics and heterogeneity of drought events in data sparse regions, coupled with recent advancements in remote sensing technology, and increasing richness of Earth observation (EO) data, remote sensing has become a viable solution for monitoring key drought-related variables over larger temporal and spatial scales than what was previously possible. Common types of remote

sensing datasets used for drought monitoring include rainfall (e.g. (Hou et al. 2014; Islam and Uyeda 2007; Kummerow et al. 1998)), evapotranspiration (e.g. (Miralles et al. 2011; Van Dijk et al. 2018; Vinukollu et al. 2011)), soil moisture (e.g. (Eswar et al. 2018; Martínez-Fernández et al. 2016)), and vegetation health response to drought conditions (e.g. (Ahmed et al. 2017; Kogan and Sullivan 1993; Wang et al. 2007)).

Still, the temporal and spatial resolutions of remote sensing datasets are often inadequate for agricultural monitoring (Whitcraft et al. 2015b). Temporal resolution is an important consideration, since droughts are not only complex in both the timeline of their initialization and duration (Parry et al. 2016), but the timing of a drought event relative to the crops' phenology, which rapidly changes throughout the season, is extremely significant when monitoring for yield prediction (Sah et al. 2020; Steduto et al. 2012). As a result, yield prediction requires one clear observation made at least biweekly throughout the growing season (Johnson 2014; Zaks and Kucharik 2011). Due to this requirement, a tradeoff decision is often made to use data with coarse spatial resolution (Lavender and Lavender 2015), defined by the Global Agricultural Monitoring Community (GEOGLAM) as greater than 100 m (Whitcraft et al. 2015a). For example, the Tropical Rainfall Measuring Mission (TRMM) microwave precipitation radar (Kummerow et al. 1998) and Global Precipitation Measurement (GPM) mission (Hou et al. 2014) are able to be combined to generate sub-daily rainfall estimates at 0.1 - 0.25 degree spatial resolution and makes up a significant dataset used in global rainfall and drought pattern studies (e.g. (Alizadeh and Nikoo 2018; Zhang et al. 2017)). Both active and passive instruments may also be used to derive surface soil moisture conditions, such as the Soil Moisture and Ocean Salinity (SMOS) (Kerr et al. 2010), Soil Moisture Active Passive (SMAP) (Entekhabi et al. 2010), or Advanced Microwave Scanning Radiometer – Earth Observing System (AMSR-E) (Njoku et al. 2003), at revisit frequencies ranging from 2 to 3 days and spatial resolutions ranging from 3 to 50 km. Passive multispectral observations at 250-500 m from MODIS-class sensor also have an excellent temporal resolution of two images every day and have traditionally been the primary data source for computing indices related to vegetation health (e.g. (Duveiller et al. 2011; Pan et al. 2012)). Coarse resolution datasets like these, however, are often inadequate due to issues from sub-pixel heterogeneity within agricultural landscapes (Duveiller and Defourny 2010).

Multispectral EO data are continuing to become more available at the moderate spatial resolution (defined by GEOGLAM as 10 - 100 m) scale suitable for crop monitoring applications (Duveiller and Defourny 2010; West et al. 2019; Whitcraft et al. 2015a). The successful launch of the Landsat-8 Operational Land Imager (OLI) in 2012, Sentinel-2A Multi-Spectral Instrument (MSI) in 2015, and Sentinel-2B MSI in 2017, the systematic acquisition schedule and free data distribution

policy of both missions provide the opportunity for measurements at a spatial and temporal scale that can meet the demands of potential operational users: combined, these polar-orbiting systems provide 10 m to 30 m multi-spectral global coverage up to every 2-3 days (Whitcraft et al. 2015a). The launch of Landsat-9 OLI-2 (Masek et al. 2020) in 2021 and Sentinel-2C MSI (Toulemont et al. 2019) scheduled for 2024 further enable the envisioning of an operational agricultural monitoring system (Fritz et al. 2019), thereby lessening the challenges related to resolution when using remote sensing technology.

Most common approaches to crop yield forecasting are based on empirical regression models using multispectral EO-derived vegetation indices inputs like maximum Normalized Difference Vegetation Index (NDVI) (Tucker 1979) over the season (Becker-Reshef et al. 2010) or temporal NDVI integration (Doraiswamy et al. 2005; Meroni et al. 2013). Since NDVI is sensitive to changes in photosynthetic activity, vegetation health, and vegetation abundance, NDVI is thought to reflect the variables affecting crop distress and production (Chantarat et al. 2009; Rowley et al. 2007). NDVI has been found to correlate well with precipitation, extreme heat, and yield in a number of regional experiments (Carter 2009; Chantarat et al. 2009; Ward et al. 2008), however, a study which examined the relationships between yield and NDVI over 60 locations between 1982 and 2003 found the relationships were inconsistent and highly dependent on location specific characteristics (Turvey and Mclaurin 2012). The relationship between NDVI and yield is also known to be weakened during seasons with ideal conditions during early growth stages, which create full establishment of vegetation, and drought conditions after full development during reproductive stages (Rowley et al. 2007). Challenges with the transferability of remote sensing methods typically arise when relationships from empirical approaches are highly dependent upon field sampling methods, imagery preprocessing quality, statistical model chosen and when the measurements used to characterize the relationship are not representative of the target region (Grossman et al. 1996; Li and Wang 2011; Yebra et al. 2013).

The biophysical parameter, cropland canopy water content (CCWC), defined as the total amount of water stored in the canopy per unit ground area [g m^{-2}], has successfully been estimated to provide agricultural producers cost-effective key knowledge for improving production capacity and resiliency in agricultural systems (Anderson et al. 2016; Yi et al. 2014; Zhang and Zhou 2019). CCWC has an advantage over NDVI in that, because it represents the physical quantity of water in the canopy, it may be estimated through physical-based radiative transfer model (RTM) inversion methods to alleviate the transferability challenge inherit with empirical methods (Cernicharo et al. 2013; Gerber et al. 2011; Jurdao et al. 2013) and represents a more direct estimate of the crop's water status. RTMs describe the absorption, emission, and scattering processes of radiation through a medium with known physical properties. Due to the physical nature of the approach, the technique has the advantage of

transferability over empirical-based approaches (Fourty et al. 1996; Liang et al. 2015; Schlerf and Atzberger 2006). The combination of leaf model, Propriétés Spectrales (PROSPECT) (Jacquemoud and Baret 1990), and canopy model, the Scattering by Arbitrary Inclined Leaves (4SAIL) (Verhoef 1984), have been successfully coupled, PRO4SAIL (Jacquemoud et al. 2009), and inverted using remotely sensed data to retrieve biophysical and canopy parameter estimates (Croft et al. 2015; Darvishzadeh et al. 2008; Jacquemoud et al. 2009; Vohland et al. 2010).

RTM inversion is achieved by minimizing the difference between the observed and modeled spectra: the biophysical values used for generating the modeled spectra with the minimum difference to the observed spectra are assigned as the values retrieved. Since very similar reflectance spectra can be obtained from a range of biophysical parameters with different combinations, the inversion problem has been referred to as being an "ill-posed" problem (Baret and Buis 2008; Combal et al. 2003; Yebra and Chuvieco 2009). The leaf structure parameter (N_s), a hypothetical parameter in the PROSPECT RTM relating to the number of plates in the conceptual plate model within PROSPECT (Allen et al. 1969), has been cited as the parameter with highest uncertainty since it is the only parameter with no measurable physical trait (Ceccato et al. 2001; Ollinger 2011). Combal et al. (2003) recommended the use of *a priori* information to alleviate the "ill-posed" problem. Several studies have reported significant improvements to biophysical parameter retrieval using *a priori* information to constrain the approach (Danson and Bowyer 2004; Koetz et al. 2005; Lavergne et al. 2007). Still, the need to advance knowledge of uncertainties related to measurements and modeling exists, especially with the relationships between N_s , species, stress, and phenology, as it would improve the quality and application of *a priori* information (Combal et al. 2003; Laurent et al. 2014; Qu et al. 2008).

The remaining challenge of transferring a physical-based CCWC estimates for informing yield prediction models requires an investigation into the link between CCWC and yield. While limited, the existing research which aims to inform agricultural managers about yield using remotely sensed CCWC, retrieved through either empirical or physical-based methods, still rely on empirical relationships between drought stress, yield, and CCWC (Elmetwalli et al. 2020; Mwinuka et al. 2021) which may not transfer effectively across a diverse range of locations or crops. This is especially true when phenology is not considered since water stress during various phenological stages has different impacts on crop growth, development, and yield for various crops (Sah et al. 2020; Steduto et al. 2012; Yavuz et al. 2021). It is imperative that a connection be made and explored between the physical quantity of water in the canopy to drought stress and yield.

This research proposes a new approach to estimating the yield loss ratio using CCWC estimates derived from RTM inversion of moderate resolution multi-spectral EO data. The first objective of the

dissertation was to characterize the relationship of the N_s parameter in PROSPECT with phenology, species type, and leaf water status. To our knowledge, no other study has examined the relationship between the N_s parameter phenology and leaf water status, which are both critical leaf state information for the main thesis objective of estimate a yield loss ratio. The lessons from the first objective will be considered and applied to subsequent components of the dissertation. The second objective was to use the 30-m Harmonized Landsat-Sentinel (HLS) multispectral EO product (Claverie et al. 2018) as the input in PRO4SAIL inversion for CCWC estimation. The HLS product, which combines Landsat-8 and Sentinel-2 observations, offers strong temporal and spatial resolutions for monitoring agricultural landscapes. The HLS product has not been evaluated for CCWC estimation through RTM inversion over the entire growing season of multiple years. Lastly, the third objective of the dissertation was to transfer the CCWC estimation methods from the second objective to another study region with known water balance information (Zhang et al. 2019) and examine a new method which exploits a previously published relationship between leaf water content and soil water content (Zhou et al. 2021) and using the Food and Agriculture Organization (FAO) Irrigation and Drainage paper 56 yield ratio prediction equations (Allen et al. 1998) for estimating the yield loss of crops in the study throughout the growing season. Combined, the dissertation presents the first steps towards a new approach to estimating yield ratio changes from physical-based and moderate spatial resolution EO-data derived CCWC.

To this end, the dissertation is divided into three chapters that develop the three main goals of the research: 1) assess whether there is a statistically significant variation in N_s as a function of phenology and water status, and to provide reference values of N_s to be used as *a priori* information for the inversion of PRO4SAIL in subsequent research; 2) propose and test a phenology driven methodology for the generation of a multi-temporal CCWC product from the time series of HLS reflectances, through look-up table (LUT) inversion of PRO4SAIL; and 3) estimate the yield loss ratio of a previously published irrigation experiment using the CCWC estimation methods from the second objective and an logistic regression model linking CCWC to soil water content (Zhou et al. 2021) which can be used as the input to FAO-56 yield ratio equations (Allen et al. 1998) for predicting yield.

References

Ahmed, M., Else, B., Eklundh, L., Ardö, J., & Seaquist, J. (2017). Dynamic response of NDVI to soil moisture variations during different hydrological regimes in the Sahel region. *International Journal of Remote Sensing, 38*, 5408-5429

Alizadeh, M.R., & Nikoo, M.R. (2018). A fusion-based methodology for meteorological drought estimation using remote sensing data. *Remote sensing of environment, 211*, 229-247

Allen, R.G., Pereira, L.S., Raes, D., & Smith, M. (1998). FAO Irrigation and drainage paper No. 56. *Rome: Food and Agriculture Organization of the United Nations, 56*, e156

Allen, W.A., Gausman, H.W., Richardson, A.J., & Thomas, J.R. (1969). Interaction of isotropic light with a compact plant leaf. *JOSA, 59*, 1376-1379

Amprako, J.L. (2016). The United Nations World Water Development Report 2015. *Future of Food: Journal on Food, Agriculture and Society, 4*, 64-65

Anderson, M.C., Zolin, C.A., Sentelhas, P.C., Hain, C.R., Semmens, K., Yilmaz, M.T., Gao, F., Otkin, J.A., & Tetrault, R. (2016). The Evaporative Stress Index as an indicator of agricultural drought in Brazil: An assessment based on crop yield impacts. *Remote sensing of environment, 174*, 82-99

Baret, F., & Buis, S. (2008). Estimating canopy characteristics from remote sensing observations: Review of methods and associated problems. *Advances in land remote Sensing* (pp. 173-201): Springer

Becker-Reshef, I., Vermote, E., Lindeman, M., & Justice, C. (2010). A generalized regression-based model for forecasting winter wheat yields in Kansas and Ukraine using MODIS data. *Remote sensing of environment, 114*, 1312-1323

Boyer, J.S. (1982). Plant productivity and environment. *Science, 218*, 443-448

Carter, M. (2009). Innovations in insuring the poor: Intelligent design of index insurance for smallholder farmers and pastoralists. 2020 Vision Focus Brief 17 (6). *IFPRI, Washington DC*

Ceccato, P., Flasse, S., Tarantola, S., Jacquemoud, S., & Grégoire, J.-M. (2001). Detecting vegetation leaf water content using reflectance in the optical domain. *Remote sensing of environment, 77*, 22-33

Cernicharo, J., Verger, A., & Camacho, F. (2013). Empirical and physical estimation of canopy water content from CHRIS/PROBA data. *Remote Sensing, 5*, 5265-5284

Chantarat, S., Mude, A.G., Barrett, C.B., & Turvey, C.G. (2009). The performance of index based livestock insurance: Ex ante assessment in the presence of a poverty trap. *Available at SSRN 1844751*

Claverie, M., Ju, J., Masek, J.G., Dungan, J.L., Vermote, E.F., Roger, J.-C., Skakun, S.V., & Justice, C. (2018). The Harmonized Landsat and Sentinel-2 surface reflectance data set. *Remote sensing of environment, 219*, 145-161

Combal, B., Baret, F., Weiss, M., Trubuil, A., Mace, D., Pragnere, A., Myneni, R., Knyazikhin, Y., & Wang, L. (2003). Retrieval of canopy biophysical variables from bidirectional reflectance: Using prior information to solve the ill-posed inverse problem. *Remote sensing of environment, 84*, 1-15

Croft, H., Chen, J., Zhang, Y., Simic, A., Noland, T., Nesbitt, N., & Arabian, J. (2015). Evaluating leaf chlorophyll content prediction from multispectral remote sensing data within a physically-based modelling framework. *ISPRS Journal of Photogrammetry and Remote Sensing, 102*, 85-95

Danson, F., & Bowyer, P. (2004). Estimating live fuel moisture content from remotely sensed reflectance. *Remote sensing of environment, 92*, 309-321

Darvishzadeh, R., Skidmore, A., Schlerf, M., & Atzberger, C. (2008). Inversion of a radiative transfer model for estimating vegetation LAI and chlorophyll in a heterogeneous grassland. *Remote sensing of environment, 112*, 2592-2604

Diem, J.E., Ryan, S.J., Hartter, J., & Palace, M.W. (2014). Satellite-based rainfall data reveal a recent drying trend in central equatorial Africa. *Climatic change, 126*, 263-272

Doraiswamy, P.C., Sinclair, T.R., Hollinger, S., Akhmedov, B., Stern, A., & Prueger, J. (2005). Application of MODIS derived parameters for regional crop yield assessment. *Remote sensing of environment, 97*, 192-202

Duveiller, G., Baret, F., & Defourny, P. (2011). Crop specific green area index retrieval from MODIS data at regional scale by controlling pixel-target adequacy. *Remote sensing of environment, 115*, 2686-2701

Duveiller, G., & Defourny, P. (2010). A conceptual framework to define the spatial resolution requirements for agricultural monitoring using remote sensing. *Remote sensing of environment, 114*, 2637-2650

Elmetwalli, A.H., El-Hendawy, S., Al-Suhaibani, N., Alotaibi, M., Tahir, M.U., Mubushar, M., Hassan, W.M., & Elsayed, S. (2020). Potential of hyperspectral and thermal proximal sensing for estimating growth performance and yield of soybean exposed to different drip irrigation regimes under arid conditions. *Sensors, 20*, 6569

Entekhabi, D., Njoku, E.G., O'Neill, P.E., Kellogg, K.H., Crow, W.T., Edelstein, W.N., Entin, J.K., Goodman, S.D., Jackson, T.J., & Johnson, J. (2010). The soil moisture active passive (SMAP) mission. *Proceedings of the IEEE, 98*, 704-716

Eswar, R., Das, N.N., Poulsen, C., Behrangi, A., Swigart, J., Svoboda, M., Entekhabi, D., Yueh, S., Doorn, B., & Entin, J. (2018). SMAP soil moisture change as an indicator of drought conditions. *Remote Sensing, 10*, 788

Fourty, T., Baret, F., Jacquemoud, S., Schmuck, G., & Verdebout, J. (1996). Leaf optical properties with explicit description of its biochemical composition: direct and inverse problems. *Remote sensing of environment, 56*, 104-117

Fritz, S., See, L., Bayas, J.C.L., Waldner, F., Jacques, D., Becker-Reshef, I., Whitcraft, A., Baruth, B., Bonifacio, R., & Crutchfield, J. (2019). A comparison of global agricultural monitoring systems and current gaps. *Agricultural Systems, 168*, 258-272

Gerber, F., Marion, R., Olioso, A., Jacquemoud, S., Da Luz, B.R., & Fabre, S. (2011). Modeling directional–hemispherical reflectance and transmittance of fresh and dry leaves from 0.4 μm to 5.7 μm with the PROSPECT-VISIR model. *Remote sensing of environment, 115*, 404-414

Grossman, Y., Ustin, S., Jacquemoud, S., Sanderson, E., Schmuck, G., & Verdebout, J. (1996). Critique of stepwise multiple linear regression for the extraction of leaf biochemistry information from leaf reflectance data. *Remote sensing of environment, 56*, 182-193

Gu, L., Chen, J., Yin, J., Sullivan, S.C., Wang, H.-M., Guo, S., Zhang, L., & Kim, J.-S. (2020). Projected increases in magnitude and socioeconomic exposure of global droughts in 1.5 and 2° C warmer climates. *Hydrology and Earth System Sciences, 24*, 451-472

Hou, A.Y., Kakar, R.K., Neeck, S., Azarbarzin, A.A., Kummerow, C.D., Kojima, M., Oki, R., Nakamura, K., & Iguchi, T. (2014). The global precipitation measurement mission. *Bulletin of the American Meteorological Society, 95*, 701-722

Islam, M.N., & Uyeda, H. (2007). Use of TRMM in determining the climatic characteristics of rainfall over Bangladesh. *Remote sensing of environment, 108*, 264-276

Jacquemoud, S., & Baret, F. (1990). PROSPECT: A model of leaf optical properties spectra. *Remote sensing of environment, 34*, 75-91

Jacquemoud, S., Verhoef, W., Baret, F., Bacour, C., Zarco-Tejada, P.J., Asner, G.P., François, C., & Ustin, S.L. (2009). PROSPECT+ SAIL models: A review of use for vegetation characterization. *Remote sensing of environment, 113*, S56-S66

Johnson, D.M. (2014). An assessment of pre-and within-season remotely sensed variables for forecasting corn and soybean yields in the United States. *Remote sensing of environment, 141*, 116-128

Jurdao, S., Yebra, M., Guerschman, J.P., & Chuvieco, E. (2013). Regional estimation of woodland moisture content by inverting radiative transfer models. *Remote sensing of environment, 132*, 59-70

Kerr, Y.H., Waldteufel, P., Wigneron, J.-P., Delwart, S., Cabot, F., Boutin, J., Escorihuela, M.-J., Font, J., Reul, N., & Gruhier, C. (2010). The SMOS mission: New tool for monitoring key elements ofthe global water cycle. *Proceedings of the IEEE, 98*, 666-687

Kirtman, B., Power, S., Adedoyin, A., Boer, G., Bojariu, R., Camilloni, I., Doblas-Reyes, F., Fiore, A., Kimoto, M., & Meehl, G. (2013). Near-term climate change: projections and predictability

Koetz, B., Baret, F., Poilvé, H., & Hill, J. (2005). Use of coupled canopy structure dynamic and radiative transfer models to estimate biophysical canopy characteristics. *Remote sensing of environment, 95*, 115-124

Kogan, F., & Sullivan, J. (1993). Development of global drought-watch system using NOAA/AVHRR data. *Advances in Space Research, 13*, 219-222

Kummerow, C., Barnes, W., Kozu, T., Shiue, J., & Simpson, J. (1998). The tropical rainfall measuring mission (TRMM) sensor package. *Journal of atmospheric and oceanic technology, 15*, 809-817

Lambers, H., Chapin, F.S., & Pons, T.L. (2008). Plant Physiological Ecology. Springer New York

Laurent, V.C., Schaepman, M.E., Verhoef, W., Weyermann, J., & Chávez, R.O. (2014). Bayesian object-based estimation of LAI and chlorophyll from a simulated Sentinel-2 top-of-atmosphere radiance image. *Remote sensing of environment, 140*, 318-329

Lavender, S., & Lavender, A. (2015). *Practical handbook of remote sensing*. CRC Press

Lavergne, T., Kaminski, T., Pinty, B., Taberner, M., Gobron, N., Verstraete, M.M., Vossbeck, M., Widlowski, J.-L., & Giering, R. (2007). Application to MISR land products of an RPV model inversion package using adjoint and Hessian codes. *Remote sensing of environment, 107*, 362-375

Li, P., & Wang, Q. (2011). Retrieval of leaf biochemical parameters using PROSPECT inversion: A new approach for alleviating ill-posed problems. *IEEE Transactions on Geoscience and Remote Sensing, 49*, 2499-2506

Liang, L., Di, L., Zhang, L., Deng, M., Qin, Z., Zhao, S., & Lin, H. (2015). Estimation of crop LAI using hyperspectral vegetation indices and a hybrid inversion method. *Remote sensing of environment, 165*, 123-134

Lloyd-Hughes, B. (2014). The impracticality of a universal drought definition. *Theoretical and Applied Climatology, 117*, 607-611

Martínez-Fernández, J., González-Zamora, A., Sánchez, N., Gumuzzio, A., & Herrero-Jiménez, C. (2016). Satellite soil moisture for agricultural drought monitoring: Assessment of the SMOS derived Soil Water Deficit Index. *Remote sensing of environment*, *177*, 277-286

Masek, J.G., Wulder, M.A., Markham, B., McCorkel, J., Crawford, C.J., Storey, J., & Jenstrom, D.T. (2020). Landsat 9: Empowering open science and applications through continuity. *Remote sensing of environment, 248*, 111968

McKee, T.B., Doesken, N.J., & Kleist, J. (1993). The relationship of drought frequency and duration to time scales. In, *Proceedings of the 8th Conference on Applied Climatology* (pp. 179-183): Boston

Meroni, M., Marinho, E., Sghaier, N., Verstrate, M.M., & Leo, O. (2013). Remote sensing based yield estimation in a stochastic framework—Case study of durum wheat in Tunisia. *Remote Sensing, 5*, 539-557

Miralles, D.G., Holmes, T., De Jeu, R., Gash, J., Meesters, A., & Dolman, A. (2011). Global land-surface evaporation estimated from satellite-based observations. *Hydrology and Earth System Sciences, 15*, 453-469

Mwinuka, P.R., Mbilinyi, B.P., Mbungu, W.B., Mourice, S.K., Mahoo, H., & Schmitter, P. (2021). The feasibility of hand-held thermal and UAV-based multispectral imaging for canopy water status

assessment and yield prediction of irrigated African eggplant (Solanum aethopicum L). *Agricultural water management, 245*, 106584

Njoku, E.G., Jackson, T.J., Lakshmi, V., Chan, T.K., & Nghiem, S.V. (2003). Soil moisture retrieval from AMSR-E. *IEEE Transactions on Geoscience and Remote Sensing, 41*, 215-229

Ollinger, S. (2011). Sources of variability in canopy reflectance and the convergent properties of plants. *New Phytologist, 189*, 375-394

Palmer, W.C. (1965). *Meteorological drought*. US Department of Commerce, Weather Bureau

Pan, Y., Li, L., Zhang, J., Liang, S., Zhu, X., & Sulla-Menashe, D. (2012). Winter wheat area estimation from MODIS-EVI time series data using the Crop Proportion Phenology Index. *Remote sensing of environment, 119*, 232-242

Parry, S., Prudhomme, C., Wilby, R.L., & Wood, P.J. (2016). Drought termination: concept and characterisation. *Progress in Physical Geography, 40*, 743-767

Qu, Y., Wang, J., Wan, H., Li, X., & Zhou, G. (2008). A Bayesian network algorithm for retrieving the characterization of land surface vegetation. *Remote sensing of environment, 112*, 613-622

Rowley, R.J., Price, K.P., & Kastens, J.H. (2007). Remote sensing and the rancher: Linking rancher perception and remote sensing. *Rangeland Ecology & Management, 60*, 359-368

Sah, R., Chakraborty, M., Prasad, K., Pandit, M., Tudu, V., Chakravarty, M., Narayan, S., Rana, M., & Moharana, D. (2020). Impact of water deficit stress in maize: Phenology and yield components. *Scientific reports, 10*, 1-15

Schlerf, M., & Atzberger, C. (2006). Inversion of a forest reflectance model to estimate structural canopy variables from hyperspectral remote sensing data. *Remote sensing of environment, 100*, 281-294

Somerville, C., & Briscoe, J. (2001). Genetic engineering and water. *Science, 292*, 2217-2217

Steduto, P., Hsiao, T.C., Fereres, E., & Raes, D. (2012). *Crop yield response to water*. Food and Agriculture Organization of the United Nations Rome

Toulemont, A., Fernandez, V., Mavrocordatos, C., Mandorlo, G., & Laberinti, P. (2019). Sentinel-2C instrument new features and first instrument performance characterization. In, *Sensors, Systems, and Next-Generation Satellites XXIII* (p. 111510P): International Society for Optics and Photonics

Tucker, C.J. (1979). Red and photographic infrared linear combinations for monitoring vegetation. *Remote sensing of environment, 8*, 127-150

Turvey, C.G., & Mclaurin, M.K. (2012). Applicability of the Normalized Difference Vegetation Index (NDVI) in index-based crop insurance design. *Weather, Climate, and Society, 4*, 271-284

Van Dijk, A.I., Schellekens, J., Yebra, M., Beck, H.E., Renzullo, L.J., Weerts, A., & Donchyts, G. (2018). Global 5 km resolution estimates of secondary evaporation including irrigation through satellite data assimilation. *Hydrology and Earth System Sciences, 22*, 4959-4980

Verhoef, W. (1984). Light scattering by leaf layers with application to canopy reflectance modeling: the SAIL model. *Remote sensing of environment, 16*, 125-141

Vinukollu, R.K., Wood, E.F., Ferguson, C.R., & Fisher, J.B. (2011). Global estimates of evapotranspiration for climate studies using multi-sensor remote sensing data: Evaluation of three process-based approaches. *Remote sensing of environment, 115*, 801-823

Vohland, M., Mader, S., & Dorigo, W. (2010). Applying different inversion techniques to retrieve stand variables of summer barley with PROSPECT+ SAIL. *International Journal of Applied Earth Observation and Geoinformation, 12*, 71-80

Wang, X., Xie, H., Guan, H., & Zhou, X. (2007). Different responses of MODIS-derived NDVI to root-zone soil moisture in semi-arid and humid regions. *Journal of hydrology, 340*, 12-24

Ward, M.N., Holthaus, E., & Siebert, A. (2008). Index insurance for drought in the Millennium Villages Project. In, *American Meteorological Society 20th Conference on Climate Variability and Change, New Orleans, Louisiana*

West, H., Quinn, N., & Horswell, M. (2019). Remote sensing for drought monitoring & impact assessment: Progress, past challenges and future opportunities. *Remote sensing of environment, 232*, 111291

Whitcraft, A.K., Becker-Reshef, I., & Justice, C.O. (2015a). A framework for defining spatially explicit earth observation requirements for a global agricultural monitoring initiative (GEOGLAM). *Remote Sensing, 7*, 1461-1481

Whitcraft, A.K., Becker-Reshef, I., Killough, B.D., & Justice, C.O. (2015b). Meeting earth observation requirements for global agricultural monitoring: An evaluation of the revisit capabilities of current and planned moderate resolution optical earth observing missions. *Remote Sensing, 7*, 1482-1503

Yavuz, D., Seymen, M., Yavuz, N., Çoklar, H., & Ercan, M. (2021). Effects of water stress applied at various phenological stages on yield, quality, and water use efficiency of melon. *Agricultural water management, 246*, 106673

Yebra, M., & Chuvieco, E. (2009). Linking ecological information and radiative transfer models to estimate fuel moisture content in the Mediterranean region of Spain: Solving the ill-posed inverse problem. *Remote sensing of environment, 113*, 2403-2411

Yebra, M., Dennison, P.E., Chuvieco, E., Riaño, D., Zylstra, P., Hunt, E.R., Danson, F.M., Qi, Y., & Jurdao, S. (2013). A global review of remote sensing of live fuel moisture content for fire danger assessment: Moving towards operational products. *Remote sensing of environment, 136*, 455-468

Yi, Q., Wang, F., Bao, A., & Jiapaer, G. (2014). Leaf and canopy water content estimation in cotton using hyperspectral indices and radiative transfer models. *International Journal of Applied Earth Observation and Geoinformation, 33*, 67-75

Zaks, D.P., & Kucharik, C.J. (2011). Data and monitoring needs for a more ecological agriculture. *Environmental Research Letters, 6*, 014017

Zhang, F., & Zhou, G. (2019). Estimation of vegetation water content using hyperspectral vegetation indices: A comparison of crop water indicators in response to water stress treatments for summer maize. *BMC ecology*, *19*, 18

Zhang, L., Zhang, H., Niu, Y., & Han, W. (2019). Mapping maize water stress based on UAV multispectral remote sensing. *Remote Sensing, 11*, 605

Zhang, X., Chen, N., Li, J., Chen, Z., & Niyogi, D. (2017). Multi-sensor integrated framework and index for agricultural drought monitoring. *Remote sensing of environment, 188*, 141-163

Zhou, H., Zhou, G., He, Q., Zhou, L., Ji, Y., & Lv, X. (2021). Capability of leaf water content and its threshold values in reflection of soil–plant water status in maize during prolonged drought. *Ecological Indicators, 124*, 107395

Chapter 1: Characterizing the variability of the structure parameter in the PROSPECT leaf optical properties model

Published in *Remote Sensing* as:

Boren, E.J., Boschetti, L. and Johnson, D.M., 2019. Characterizing the variability of the structure parameter in the PROSPECT leaf optical properties model. Remote Sensing, 11(10), p.1236.

Abstract

Radiative transfer model (RTM) inversion allows for the quantitative estimation of vegetation biochemical composition from satellite sensor data, but large uncertainties associated with inversion make accurate estimation difficult. The leaf structure parameter (N_s) is one of the largest sources of uncertainty in inversion of the widely used leaf-level PROSPECT model, since it is the only parameter that cannot be directly measured. In this study, we characterize N_s as a function of phenology by collecting an extensive dataset of leaf measurements from samples of three monocotyledon species (hard red wheat, soft white wheat, and upland rice) and one dicotyledon (soy), grown under controlled conditions over two full growth seasons. A total of 230 samples were collected: Measured leaf reflectance and transmittance were used to estimate N_s from each sample. These experimental data were used to investigate whether N_s depends on phenological stages (early / mid / late), and/or irrigation regime (irrigation at 85%, 75%, 60% of the initial saturated tray weight, and pre-/post-irrigation). The results, supported by the extensive experimental data set, indicate a significant difference between N_s estimated on monocotyledon and dicotyledon plants, and a significant difference between N_s estimated at different phenological stages. Different irrigation regimes did not result in significant N_s differences for either monocotyledon or dicotyledon plant types. To our knowledge, this study provides the first systematic record of N_s as a function of phenology for common crop species.

Introduction

Terrestrial biogeochemical cycles are primarily driven by plant physiological and ecological processes involving the exchange of matter and energy, such as photosynthesis and evapotranspiration (Bonan 2008; Reichstein et al. 2014; Running and Coughlan 1988). Knowledge of plant canopy biochemical composition provides critical information towards understanding and predicting the flow of energy and matter within terrestrial biogeochemical cycles (Schimel et al. 1991; Trumbore 2006). However, generalizing field measured plant or canopy biochemical processes, albeit locally accurate, is not a feasible method for inferring larger landscape ecosystem processes.

Spaceborne radiometric remote sensing measurements of solar electromagnetic radiation, reflected by the Earth's surface, can be used to monitor physical interactions between leaf properties

and canopy structure, thereby delivering valuable information relevant to terrestrial biogeochemical cycles (Justice et al. 1998; Running et al. 2004; Ustin et al. 2004). Empirical methods, which rely on statistical relationships of observed phenomena with remote sensing measurements, are widely applied as being simple and computationally efficient. Typically, with this approach, multispectral reflectances are combined into vegetation indices, designed to maximize the sensitivity to parameters of interest while minimizing the influence of unrelated factors, including soil or atmospheric effects (Baret and Guyot 1991; Pinty and Verstraete 1991). The vegetation indices are subsequently correlated to biochemical variables such as photosynthetically active pigments, water, and biomass.

The systematic application of vegetation indices for quantitative biochemical component estimation, however, is hampered by large uncertainties. Spectral indices are inevitably sensitive to multiple biochemical and structural characteristics of vegetative canopy systems, and are constrained by the representativeness of the training data needed by this approach (Baret and Buis 2008; Jacquemoud et al. 2000; Zhang et al. 2017). Alternatively, physical-based approaches may be applied to overcome transferability problems that arise during systemic application (Darvishzadeh et al. 2011).

Physical-based approaches are used to estimate canopy biochemical and structural characteristics through radiative transfer modeling by simulating the interactions of electromagnetic energy with leaf and canopy surfaces based on the laws of physics (Goel 1988; Jacquemoud and Baret 1993). Among these, leaf optical spectral properties are critical indicators of plant physiology (Carter and Knapp 2001; Serbin et al. 2011; Ustin et al. 2009), which affect other functional processes up to ecosystem levels (Reichstein et al. 2014). Leaves also act as the primary scattering and absorbing elements of plant canopy systems (Baret et al. 1994; Govaerts and Verstraete 1995).

The leaf Propriétés Spectrales radiative transfer model (PROSPECT), which simulates hemispherical reflectance and transmittance of a leaf in reflective wavelengths in the 400–2500 nm spectral region (Jacquemoud and Baret 1990), is one of the most widely applied physical-based models for leaf trait estimation (Jacquemoud et al. 2009; Sun et al. 2018). The model has been successfully used to estimate leaf biochemical components by inverting leaf reflectance measurements (Sun et al. 2018; Zhang et al. 2017; Zhao et al. 2014).

PROSPECT is based on the plate theory model (Allen et al. 1969), where a leaf is conceptualized as one or multiple compact absorbing plates with rough surfaces. The model calculates the radiative transfer of energy at the surface and inside the leaf as a function of: (1) the angle of incidence of incoming radiation α, (2) the refractive index $n(\lambda)$, (3) a dimensionless leaf structural parameter that represents the number of homogenous layers (or plates) N_s, and airspaces $N_s - 1$,

specifying the number of cell wall/air space interfaces within the plant leaf mesophyll, and (4) the contents of biochemical components per leaf area *Cspe*, multiplied by the corresponding absorption coefficients $k_{spe}(\lambda)$.

Several versions of the model have been published since first introduced in 1990 (Jacquemoud et al. 2000; Jacquemoud and Baret 1990; Jacquemoud et al. 1996; Le Maire et al. 2004): the most recent version being PROSPECT-5 (Féret et al. 2008) and PROSPECT-D (Féret et al. 2017). The biochemical components used in PROSPECT-5 are presented in Table 1.

In the PROSPECT-5 version of the model, the incidence of incoming radiation α, refractive index $n(\lambda)$, and specific absorption coefficients $k_{spe}(\lambda)$ have been estimated and fixed in the model (Féret et al. 2008). Therefore, the estimation of a single leaf's reflectance and transmittance in PROSPECT-5 is driven by user inputs: The N_s parameter and contents of the biochemical components per leaf area C_{spe}. The spectral absorption coefficient $k(\lambda)$ is estimated as:

$$k(\lambda) = \frac{(C_{cab} * k_{cab}(\lambda)) + (C_{car} * k_{car}(\lambda)) + (C_m * k_m(\lambda)) + (C_w * k_w(\lambda))}{N_s}, \quad (1)$$

Leaf transmittance $\tau(\lambda)$ and reflectance $\rho(\lambda)$ are subsequently derived from the spectral absorption coefficient $k(\lambda)$, angle of incidence of incoming radiation α, refractive index $n(\lambda)$, and number of airspaces $N_s - 1$ following the methods introduced by Jacquemoud and Baret (Jacquemoud and Baret 1990).

The inversion of a model for the retrieval of biophysical variables is inherently an "ill-posed" problem (Combal et al. 2003): In many cases, it is likely that more than one set of values of the variables would satisfy the inversion. Combal et al. (2003) recommended the use of *a priori* information to address the "ill-posed" nature of the problem by constraining the range of biophysical values resulting from the inversion, thereby eliminating unrealistic solutions. Several studies have reported significant improvements to biophysical parameter retrieval by using *a priori* information to constrain the inversion (Danson and Bowyer 2004; Koetz et al. 2005; Lavergne et al. 2007). There is still a need, however, to advance our knowledge of the range of key biophysical variables and of associated uncertainties (Combal et al. 2003; Laurent et al. 2014; Qu et al. 2008).

The N_s parameter is a major source of uncertainty in the inversion of the PROSPECT model as it is the only parameter that is based on a conceptual quantity (i.e., number of plates) rather than a measurable physiological trait. Theoretically, N_s is connected to leaf characteristics such as thickness and intercellular properties, including fraction of airspace and mesophyll cell structural dimensions (Govaerts et al. 1996; Jacquemoud and Baret 1990). The internal structural properties and cell types

(i.e., epidermis, palisade, and spongy mesophyll) of leaves play a key role in regulating internal light for maximizing photosynthetic activity, especially with regard to energy not easily absorbed at the leaf surface (Oguchi et al. 2018; Smith et al. 1997). For example, upper epidermis cell shape (spherical vs elliptical) dictates the distribution of intercepted energy within the leaf while palisade mesophyll cells act as a conduit for photons to enter the spongy mesophyll. Spongy mesophyll cells and interior air spaces (many air–water interfaces) induce a scattering effect to maximize absorption by chloroplasts. Since the visible (400–750 nm) and mid-infrared (> 1400 nm) regions are governed by the two primary absorbers in leaf tissue (pigments and water, respectively), the NIR wavelengths (750–1400 nm) represents the region in which leaves are most optically transparent and is primarily influenced by leaf structural properties (Ollinger 2011). In PROSPECT, these intercellular characteristics are lumped into the N_s parameter. Previous approaches to link N_s with physical traits, like specific leaf area (SLA), are based on empirical relationships that are difficult to transfer (Ceccato et al. 2001). As a result of the simplification of leaf structural properties, N_s cannot be easily connected to any corresponding physical traits (Ollinger 2011).

The sensitivity analysis conducted by Ceccato et al. (2001) demonstrated that N_s is a key parameter within PROSPECT. When applying the model in direct mode to estimate leaf reflectance at 1600 nm, N_s has the greatest influence on the uncertainty of the model output (41.1%), as compared to leaf water content (36.4%) and dry matter content (22.5%). Consequently, when applying the model in inverse mode, constraining the range of possible N_s values would greatly reduce the uncertainty in estimating other biophysical variables of interest.

Jacquemoud and Baret (1990) indicated that the different structural properties of monocotyledon and dicotyledon species cause differences in estimated N_s values, with monocotyledon leaves ranging between 1 and 1.5 and the thicker and structurally more complex leaves of dicotyledon leaves resulting in N_s values between 1.5 and 2.5. Processes driven by leaf growth are also important when considering the scattering of energy. Demarez (1999) observed seasonal variation of N_s in select temperate deciduous forest species and linked the change of N_s throughout time to the development of the leaves. In that study, N_s increased gradually during leaf tissue development in the initial growth stages, plateaued during most of the summer months, then rapidly increased during senescence. The rapid increase of N_s at the end of the study period was linked with an amplified scattering effect caused from degradation of leaf structural features resulting from the reduction of leaf water content. This link was made because, as leaves approach fully turgid or wilted states, leaf cell size, shape, and distribution are altered resulting in changes in scattering properties (Gausman et al. 1969). Despite this, we are not aware of any studies that examine the effect of water stress on N_s, regardless of the fact that several

studies used PROSPECT inversion to estimate vegetation water content (Baret and Fourty 1997; Ceccato et al. 2001; Gerber et al. 2011; Jurdao et al. 2013; Zarco-Tejada et al. 2003).

A few studies exist that examine the variation of N_s as a function of vegetation physiological status (i.e., water stress) and phenology (Demarez 1999; Jacquemoud and Baret 1990; Jacquemoud et al. 1996; Zhang et al. 2017), but no prior study presents a comprehensive analysis of this relationship. Zhang et al. (2017) established an indirect relationship between leaf reflectance and copper stress through the N_s parameter in two crop species at two vegetative growth stages. Jacquemoud and Baret (1990) used a limited set of greenhouse measurements to state that a difference exists between estimated N_s in monocotyledon and dicotyledon leaves; Jacquemoud et al. (1996) found that this difference might not be observed on leaves grown outdoors, but neither study took phenology into consideration. Finally, Demarez (1999) reported estimated N_s from leaves at various stages throughout leaf development, but this study was limited to temperate tree species grown in a deciduous forest under the same environmental conditions. Furthermore, to the best of our knowledge, no published dataset reports reference N_s values of common monocotyledon and dicotyledon crop species throughout the growing season.

The present study is designed to assess whether there is a statistically significant variation in N_s as a function of phenology and irrigation, and to provide reference values of N_s to be used as *a priori* information for the inversion of PROSPECT in future research.

The present study involved three main components: (1) a large data collection experiment was performed over two growing seasons to collect a comprehensive dataset of leaf optical spectral measurements for use in N_s estimation; (2) PROSPECT-5 was inverted to estimate N_s using the leaf optical spectral dataset; (3) the distribution of estimated N_s values was analyzed statistically as a function of phenological class and irrigation regime.

Methods and Materials

Data collection

An extensive experiment was conducted in which plants (monocotyledon and dicotyledon) were grown under controlled conditions to collect a representative dataset of leaf optical spectral measurements over a period of 90 days, to cover the full phenological cycle of the plants. Additionally, the plants were subjected to different irrigation regimes to create controlled water stress conditions. Measurements were performed throughout the entire growing season. The phenological stages of the plants grown were aggregated into three main phenological classes, defined to delimit periods in which plants are most temperature and water sensitive.

Experimental design

Pitkin's forest research nursery during the summers of 2015 and 2016 contained three monocotyledons (hard red wheat—*Triticum durum* Desf., soft white wheat—*Triticum aestivum* L., and upland rice—*Oryza sativa* L.) and one dicotyledon (soy—*Glycine max* L.). All four were grown in 2015, and two were also grown in 2016 (hard red wheat and soy). The plants were grown outdoors in 45-well foam trays. Watering was controlled, following the procedures detailed below. Other environmental variables, such as temperature, sunlight, and exposure to wind were not controlled.

Each tray contained 45 plants of the same species (one plant for each well); 2–3 seeds per well were initially planted. After plant emergence, if more than one seed had germinated in the same well, the additional plants were removed to ensure one seedling per well. Plants were watered through sub-irrigation methods, allowing for direct control over the amount of water administered while limiting tissue disease. The water for sub-irrigation contained a mixture of starter fertilizer to obtain a nitrogen content of 50 ppm. To water a tray, an 18-gallon bin was filled with approximately 3 gallons of the nitrogen starter mixture. The tray was placed in the bin to allow the starter mixture to soak the tray up from the bottom. The tray would remain in the starter mixture for 30 minutes before being removed. To determine whether sub-irrigation was necessary, each tray was weighed every day. The tray was irrigated only if on that day its weight had dropped below a given percentage of the initial tray saturation weight.

Plant extraction for performing the measurements began approximately 27 days after planting to allow the plants to establish. For the plants grown in 2015, plant extraction and leaf optical measurements occurred regularly once a week and three plants were removed from each tray during the extraction. In 2016, plant extraction and measurements were dependent on watering frequency. Two plants were extracted and sampled immediately before watering occurred and again 24 hours after watering occurred.

The life cycle stages of the plants were aggregated into three main phenological classes (early, mid, late), reported in Figure 1.1. These three phenological classes were defined based on the sensitivity to drought (water deficit) and temperature of each growth stage for each crop. The 'early' class was defined to include the vegetative periods, where extreme temperatures and water deficit have consequences that slow or stop development and reduce yield in later life cycle stages (Doorenbos and Kassam 1979). The 'mid' and 'late' classes encompass the flowering and yield formation phases of the crop's life cycle, respectively. In terms of successful yield, these periods are the most sensitive to water and temperature extremes (Doorenbos and Kassam 1979). The crops used in this study are less

susceptible to drought or extreme temperatures when full maturity is achieved. Therefore, life cycle stages after the 'late' phenological class were not considered, and plants were no longer sampled.

Since the plants were grown outdoors, the samples were subjected to the same temperature and sunlight conditions. The upland rice plants did not grow past the flowering growth stages as the local outdoor conditions slowed development in the early and mid-phenological classes. As the experiment ended after 90 days, before the upland rice plants reached the ripening growth phase, the upland rice samples were aggregated into two phenological classes only (early and mid).

In 2015, plants were separated into three separate irrigation regimes resulting in three groups of four trays (four species)—for a total of 12 trays. The trays were weighed daily at approximately the same time of day to determine if watering should occur. Irrigation occurred when the tray reached 85%, 75%, and 60% of the initial saturated weight measured at the beginning of the growing season for regimes 1, 2, and 3, respectively.

In 2016, all plants were watered following the same regime, hence only one tray per species was grown. As in the 2015 experiment, the trays were weighed daily at approximately the same time of day to determine if irrigation would occur. Irrigation occurred when the tray reached 60% of the initial saturated weight measured at the beginning of the growing season.

Measurement protocol

Extraction occurred by cutting the plant at the base, just above the soil line, and immediately placing it in a plastic bag to minimize water loss. Bags were put in a cooler until processing in the lab approximately an hour after extraction. Leaf sample water loss was assumed to be minimal during transportation to the lab for measurements. Extraction and leaf measurements occurred at approximately the same time each day.

Leaf bidirectional reflectance factor ($\rho_{BRF\,\lambda}$) [dimensionless] and transflectance [dimensionless] were measured with a PSR-3500 field spectroradiometer (Spectral Evolution, Inc). The instrument collects measurements on a full spectral range of wavelengths, from 350 nm to 2500 nm, with a spectral resolution of 3 nm at 700 nm, 8 nm at 1500 nm, and 6 nm at 2100 nm. All data were interpolated to 1 nm sampling interval before further processing, resulting in 2151 bands. The field spectroradiometer was equipped with a pistol-grip contact probe with leaf clip, using a 5-watt tungsten halogen source at 12-degree incidence zenith to the target for spectral measurements. The leaf clip attachment for the contact probe includes a two-sided reversible plate that holds the leaf sample during measurement and excludes ambient direct and scattered light from the sensor. One side of the plate is

a near 100% reflective Lambertian Spectralon panel (Labsphere Inc., North Sutton, NH) and the opposite side is a black surface with near 0% reflectance. Radiance measurements were calibrated using the Spectralon panel before scanning each leaf. The instrument was set to acquire and average 10 spectra per scan to reduce noise and was considered the optimal compromise between time required for spectra collection and noise reduction. Measurements were performed on five points of the leaf and subsequently averaged. The black plate was used to measure $\rho_{BRF\,\lambda}$ as it ensures that only electromagnetic radiation directly reflected by the leaf is measured by the sensor, as any radiation transmitted through the leaf is absorbed by the plate. The white plate was used as the background to measure leaf transflectance, defined as the sum of leaf reflectance and double transmittance: The spectroradiometer acquires the energy directly reflected by the leaf, plus the energy that is transmitted through the leaf, reflected by the Spectralon panel, and transmitted through the leaf a second time (Lam and Rotman 2010). While leaves from all plants sampled after the 27-day establishment period were measured with the leaf clip, only leaves that fully covered the leaf clip field of view area were considered in the present study.

Spectral data processing

A function based on the Kubelka-Munk theory of light scattering and absorption was applied to measured leaf transflectance to estimate leaf transmittance (τ_λ) [dimensionless]:

$$\tau_\lambda = \sqrt{(\rho_{TF\lambda} - \rho_{BRF\lambda})(\frac{1}{\rho_{w\lambda}} - \rho_{BRF\lambda})}, \quad (2)$$

where τ_λ is the estimated transmittance, $\rho_{TF\lambda}$ is the measured transflectance of the leaf using the white plate background, $\rho_{BRF\lambda}$ is the measured reflectance of the leaf using the black plate background, and $\rho_{w\lambda}$ is the measured reflectance of the white plate. Transmittance estimated from Equation 2 has been used in PROSPECT inversion problems with success in previous research (Arellano et al. 2017) and is used in the estimation of N_s for this study due to the unavailability of an integrating sphere for collecting the spectral measurements

Since the PROSPECT models were originally calibrated on directional hemispherical reflectance spectra ($\rho_{DHRF\,\lambda}$) measured with an integrating sphere (Féret et al. 2008; Jacquemoud and Baret 1990), inverting the PROSPECT-5 model using leaf clip $\rho_{BRF\,\lambda}$ measurements would not be appropriate (Jay et al. 2016).

Both $\rho_{BRF\,\lambda}$ and $\rho_{DHRF\,\lambda}$ result from the combination of a leaf surface reflectance component, which accounts for the electromagnetic radiation that does not penetrate the leaf and is directly

reflected, and a diffuse reflectance component, which is the result of intercellular physical and biochemical constituents (Bousquet et al. 2005). By separating surface reflectance from the diffuse reflectance, it is possible to correct, prior to the radiative transfer model (RTM) inversion, $\rho_{BRF\,\lambda}$ measured with a leaf clip (Li et al. 2018). Bousquet et al. (2005) and Jay et al. (2016) summarized and demonstrated the principles, which connect integrating sphere measured $\rho_{DHRF\,\lambda}$ and leaf clip measured $\rho_{BRF\,\lambda}$, assuming a small incidence zenith, resulting in the characterization of the surface component, which can be used to account for the differences in physical properties between $\rho_{DHRF\,\lambda}$ and $\rho_{BRF\,\lambda}$:

$$\rho_{BRF\lambda} - \rho_{BRFsur\lambda} = \rho_{DHRF\lambda} - \rho_{DHRFsur\lambda}, \quad (3)$$

At a wavelength of 445 nm, where strong absorption of leaf pigments occurs, it is possible to assume only direct reflectance to occur at the leaf surface (Sims and Gamon 2002), thus estimating a simple function, known as PROREF (Li et al. 2018), is used to correct the $\rho_{BRF\,\lambda}$ measurement of each leaf sample:

$$\rho'_{meas\lambda} = \rho_{BRF\lambda} - (\rho_{BRF445} - \rho_{mod445}), \quad (4)$$

where $\rho'_{meas\lambda}$ is the adjusted spectral reflectance, and ρ_{BRF445}, and ρ_{mod445} are the measured and modeled leaf reflectance at 445 nm. ρ_{mod445} was generated and Equation 4 was computed with each iteration of the N_s inversion step described in Section 2.2, with constant values set for Cc_{ab} and Cc_{ar} at 47.28 µg $cm^{-2}$and 10.31 µg cm^{-2}, respectively, and the N_s value from the iteration. The solution to Equation 5 was computed with each iteration of N_s inversion until minimization was reached. The method for minimization is described in more detail in the data analysis section.

The pigment parameter values were determined by taking the average of Cc_{ab} and Cc_{ar} from all of the leaves in the LOPEX leaf dataset (Hosgood et al. 1995). Using only pigment values from soybean and rice leaf, LOPEX samples did not significantly change $\rho_{mod\,445}$ (less than a tenth of a percent). Similarly, the difference in $\rho_{mod\,445}$ generated with N_s = 1 and N_s = 3 was less than a half percent. An example of the PROREF function being applied in the NIR region of measured mature soy leaf spectra is presented in Figure 1.2.

Data analysis

The PROSPECT-5 model was inverted to estimate N_s for each leaf sample, using the three-wavelength inversion method proposed by Féret et al. (2008). The method uses reflectance and transmittances measured at three wavelengths in the NIR plateau, where the leaf spectral response is more sensitive to the N_s parameter, rather than to the concentration of the biochemical components. The

three wavelengths are identified based on the measured reflectance and transmittance of each leaf sample in the 800–1300 nm range, as:

- λ_1: Wavelength of minimum absorbance (i.e., the maximum of the sum of measured transmittance and reflectance).
- λ_2: Wavelength of maximum measured reflectance.
- λ_3: Wavelength of maximum measured transmittance.

The approximate location of these three wavelengths are illustrated in Figure 1.3 on the same example spectra as Figure 1.2.

The inversion is performed by minimizing a merit function, defined as:

$$J\left(N_s, k_i(\lambda_i)\right) = \sum_{i=1}^{3}(\rho_{mes}(\lambda_i) - \rho_{mod}(N_s, k(\lambda_i)))^2 + (\tau_{mes}(\lambda_i) - \tau_{mod}(N_s, k(\lambda_i)))^2, \quad (5)$$

where $\lambda_i = (\lambda_1, \lambda_2, \lambda_3)$ are the three wavelengths defined above, $\rho_{mes}(\lambda_i)$ and $\tau_{mes}(\lambda_i)$ are the measured reflectance and transmittance, $\rho_{mod}(\lambda_i)$ and $\tau_{mod}(\lambda_i)$ are the reflectance and transmittance simulated by applying the model in forward mode, and $k(\lambda_i)$ is the absorption coefficient of an elementary layer N_s at the three wavelengths. The function J was minimized using the Nelder-Mead downhill simplex method (Nelder and Mead 1965), setting an arbitrary starting value for the numerator of Equation 1 and N_s, and iteratively searching in the parameter space for the solution resulting in the minimum difference between modeled and measured leaf spectra.

The population of N_s resulting from inversion of the measurements of each leaf sample was analyzed through an ANOVA test to determine whether the range of variation of N_s can be explained by considering plant type (monocotyledon vs. dicotyledon), phenological class (early / mid / late), and irrigation regime (irrigation at 85%, 75%, and 60% of the initial saturated weight, and pre-/post-irrigation). The statistical analysis was conducted as follows:

1. The population of estimated N_s values was stratified into sub-populations according to the criteria defined in Section 2.1.
2. A Welch's two-sample t-test was performed to determine if the estimated means of monocotyledon and dicotyledon N_s differed significantly from one another.
3. A Welch's two-sample t-test was run to determine whether there was a significant difference between the estimated means of pre- and post-irrigation N_s for each plant type.

4. Welch's one-way ANOVA tests were run to test whether the variation of N_s in each plant type can be explained by phenological class (early / mid / late) and irrigation regime (irrigation at 85%, 75%, and 60% of the initial saturated weight)

If the ANOVA test was significant at $P \leq 0.05$, then Welch's two-sample t-tests were carried out to compare the means of classes within the sub-population of the plant type. For example, if phenological class returned a significant result as an explanatory variable for N_s in the sampled monocotyledon leaves, then the means of 'early', 'mid', and 'late' monocotyledon N_s would be compared.

Results

In total, 230 independent estimates of N_s were retrieved from the spectral measurements: 158 from the 2015 experiment and 72 from the 2016 experiment. The timeseries of estimated N_s from the 2015 and 2016 nursery experiments are presented in Figure 1.4 and 1.5, respectively. A summary of the estimated N_s, stratified by plant type and phenological class, is presented in Table 1.2.

The summary in Table 1.2 illustrates monocotyledon N_s values primarily fit within the range 1.3–1.7 ($\mu = 1.46$, $\sigma = 0.29$) and dicotyledon N_s values exhibited a distribution primarily between 1.9 and 2.2 ($\mu = 2.07$, $\sigma = 0.27$). Overall, a pattern of N_s increasing with days after seeding was observed with the sampled monocotyledon plants, with lower values in the 'early' stage ($\mu = 1.35$, $\sigma = 0.28$) and higher values in the 'mid' and 'late' stages: ($\mu = 1.50$, $\sigma = 0.23$) and ($\mu = 1.66$, $\sigma = 0.25$), respectively. Soy began with higher estimated values of N_s ($\mu = 2.17$, $\sigma = 0.19$), lower 'mid' stage ($\mu = 1.96$, $\sigma = 0.25$), and finally increased during the 'late' stage ($\mu = 2.14$, $\sigma = 0.29$). The progression of distributions for each plant type over time is illustrated in the box plots of Figure 1.6, again illustrating the high-low-high pattern for dicotyledon soy and increase over time for the monocotyledon plants. The results from statistical analyses described in the data analysis section are presented in Table 1.3.

The Welch's two-sample t-test run for the whole dataset ('all') comparing N_s means by plant type shows a significant difference ($P < 0.001$) between the means of monocotyledon and dicotyledon. It was also determined that phenological classes influence the variation of estimated N_s within each plant type, with $F(2,115) = 13.40$, $P < 0.001$ for monocotyledon phenological classes and $F(2,109) = 7.10$, $P = 0.001$ for dicotyledon phenological classes. Finally, no significant differences were observed between the irrigation regime N_s means for either 2015 or 2016.

Since it was determined that phenological classes were a significant source of variance in estimated N_s, Welch's two-sample t-tests were run to intercompare the phenological classes sub-population means of N_s (early / mid / late) within each plant type. The results from those analyses are

presented in Table 4. Significant differences between sub-population means of N_s in every consecutive phenological class were observed.

Discussion

Our analysis relied on an extensive experimental dataset, collected over two growing seasons with a rigorous data collection protocol. The distribution of estimated N_s was consistent with expected values for monocotyledon and dicotyledon plant types: monocotyledon N_s primarily ranged between values of 1.0–1.5, and dicotyledon N_s primarily ranged between values of 1.5 and 2.5 (Jacquemoud et al. 1996). The statistical analysis performed on the population of estimated N_s indicated that there was a significant difference between plant types, and that there was a significant difference by broad phenological class. There was instead no significant difference between N_s estimated from plants subject to different irrigation regimes.

The results align with previous literature reporting that structural changes, driven by growth and maturation, influence N_s (Demarez 1999; Jacquemoud et al. 2009). In particular, we observed a pronounced increase of N_s over time in monocotyledon leaves and a less pronounced dicotyledon seasonality, with higher N_s in the early and late phases, than in the mid growing phase. While the monocotyledon seasonality is in line with previous results derived from measurements on broadleaved plants (Demarez 1999), to the best of our knowledge, the reduced sensitivity of N_s to phenology in certain dicotyledon leaves has not been reported in the available literature. Higher mean N_s in the 'early' phenological stages of the dicotyledon plants may be attributed to a change of leaf properties as the leaves begin to mature, i.e., leaf thickness decreasing or the wider spatial distribution of trichomes per unit leaf area as the leaves mature, which affect the transmission of NIR energy. A more detailed investigation of N_s as a function of phenology in dicotyledon species, which will examine a wider variety of species, will be conducted in the future. For monocotyledon N_s, while samples were rejected if the leaf material did not cover the full leaf clip field of view, the strong variation in data points derived from measurements performed less than 60 days after seeding may be attributed to errors with the leaves sampled during the early tillering stages, when in some cases the leaves were still too small for a reliable spectral measurement.

The irrigation regime did not explain the variation estimated N_s. The presence of water either has a direct influence on the spectral signal of leaves, through the rotation-vibration features of water in the mid-infrared region, or an indirect influence, through the structural and physiological biochemical responses of leaves to hydration or dehydration. The result that irrigation regime did not influence the estimation of N_s is consistent with the fact that the estimation of N_s is independent of both direct (i.e., mid-infrared absorption characteristics of water) and most indirect (i.e., changing pigment

content) water content influences. Leaf wilting does influence the estimation of N_s, but only when water loss has developed sufficiently enough to result in severe leaf dehydration, causing a significant response in the NIR spectral region (Suplick-Ploense et al. 2011). Although the irrigation regime did not have a significant influence over the variance of the N_s parameter in our study, water still has the potential to affect the structural components of leaves and should be considered on an individual species and ecosystem basis along with other environmental factors, such as toxicity, nutrient availability, and disease. Future studies, which examine the influence of wilting or fully turgid cellular properties on the estimation of N_s in more extreme cases, will need to account for irrigation regimes on an individual species basis. Notwithstanding these limitations, the finding that the irrigation regimes used in the current study do not significantly influence N_s has particular relevance as it implies that *a priori* N_s values, tabulated solely as a function of plant type and phenology (i.e., Table 2), can be used to constrain the inversion of PROSPECT. A common use of PROSPECT is the estimation of canopy water content, and in such case the leaf water content is evidently unavailable to inform the *a priori* selection of N_s.

A few caveats should be considered if using *a priori* N_s values, estimated in this study through leaf-level inversions, for canopy level studies. First, the heterogeneity of the canopy should be considered, as different plant types and different phenological stages might be present. Second, N_s may vary within a single species depending on other factors besides phenology, such as environmental conditions (Zhang et al. 2017) and illumination (sun vs shade) (Demarez 1999). Future research will be focused on coupled radiative transfer model inversion for estimating canopy traits in an agricultural setting where species, environmental conditions, illumination, and phenology are relatively uniform, and on the evaluation of the reduction of canopy water content uncertainty that can be attained by constraining the range of variation of N_s.

Conclusion

This paper presents the results of an extensive experiment aimed at the assessment of the PROSPECT radiative transfer model leaf parameter (N_s) as a function of phenological class, and whether water content would indirectly influence the estimation of the N_s parameter. While several datasets of leaf spectral and biophysical properties are available (Féret et al. 2008; Gitelson and Merzlyak 1994; Hosgood et al. 1995; Richardson et al. 2002), our results, obtained over the full extent of the growing season and accounting for a range of irrigation regimes, provide the first detailed phenology dependent record of N_s values for two common crop species. The results indicate a significant difference between N_s estimated on the considered monocotyledon and dicotyledon plants, and new findings of a significant difference between N_s estimated at different phenological stages. The results also indicate other new findings, namely that irrigation regimes did not result in significant N_s

differences for either monocotyledon or dicotyledon plant types. Since only four plant species (three monocotyledons and one dicotyledon) were considered in this study, further research will be needed to assess whether these results can be generalized to different species. A second priority for future research will be on the quantitative assessment of the reduction of uncertainty in estimating plant biophysical variables when applying *a priori* N_s values in PROSPECT inversions and whether constraining the range of variation of N_s can reduce the uncertainty of retrieving certain canopy variables in coupled radiative transfer model inversion.

Acknowledgements

This project was supported by the NASA Idaho Space Grant Consortium Fellowship and by the College of Natural Resources of the University of Idaho Doctoral Finishing Fellowship. We would like to acknowledge the staff support and equipment use of the University of Idaho Pitkin's Nursery.

References

Allen, W.A., Gausman, H.W., Richardson, A.J., & Thomas, J.R. (1969). Interaction of isotropic light with a compact plant leaf. *JOSA, 59*, 1376-1379

Arellano, P., Tansey, K., Balzter, H., & Boyd, D.S. (2017). Field spectroscopy and radiative transfer modelling to assess impacts of petroleum pollution on biophysical and biochemical parameters of the Amazon rainforest. *Environmental earth sciences, 76*, 217

Arraudeau, M., & Vergara, B.S. (1988). *A farmer's primer on growing upland rice*. Int. Rice Res. Inst.

Baret, F., & Buis, S. (2008). Estimating canopy characteristics from remote sensing observations. Review of methods and associated problems. *Advances in land remote sensing: System, modeling, inversion and application*, 173-201

Baret, F., & Fourty, T. (1997). Estimation of leaf water content and specific leaf weight from reflectance and transmittance measurements. *Agronomie, 17*, 455-464

Baret, F., & Guyot, G. (1991). Potentials and limits of vegetation indices for LAI and APAR assessment. *Remote sensing of environment, 35*, 161-173

Baret, F., Vanderbilt, V.C., Steven, M.D., & Jacquemoud, S. (1994). Use of spectral analogy to evaluate canopy reflectance sensitivity to leaf optical properties. *Remote sensing of environment, 48*, 253-260

Bonan, G.B. (2008). Forests and climate change: forcings, feedbacks, and the climate benefits of forests. *Science*, *320*, 1444-1449

Bousquet, L., Lachérade, S., Jacquemoud, S., & Moya, I. (2005). Leaf BRDF measurements and model for specular and diffuse components differentiation. *Remote sensing of environment, 98*, 201-211

Carter, G.A., & Knapp, A.K. (2001). Leaf optical properties in higher plants: linking spectral characteristics to stress and chlorophyll concentration. *American Journal of Botany, 88*, 677-684

Ceccato, P., Flasse, S., Tarantola, S., Jacquemoud, S., & Grégoire, J.-M. (2001). Detecting vegetation leaf water content using reflectance in the optical domain. *Remote sensing of environment, 77*, 22-33

Combal, B., Baret, F., Weiss, M., Trubuil, A., Mace, D., Pragnere, A., Myneni, R., Knyazikhin, Y., & Wang, L. (2003). Retrieval of canopy biophysical variables from bidirectional reflectance: Using prior information to solve the ill-posed inverse problem. *Remote sensing of environment, 84*, 1-15

Danson, F., & Bowyer, P. (2004). Estimating live fuel moisture content from remotely sensed reflectance. *Remote sensing of environment, 92*, 309-321

Darvishzadeh, R., Atzberger, C., Skidmore, A., & Schlerf, M. (2011). Mapping grassland leaf area index with airborne hyperspectral imagery: A comparison study of statistical approaches and inversion of radiative transfer models. *ISPRS Journal of Photogrammetry and Remote Sensing, 66*, 894-906

Demarez, V. (1999). Seasonal variation of leaf chlorophyll content of a temperate forest. Inversion of the PROSPECT model. *International Journal of Remote Sensing, 20*, 879-894

Doorenbos, J., & Kassam, A. (1979). Yield response to water. *Irrigation and drainage paper, 33*, 257

Féret, J.-B., François, C., Asner, G.P., Gitelson, A.A., Martin, R.E., Bidel, L.P., Ustin, S.L., Le Maire, G., & Jacquemoud, S. (2008). PROSPECT-4 and 5: Advances in the leaf optical properties model separating photosynthetic pigments. *Remote sensing of environment, 112*, 3030-3043

Féret, J.-B., Gitelson, A., Noble, S., & Jacquemoud, S. (2017). PROSPECT-D: Towards modeling leaf optical properties through a complete lifecycle. *Remote sensing of environment, 193*, 204-215

Gausman, H., Allen, W., Myers, V., & Cardenas, R. (1969). Reflectance and Internal Structure of Cotton Leaves, Gossypium hirsutum L. 1. *Agronomy journal, 61*, 374-376

Gerber, F., Marion, R., Olioso, A., Jacquemoud, S., Da Luz, B.R., & Fabre, S. (2011). Modeling directional–hemispherical reflectance and transmittance of fresh and dry leaves from 0.4 μm to 5.7 μm with the PROSPECT-VISIR model. *Remote sensing of environment, 115*, 404-414

Gitelson, A., & Merzlyak, M.N. (1994). Spectral reflectance changes associated with autumn senescence of Aesculus hippocastanum L. and Acer platanoides L. leaves. Spectral features and relation to chlorophyll estimation. *Journal of plant physiology, 143*, 286-292

Goel, N.S. (1988). Models of vegetation canopy reflectance and their use in estimation of biophysical parameters from reflectance data. *Remote Sensing Reviews, 4*, 1-212

Govaerts, Y., & Verstraete, M.M. (1995). Evaluation of the capability of BRDF models to retrieve structural information on the observed target as described by a three-dimensional ray tracing code. In, *The European Symposium on Satellite Remote Sensing* (pp. 9-20). Rome, Italy

Govaerts, Y.M., Jacquemoud, S., Verstraete, M.M., & Ustin, S.L. (1996). Three-dimensional radiation transfer modeling in a dicotyledon leaf. *Applied Optics, 35*, 6585-6598

Hosgood, B., Jacquemoud, S., Andreoli, G., Verdebout, J., Pedrini, G., & Schmuck, G. (1995). Leaf optical properties experiment 93 (LOPEX93). *Ispra Italy'European Commission, Joint Research Centre Institute of Remote Sensing Applications*

Jacquemoud, S., Bacour, C., Poilve, H., & Frangi, J.-P. (2000). Comparison of four radiative transfer models to simulate plant canopies reflectance: Direct and inverse mode. *Remote sensing of environment, 74*, 471-481

Jacquemoud, S., & Baret, F. (1990). PROSPECT: A model of leaf optical properties spectra. *Remote sensing of environment, 34*, 75-91

Jacquemoud, S., & Baret, F. (1993). Estimating vegetation biophysical parameters by inversion of a reflectance model on high spectral resolution data. In C. Varlet-Grancher, R. Bonhomme, & H. Sinoquet (Eds.), *Crop Structure and Light*

Microclimate: Characterization and Applications (p. 339−350): Institut National De La Recherche Agronomique

Jacquemoud, S., Ustin, S., Verdebout, J., Schmuck, G., Andreoli, G., & Hosgood, B. (1996). Estimating leaf biochemistry using the PROSPECT leaf optical properties model. *Remote sensing of environment, 56*, 194-202

Jacquemoud, S., Verhoef, W., Baret, F., Bacour, C., Zarco-Tejada, P.J., Asner, G.P., François, C., & Ustin, S.L. (2009). PROSPECT+ SAIL models: A review of use for vegetation characterization. *Remote sensing of environment, 113*, S56-S66

Jay, S., Bendoula, R., Hadoux, X., Féret, J.-B., & Gorretta, N. (2016). A physically-based model for retrieving foliar biochemistry and leaf orientation using close-range imaging spectroscopy. *Remote sensing of environment, 177*, 220-236

Jurdao, S., Yebra, M., Guerschman, J.P., & Chuvieco, E. (2013). Regional estimation of woodland moisture content by inverting radiative transfer models. *Remote sensing of environment, 132*, 59-70

Justice, C.O., Vermote, E., Townshend, J.R., Defries, R., Roy, D.P., Hall, D.K., Salomonson, V.V., Privette, J.L., Riggs, G., & Strahler, A. (1998). The Moderate Resolution Imaging Spectroradiometer (MODIS): Land remote sensing for global change research. *IEEE Transactions on Geoscience and Remote Sensing, 36*, 1228-1249

Koetz, B., Baret, F., Poilvé, H., & Hill, J. (2005). Use of coupled canopy structure dynamic and radiative transfer models to estimate biophysical canopy characteristics. *Remote sensing of environment, 95*, 115-124

Lam, H., & Rotman, S. (2010). Performance Verification of NIR Spectrophotometers. *Practical Approaches to Method Validation and Essential Instrument Qualification*, 177-199

Laurent, V.C., Schaepman, M.E., Verhoef, W., Weyermann, J., & Chávez, R.O. (2014). Bayesian object-based estimation of LAI and chlorophyll from a simulated Sentinel-2 top-of-atmosphere radiance image. *Remote sensing of environment, 140*, 318-329

Lavergne, T., Kaminski, T., Pinty, B., Taberner, M., Gobron, N., Verstraete, M.M., Vossbeck, M., Widlowski, J.-L., & Giering, R. (2007). Application to MISR land products of an RPV model inversion package using adjoint and Hessian codes. *Remote sensing of environment, 107*, 362-375

Le Maire, G., Francois, C., & Dufrene, E. (2004). Towards universal broad leaf chlorophyll indices using PROSPECT simulated database and hyperspectral reflectance measurements. *Remote sensing of environment, 89*, 1-28

Li, D., Cheng, T., Jia, M., Zhou, K., Lu, N., Yao, X., Tian, Y., Zhu, Y., & Cao, W. (2018). PROCWT: Coupling PROSPECT with continuous wavelet transform to improve the retrieval of foliar

chemistry from leaf bidirectional reflectance spectra. *Remote sensing of environment, 206*, 1-14

Nelder, J.A., & Mead, R. (1965). A simplex method for function minimization. *The computer journal, 7*, 308-313

Oguchi, R., Onoda, Y., Terashima, I., & Tholen, D. (2018). Leaf Anatomy and Function. *The Leaf: A Platform for Performing Photosynthesis* (pp. 97-139): Springer

Ollinger, S. (2011). Sources of variability in canopy reflectance and the convergent properties of plants. *New Phytologist, 189*, 375-394

Pedersen, P., Kumudini, S., Board, J., & Conley, S. (2004). *Soybean growth and development*. Iowa State University, University Extension Ames, IA

Pinty, B., & Verstraete, M.M. (1991). Extracting information on surface properties from bidirectional reflectance measurements. *Journal of Geophysical Research: Atmospheres, 96*, 2865-2874

Qu, Y., Wang, J., Wan, H., Li, X., & Zhou, G. (2008). A Bayesian network algorithm for retrieving the characterization of land surface vegetation. *Remote sensing of environment, 112*, 613-622

Reichstein, M., Bahn, M., Mahecha, M.D., Kattge, J., & Baldocchi, D.D. (2014). Linking plant and ecosystem functional biogeography. *Proceedings of the national academy of sciences, 111*, 13697-13702

Richardson, A.D., Duigan, S.P., & Berlyn, G.P. (2002). An evaluation of noninvasive methods to estimate foliar chlorophyll content. *New Phytologist, 153*, 185-194

Running, S.W., & Coughlan, J.C. (1988). A general model of forest ecosystem processes for regional applications I. Hydrologic balance, canopy gas exchange and primary production processes. *Ecological modelling, 42*, 125-154

Running, S.W., Nemani, R.R., Heinsch, F.A., Zhao, M., Reeves, M., & Hashimoto, H. (2004). A continuous satellite-derived measure of global terrestrial primary production. *AIBS Bulletin, 54*, 547-560

Schimel, D.S., Kittel, T.G., & Parton, W.J. (1991). Terrestrial biogeochemical cycles: global interactions with the atmosphere and hydrology. *Tellus B, 43*, 188-203

Serbin, S.P., Dillaway, D.N., Kruger, E.L., & Townsend, P.A. (2011). Leaf optical properties reflect variation in photosynthetic metabolism and its sensitivity to temperature. *Journal of Experimental Botany, 63*, 489-502

Sims, D.A., & Gamon, J.A. (2002). Relationships between leaf pigment content and spectral reflectance across a wide range of species, leaf structures and developmental stages. *Remote sensing of environment, 81*, 337-354

Smith, W.K., Vogelmann, T.C., DeLucia, E.H., Bell, D.T., & Shepherd, K.A. (1997). Leaf form and photosynthesis. *Bioscience, 47*, 785-793

Sun, J., Shi, S., Yang, J., Du, L., Gong, W., Chen, B., & Song, S. (2018). Analyzing the performance of PROSPECT model inversion based on different spectral information for leaf biochemical properties retrieval. *ISPRS Journal of Photogrammetry and Remote Sensing, 135*, 74-83

Suplick-Ploense, M., Alshammary, S., & Qian, Y. (2011). Spectral reflectance response of three turfgrasses to leaf dehydration. *Asian Journal of Plant Sciences, 10*, 67

Trumbore, S. (2006). Carbon respired by terrestrial ecosystems–recent progress and challenges. *Global Change Biology, 12*, 141-153

Ustin, S.L., Gitelson, A.A., Jacquemoud, S., Schaepman, M., Asner, G.P., Gamon, J.A., & Zarco-Tejada, P. (2009). Retrieval of foliar information about plant pigment systems from high resolution spectroscopy. *Remote sensing of environment, 113*, S67-S77

Ustin, S.L., Roberts, D.A., Gamon, J.A., Asner, G.P., & Green, R.O. (2004). Using imaging spectroscopy to study ecosystem processes and properties. *AIBS Bulletin, 54*, 523-534

Zadoks, J.C., Chang, T.T., & Konzak, C.F. (1974). A decimal code for the growth stages of cereals. *Weed research, 14*, 415-421

Zarco-Tejada, P.J., Rueda, C., & Ustin, S. (2003). Water content estimation in vegetation with MODIS reflectance data and model inversion methods. *Remote sensing of environment, 85*, 109-124

Zhang, C., Ren, H., Liang, Y., Liu, S., Qin, Q., & Ersoy, O.K. (2017). Advancing the PROSPECT-5 Model to Simulate the Spectral Reflectance of Copper-Stressed Leaves. *Remote Sensing, 9*, 1191

Zhao, F., Guo, Y., Huang, Y., Reddy, K.N., Lee, M.A., Fletcher, R.S., & Thomson, S.J. (2014). Early detection of crop injury from herbicide glyphosate by leaf biochemical parameter inversion. *International Journal of Applied Earth Observation and Geoinformation, 31,* 78-85

Table 1.1. Biochemical parameters used by the PROSPECT-5 model.

Symbol	Biochemical Parameter	Units
C_{cab}	Leaf chlorophyll content	µg cm^{-2}
C_{car}	Leaf carotenoid content	µg cm^{-2}
C_w	Equivalent water thickness	g cm^{-2}
C_m	Dry matter content	g cm^{-2}

Table 1.2. Summary of leaf structure parameter (N_s) metrics[1.]

Plant type	Total	Early	Mid	Late
Monocotyledon (n = 118)				
µ	1.46	1.35	1.5	1.66
σ	0.29	0.28	0.23	0.25
Max/Min	2.23/1.00	1.92/1.00	1.84/1.00	2.23/1.15
Upper/Lower IQ	1.68/1.27	1.57/1.03	1.70/1.39	1.73/1.52
Dicotyledon (n = 112)				
µ	2.07	2.17	1.96	2.14
σ	0.27	0.19	0.25	0.29
Max/Min	2.96/1.61	2.54/1.91	2.89/1.61	2.96/1.64
Upper/Lower IQ	2.21/1.86	2.26/2.05	2.04/1.81	2.36/1.96

[1]Stratified by species and phenological class. The 75th and 25th percentiles are the upper and lower interquartile (IQ) limits, respectively.

Table 1.3. Welch's two-sample t-test and analysis of variance. [1.]

Data	Independent variable	F-value	T-statistic
All	Species*		10.93 (< 0.001)
Monocotyledon	Season period*	10.227 (< 0.001)	
	2015 Irrigation regime	0.896 (0.413)	
	2016 Irrigation regime		-1.122 (0.271)
Dicotyledon	Season period*	4.46 (0.017)	
	2015 Irrigation regime	2.422 (0.101)	
	2016 Irrigation regime		-1.251 (0.22)

[1]Welch's two-sample t-test and analysis of variance for species, phenological class, and irrigation regime sub-populations. ANOVA results are presented in the first two columns after the independent variable column. Two-sample t-test results are presented in the last two columns. The independent variable name is asterisked if the difference between population means are significant ($P < 0.05$).

Table 1.4 Welch's two-sample t-test. [1.]

Population	Independent variable	T-value	df	Probability of > T
Monocotyledon	Early vs Mid*	-2.486	88	0.015
	Mid vs Late*	-2.626	58	0.011
	Early vs Late*	-4.912	84	<0.001
Dicotyledon	Early vs Mid*	3.002	59	0.004
	Mid vs Late*	-3.3	95	0.001
	Early vs Late	0.373	64	0.71

[1]Results from Welch's two-sample t-test. The independent variable name is asterisked if the difference between population means are significant ($P < 0.05$).

Days after seeding	0	5	10	15	20	25	30	35	40	45	50	55	60	65	70	75	80	85	90
Soy	VE		VC		V1	V2	V3	V4	V5	V5	V6	R1	R2		R3		R4		
	Early							**Mid**						**Late**					
Wheat (Red and White)	10	11	13	15	20	25	33	37	39	43	47	55	61	71	85	87	89		
	Early									**Mid**				**Late**					
Upland Rice	Seeding				Early tillering			Late tillering						Flowering					
	Early													**Mid**					

Figure 1.1. Phenological aggregation into three classes for the species considered in this study. For each species, the top line reports the observed crop growth stage recorded using commonly used growth stage identification protocols. Growth phases and durations, outlined by Arraudeau and Vergara (1988), were used for identifying phenological stages of upland rice. The soy was identified using the protocol outlined by Pedersen et al. (2004). Both red and white varieties of wheat followed the Zadok's code (Zadoks et al. 1974). The bottom row of each species row reports the phenological aggregation.

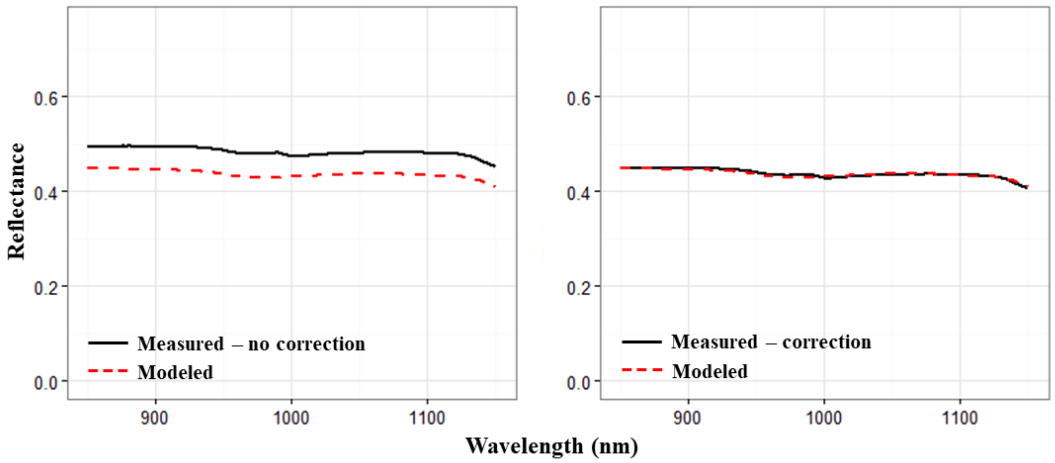

(**a**) (**b**)

Figure 1.2. Comparison between measured and modeled leaf spectra in the NIR region (850–1150 nm): (**a**) before PROREF adjustment; (**b**) after PROREF adjustment. The dashed red line represents the modeled leaf spectra as output from PROSPECT-5. The solid black line represents the measured wheat leaf spectra. The modeled leaf spectra were generated for this example figure with the biochemical input parameters measured from a wheat leaf sample: C_w = 0.016, C_m = 0.004, and N = 1.38.

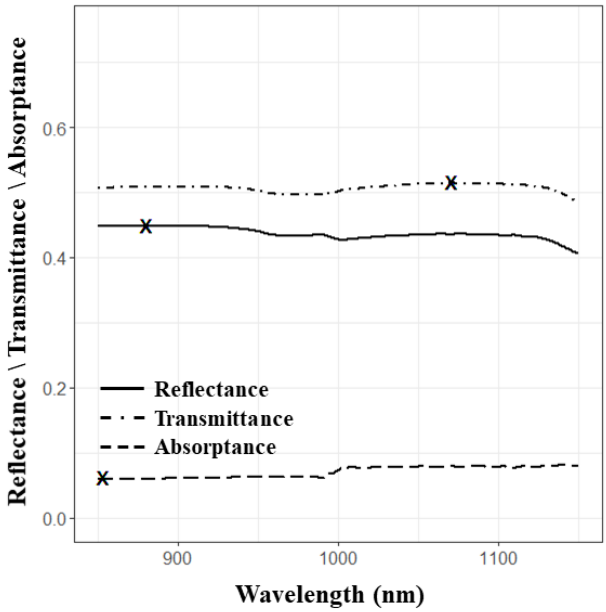

Figure 1.3. Comparison between measured reflectance and transmittance, and estimated absorptance (absolute difference between reflectance and transmittance) in the NIR region (850–1150 nm) of the wheat leaf from Figure 1. The black 'X's mark the approximate locations of maximum reflectance (λ_1 = 880 nm) and transmittance (λ_2 = 1071 nm), and minimum absorptance (λ_3 = 853 nm) in the NIR region.

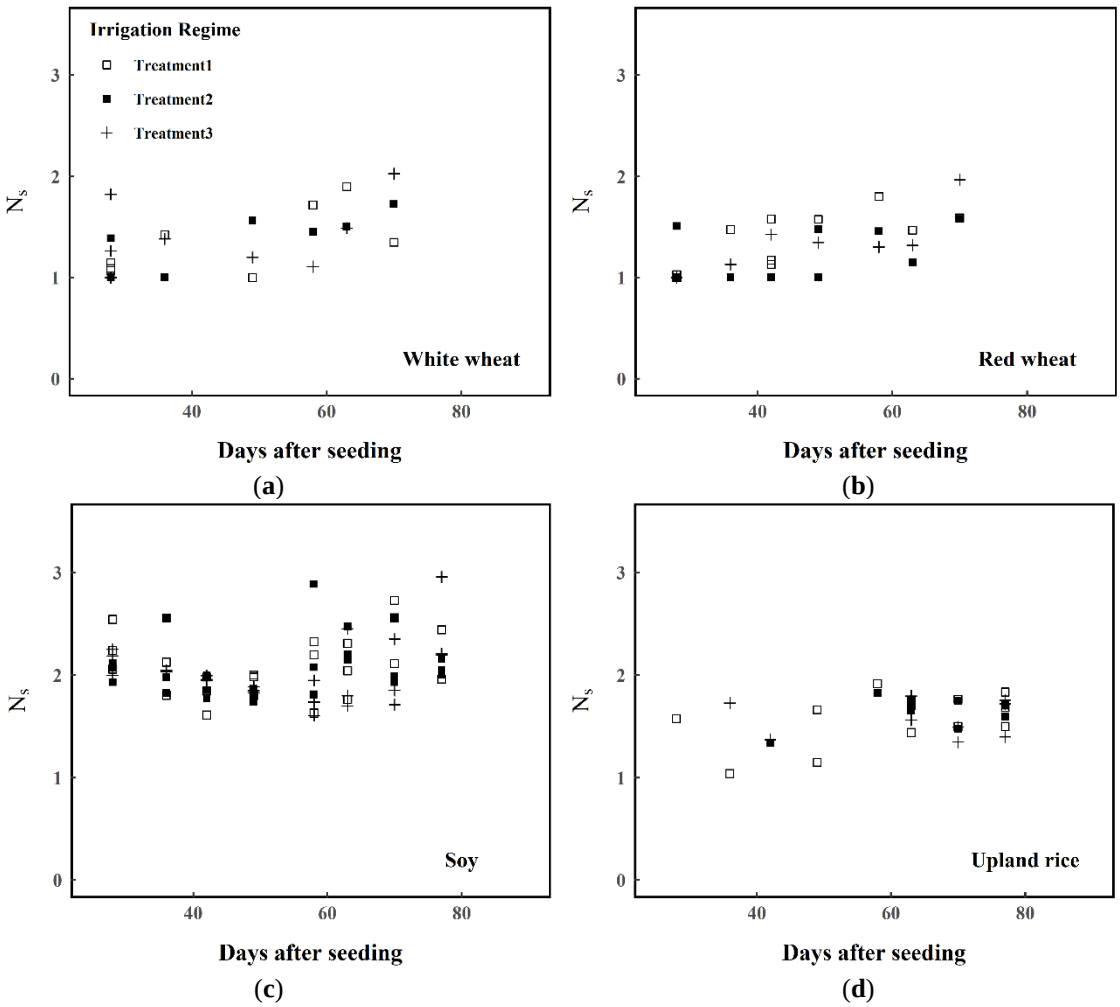

Figure 1.4. Estimated N_s for the entire sample of the four species grown in the 2015 experiment: (**a**) white wheat; (**b**) red wheat; (**c**) soy; (**d**) upland rice. In all four plots, the symbol indicates the three different irrigation regimes: Treatments 1, 2, and 3 indicate respectively watering when the plant tray reached 85%, 75%, and 60% of the initial saturated weight.

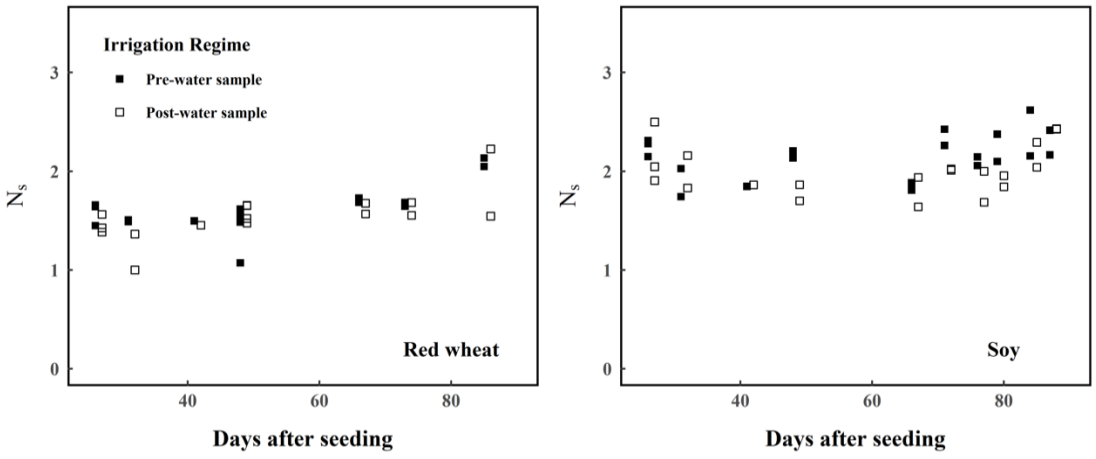

(**a**) (**b**)

Figure 1.5. Estimated N_s for the entire sample of the two species grown in the 2016 experiment: (**a**) red wheat; (**b**) soy. In each plot, the symbol indicates the two different irrigation regimes: Pre-water samples indicate estimated N_s before the trays were watered and post-water samples indicate estimated N_s 24-hours after the plants were watered.

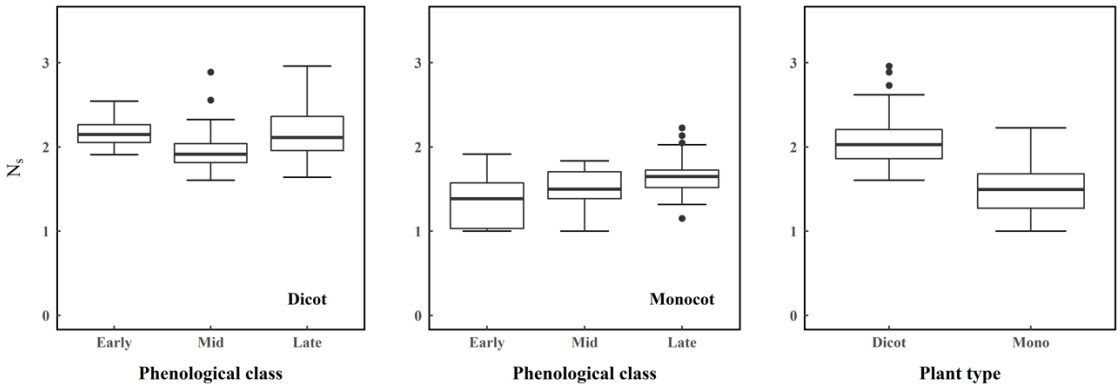

Figure 1.6. Box plots of the distribution of N_s as a function of plant type and phenological class: (**a**) dicotyledon soy during the 2015 and 2016 experiments for each phenological class; (**b**) monocotyledon wheat (hard red, soft white) and upland rice during the 2015 and 2016 experiments for each phenological class; (**c**) both dicotyledon and monocotyledon plant types during both 2015 and 2016 experiments for the entire season period. The box plots report median, interquartile range (IQR), whiskers (defined by: Q3 + 1.5 *IQR and Q1-1.5*IQR), and outliers (dots).

Chapter 2: Landsat-8 and Sentinel-2 canopy water content estimation in croplands through radiative transfer model inversion

Published in *Remote Sensing* as:

Boren, E.J. and Boschetti, L., 2020. Landsat-8 and Sentinel-2 Canopy Water Content Estimation in Croplands through Radiative Transfer Model Inversion. Remote Sensing, 12(17), p.2803.

Abstract

Despite the potential implications of a cropland canopy water content (CCWC) thematic product, no global remotely sensed CCWC product is currently generated. The successful launch of the Landsat-8 Operational Land Imager (OLI) in 2012, Sentinel-2A Multispectral Instrument (MSI) in 2015, followed by Sentinel-2B in 2017, make possible the opportunity for CCWC estimation at a spatial and temporal scale that can meet the demands of potential operational users. In this study, we designed and tested a novel radiative transfer model (RTM) inversion technique to combine multiple sources of *a priori* data in a look-up table (LUT) for inverting the NASA Harmonized Landsat Sentinel-2 (HLS) product for CCWC estimation. This study directly builds on previous research for testing the constraint of the leaf parameter (N_s) in PROSPECT, by applying those constraints in PRO4SAIL in an agricultural setting where the variability of canopy parameters are relatively minimal. In total, 225 independent leaf measurements were used to train the LUTs, and 102 field data points were collected over the 2015–2017 growing seasons for validating the inversions. The results confirm increasing *a priori* information and regularization yielded the best performance for CCWC estimation. Despite the relatively low variable canopy conditions, the inclusion of N_s constraints did not improve the LUT inversion. Finally, the inversion of Sentinel-2 data outperformed the inversion of Landsat-8 in the HLS product. The method demonstrated ability for HLS inversion for CCWC estimation, resulting in the first HLS-based CCWC product generated through RTM inversion.

Introduction

Agricultural drought, defined as the deficiency of soil moisture required for proper plant growth resulting in plant stress and yield reduction (Hazaymeh and Hassan 2016), is primarily monitored using agricultural drought indices (Zargar et al. 2011). Along with temperature, precipitation, and soil moisture content, vegetation (cropland) canopy water content (CCWC) is a known key parameter for monitoring agricultural drought due to its close relation to vegetation stress, biomass productivity, and nutrient transportation (Peñuelas et al. 1993; Peñuelas et al. 1994; Yi et al. 2014). Although agricultural drought monitoring is important throughout the entire growing season (Hazaymeh and Hassan 2016), it is especially critical during growth periods where water shortages could result in significant loss of

yield (Hu et al. 2008; Zhang et al. 2017). In irrigation-fed agricultural regions, CCWC is critical information for implementing flexible precision irrigation practices (Peñuelas et al. 1993; Ustin et al. 2004). This is increasingly relevant, as growers seek to improve efficiency through the adoption of advanced irrigation technologies, which rely on precise, geographically distributed monitoring of water in- and out-flows from farm to basin scale (Grafton et al. 2018). The spaceborne remote sensing of CCWC eliminates the need for expensive, labor intensive field measurements, and minimizes uncertainties caused by within-field variations in soil type and microtopography (Liu et al. 2008; Rud et al. 2014). Further development of remote sensing methods for CCWC assessment, is therefore of paramount importance.

Remote sensing techniques for the estimation of CCWC have been proposed relying on thermal, microwave, and optical data (Carlson et al. 1994; Peñuelas et al. 1993; van Emmerik et al. 2015). The detection of apparent thermal inertia through remote sensing by measuring surface albedo and the diurnal temperature range has been observed to have a proportional relationship with water content (Claps and Laguardia 2004; Verstraeten et al. 2006), although these methods perform poorly in heavily vegetated regions (Peters et al. 2011). Microwave remote sensing methods for land surface water detection (Entekhabi et al. 2010; Jackson et al. 1982; Meesters et al. 2005) show promising results for the detection of water content in agricultural drought monitoring applications (Anderson et al. 2010; Zhang and Jia 2013), albeit lacking the combined temporal and spatial resolution required for operational agricultural applications (Hazaymeh and Hassan 2016). The use of optical data relies primarily on the strong water absorption features in the 700–2500 nm spectral range. The increasing availability of moderate resolution (10–30 m) optical data, the development of data assimilation techniques for filling data gaps and decreasing space-borne product uncertainty (Kumar et al. 2015; Kumar et al. 2018), open the possibility of developing CCWC thematic products to meet the needs of operational users (Belward et al. 2016; Djamai et al. 2019; Zhang et al. 2013).

Optical-based estimation of water content typically involve empirical methods, relying on statistical relationships between field measured CCWC and water sensitive spectral indices (Bandyopadhyay et al. 2014; Cheng et al. 2008; Ullah et al. 2014). The normalized difference water index (NDWI) (Gao 1996) has been found to be one of the most robust indices for detecting variations in vegetation water content and biomass (Cosh et al. 2010). A major limitation of these approaches is the fact that the relationship between CCWC and spectral indices is highly dependent upon field sampling methods, imagery preprocessing quality, and on the choice of the statistical model used (Grossman et al. 1996; Li and Wang 2011; Yebra et al. 2013). Transferability of empirical methods, required for systematic large-scale application, is further limited due to region-specific variations in

vegetation species, canopy properties, and soil properties (Baret and Guyot 1991; Jacquemoud et al. 2009; Verger et al. 2011).

The inversion of radiative transfer models (RTM) provides a physically-based alternative to the empirical methods. RTMs can potentially be transferred among different regions, since they explicitly model the interaction between electromagnetic energy and vegetation biophysical components; thereby, limiting the uncertainty caused from variations in surface properties (Darvishzadeh et al. 2008b; Houborg et al. 2007; Si et al. 2012). The PROSAIL coupled RTM (Baret et al. 1992), is an extensively used model (Duan et al. 2014; Jay et al. 2017; Rivera et al. 2013) which generates top-of-canopy bidirectional reflectance and is known for representing homogenous landscapes well (Jacquemoud et al. 2009). PROSAIL is the result of combining the leaf Propriétés Spectrales model (PROSPECT) and the Scattering by Arbitrarily Inclined Leaves model (SAIL), where the output of PROSPECT is used as an input in SAIL (Figure 2.1).

The PROSPECT model, which simulates hemispherical reflectance and transmittance between 400‑2500 nm of a leaf (Jacquemoud and Baret 1990), is based on the plate theory model (Allen et al. 1969) where a leaf can be conceptualized as one or multiple compact absorbing plates. The model calculates the radiative transfer of energy at the surface and inside the leaf with two classes of user input variables: 1) the leaf structure parameter (N_s) which is the number of homogenous layers (or plates) specifying the number of cell wall interfaces within the plant leaf mesophyll and 2) the biochemical components of the leaf: the properties which the absorption coefficient of each plate is derived. Several versions of the model have been published since first introduced in 1990 (Jacquemoud et al. 2000; Jacquemoud and Baret 1990; Jacquemoud et al. 1996; Le Maire et al. 2004); the most recent improvements with the release of PROSPECT-5 (Féret et al. 2008) and PROSPECT-D (Féret et al. 2017), which separates total carotenoids and anthocyanins from total pigment content, respectively. The input parameters to PROSPECT-5 are leaf structure parameter N_s (unitless), leaf chlorophyll a + b concentration C_{cab} (µg cm^{-2}), carotenoid concentration C_{car} (µg cm^{-2}), equivalent water thickness C_w (g cm^{-2}), and dry matter content C_m (g cm^{-2}).

SAIL is a one-dimensional RTM which simulates canopy bidirectional reflectance as a function of leaf reflectance and transmittance, soil reflectance, canopy architectural properties, and illumination/viewing geometries (Verhoef 1984). SAIL considers the canopy as a horizontal, turbid medium made up of randomly distributed leaves; where the azimuth angle of the leaves is assumed to be randomly distributed, and their zenith angle characterized by a mean leaf inclination input. Like PROSPECT, SAIL has been numerically optimized resulting in the 4SAIL model (Verhoef et al. 2007). The input parameters to 4SAIL are leaf reflectance and transmittance, leaf area index (LAI) (m^2 m^{-2}),

canopy background reflectance, (i.e., soil reflectance scale parameter), leaf angle distribution from average leaf angle ALA (unitless) [54], fraction of diffuse incoming solar radiation *skly* (unitless), sun zenith angle θ_s (deg), sensor viewing angle θ_v (deg), relative azimuth angle between the sensor and sun φ (deg), and the hot-spot size parameter *HotS* (m m^{-1}) (Kuusk 1995).

PRO4SAIL inversion is performed by using known values of surface reflectance (i.e., the satellite observations) to estimate the values of the unknown leaf biochemical parameters and/or canopy structural parameters. PRO4SAIL inversion for estimating CCWC (calculated as the product of C_w and LAI) is most commonly utilized in agricultural (Yang and Ling 2004; Zhang et al. 2017) and fire danger assessment applications (Colombo et al. 2008; Yebra et al. 2013; Zarco-Tejada et al. 2003). The systematic generation of agricultural monitoring thematic products derived from RTM inversion, however, has been limited in the past both by the ill-posed nature of the inversion problem (Baret and Buis 2008; Combal et al. 2003; Yebra and Chuvieco 2009) and by the lack of optical space-borne instruments with spatial, temporal, and spectral resolution adequate to meet the needs of operational agricultural monitoring (Atzberger 2013; Becker-Reshef et al. 2010).

Inversion problems are ill-posed as more than one solution typically exists (Baret and Buis 2008; Combal et al. 2003), primarily due to the number of unknown variables exceeding the number of observed variables (Jacquemoud et al. 1995). Specifically, model parameters which influence the same spectral region contribute to this uncertainty, causing more than one combination of parameters to produce very similar spectral outputs (Weiss et al. 2000). In the case of C_w retrieval in PROSPECT inversion, Ceccato, et al. (2001) demonstrated the coupled influence of C_m and N_s with C_w in the SWIR region; thereby, illustrating that the observed SWIR reflectance alone does not provide sufficient information to invert the model and estimate C_w. PRO4SAIL inversion solving is further complicated by the fact that SAIL introduces additional parameters to model the top-of-canopy reflectance (Figure 2.1).

Various strategies have been proposed and implemented to constrain the number of viable solutions; thereby, alleviating the ill-posed nature of the inversion. Spatial constraints have been applied by splitting the inversion problem into separate landcover sub-domains (Dorigo et al. 2009; Laurent et al. 2013; Verrelst et al. 2012). Temporal constraints have also been utilized when a time series of images are available (Houborg et al. 2007; Lauvernet et al. 2008), and have demonstrated to improve inversion performance by constraining parameter variability through accounting of image acquisition periods (Koetz et al. 2007). Finally, statistical constraints, which consider typical parameter ranges and distributions (Darvishzadeh et al. 2008a; Si et al. 2012), as well as their intercorrelations (Féret et al.

2011; Quan et al. 2015), have been utilized to lower inversion uncertainty through the collection of *a priori* information (Combal et al. 2003).

The N_s parameter in PROSPECT has been identified as a primary source of uncertainty in estimating leaf reflectance and transmittance (Ceccato et al. 2001) as it is the only parameter that cannot be directly measured, or easily correlated to other measurable parameters (Ceccato et al. 2001; Ollinger 2011), yet little has been done to constrain the parameter in PRO4SAIL inverse problems for a few reasons. First, constraining the N_s parameter would likely prove to be fruitless in areas where species composition and canopy architectures are diverse since the distribution of leaf-level N_s within the canopy would likely be highly variable. Second, overall PRO4SAIL top-of-canopy reflectance has been demonstrated to be less sensitive to variations of N_s as compared to LAI, ALA, and the soil reflectance parameter (Jacquemoud et al. 2009). Because croplands have a relatively homogenous species composition and canopy architecture, however, the range of possible LAI and ALA values is narrower than in natural vegetation; thereby, limiting their overall impact on the model output. Similarly, other characteristics of croplands may translate into limited sensitivity to LAI in PRO4SAIL. Most notably, there is some saturation, especially in the near infrared (NIR) and short wave infrared (SWIR) spectral regions, for LAI greater than two (Bacour et al. 2002a), which is not uncommon in croplands. Further relevant for the inversion of PRO4SAIL in croplands, is the fact that in dense vegetation (i.e., LAI greater than two) the background reflectance from soil is completely masked (Bacour et al. 2002b).

In addition to the specific model inversion issues, agricultural monitoring through remote sensing requires the availability of data acquired with adequate spatial and temporal resolution (Asner et al. 2011; Baret et al. 2007; Martin et al. 2008; Whitcraft et al. 2015a; Whitcraft et al. 2015b). Because of the rapid changes in plants during the growing season, coarse spatial resolution instruments with daily or near-daily temporal resolution, such as the moderate resolution imaging spectroradiometer (MODIS) or the medium resolution imaging spectrometer (MERIS), were until recently the only potential data source for operational crop monitoring, even though their spatial resolution, much coarser than the average field size in most countries, was a severe limitation to their practical use (Atzberger 2013; Fritz et al. 2015). Similarly, the potential for operational agricultural applications of the ocean and land colour instrument (OLCI) onboard Sentinel-3, designed as the successor to MERIS, is limited by the coarse spatial resolution.

The successful launch of the Landsat 8 Operational Land Imager (OLI) in 2012, Sentinel 2A multispectral instrument (MSI) in 2015, Sentinel 2B MSI in 2017, and the systematic acquisition schedule and free data distribution policy of both missions create unprecedented opportunities for meeting the demands of agricultural monitoring, especially when assimilated with other remote sensing

products. The newly available NASA Harmonized Landsat-Sentinel (HLS) product is the combination of both data sets through atmospheric, radiometric, and geometric corrections (Claverie et al. 2018; Claverie et al. 2016), and has the advantage of frequent revisits (2–3 days over the entire globe) (Li and Roy 2017) while maintaining a spatial resolution (30 m resolution), both of which are necessary for capturing short-term environmental conditions. Thanks also to constantly increasing computing power, these new data sources make it possible to envision moderate resolution operational agricultural monitoring systems (Fritz et al. 2019), placing a greater emphasis on the development of methods and algorithms for the systematic generation of physically-based remotely sensed thematic products.

In this study, we propose and test a methodology for the generation of a multi-temporal CCWC product from the time series of Landsat-8 and Sentinel-2 HLS reflectances, through look-up table (LUT) inversion of PRO4SAIL. The uncertainty of the CCWC retrievals is reduced by constraining the possible values of PRO4SAIL parameters combining spatial, temporal, and statistical ancillary and *a priori* information, including crop types from the USDA Crop Data Layer (CDL) product, LAI from the MODIS MCD15A2 product, and crop-specific ranges of N_s, C_w, and C_m values from field measurements (Boren et al. 2019). In order to establish a baseline for the assessing the performance of the proposed methodology (henceforth, "Strategy 3"), two alternative inversion strategies were also considered: a minimally constrained inversion, where no crop-specific information is used and the possible range of all parameters is derived from literature (henceforth, "Strategy 1"), and a partially constrained inversion, where values of N_s values from Boren et al. (2019) are used (henceforth, "Strategy 2"). This paper therefore also assesses whether the use of N_s values stratified by phenology (early, mid, and late season) and crop type (monocotyledon and dicotyledon) improves the inversion of CCWC in croplands.

The results are validated by comparing the estimated CCWC with a new, extensive set of field measurements acquired over three growing seasons. The validation data are more representative of the complete phenological cycle of multiple crops species than those used in previous PRO4SAIL inversion validation studies. The results and implications for systematic CCWC retrieval using the HLS-product are presented and discussed, including the future directions for CCWC HLS-product incorporation into the existing agricultural monitoring framework.

Methods and Materials

Study area

The study area, covering an extent of 8 km x 8 km, is located south of Genesee (Idaho) in the Palouse Prairie bioregion of the Western United States (Figure 2.2). The bioregion covers a large area

(~16,000 km^2) in southeastern Washington, west central Idaho, and northeastern Oregon, and is characterized by a series of loess-covered basalt tablelands with moderate to high relief ranging in altitude from 370 to 1800 m **(**Bailey 1995**)**. The study region is agriculturally productive, with wheat yields occasionally exceeding 7000 kg ha^{-1} (Papendick 1996). The climate is characterized by hot, dry summers followed by wet and relatively warm winters: typically, between 60% and 70% of the annual precipitation occurring between November and April (Cox et al. 2001). Once a widespread prairie composed of perennial grasses such as Blue bunch wheatgrass (*Pseudoroegneria spicata*) and Idaho fescue (*Festuca idahoensis)*, today it is virtually entirely converted to croplands. Three full growing seasons (2015–2017) are considered in the study.

Remotely sensed data and ancillary products

Harmonized Landsat Sentinel surface reflectance data

The Harmonized Landsat Sentinel product (HLS) consists of surface reflectances from the Landsat-8 Operational Land Imager (OLI) and Sentinel-2 Multispectral Instrument (MSI) virtual constellation of moderate resolution satellite systems. The most recent HLS version 1.4 product was used as input data for the PRO4SAIL inversion. The "harmonization" of Landsat-8 and Sentinel-2 occurs through a set of algorithms which involves re-gridding the data to a common 30 m georeferenced grid, atmospheric correction, bidirectional reflectance distribution function (BRDF) correction and normalization to nadir viewing geometry, and spectral bandpass adjustment (Claverie et al. 2018).

The images were accessed through the NASA Harmonized Landsat Sentinel-2 FTP (accessed via: hls.gsfc.nasa.gov). The spectral bands included in the HLS product are presented in Table 2.1. The HLS product is distributed in the Sentinel-2 tiling geometry; the 8 km by 8 km study area is located within the 11TNM HLS tile. Every available HLS product for the study area was acquired for 2015–2017.

PRO4SAIL illumination and viewing geometry parameters

PRO4SAIL requires illumination and viewing parameters (Figure 2.1), that were extracted from the HLS metadata of each image. The Sun zenith angle (θ_s), provided in the HLS metadata for the center of the tile (Zhang et al. 2016), was kept constant throughout the study area; this is a reasonable approximation given the negligible variation of θ_s in a tile. The viewing zenith angle (θ_v) was set to 90˚, because the HLS product is normalized to nadiral conditions. Because azimuthal geometry is inconsequential on BRDF for a nadir viewing angle (Roy et al. 2016), the sun-sensor azimuth parameter (φ) was set to a fixed value of 0. Previous analysis has established that the hotspot is always located

outside the Landsat-8 and Sentinel-2 swath for overpasses at the latitude of the study region (Li et al. 2017; Zhang et al. 2016**)**. Because our plots were located well outside of the hotspot configuration, and in the interest of limiting free parameters in the inversion, the model was applied by assuming non-hotspot conditions. In this study we used the default value of fraction of diffuse incoming solar radiation (*skyl*) recommended in PRO4SAIL, namely the value proposed by François et al. (2002).

MCD15A2H LAI product

The Collection 6 MODIS MCD15A2H *LAI* 8-day composite product at 500-m resolution (Myneni et al. 2015) was used for to constrain the range of LAI values for the LUT generation. The MCD15A2H product is derived exploiting the MODIS red (648 nm) and near-infrared (858 nm) bands using a LUT-based procedure which is generated with a three-dimensional radiation transfer equation (Knyazikhin et al. 1998**)**. The product is generated daily at 500 m spatial resolution and composited using the most suitable pixels available within the 8-day acquisition periods of both MODIS sensors, Terra, and Aqua. All MCD15A2H LAI products for tile h09v04 that encompasses the study area were downloaded for the 2015–2017 growing seasons.

Cropland Data Layer (CDL) product

The United States Department of Agriculture (USDA) National Agricultural Statistics Service (NASS) geospatial Cropland Data Layer (CDL) product is a 30 m resolution, geo-referenced, crop-specific landcover classification layer which is annually updated and publicly available. CDL production is performed using decision tree supervised classification of satellite imagery, including Landsat-8 and Disaster Monitoring Constellation satellite data, for all 48 conterminous states. The thematic landcover map includes over 110 different crop categories with mapping accuracies for major crops in large production states ranging from 85% to 95% (Boryan et al. 2011). The CDL product and crop mask is distributed through the NASS online CropScape tool for 2015–2017 (Han et al. 2012).

Field sampling dataset

Leaf-level parameters

An extensive experimental data collection was conducted to acquire leaf measurements (Boren et al. 2019) used for constraining N_s, C_w, and C_m. Detailed information about the controlled experiment and sampling relevant to N_s is reported in Boren et al. (2019). The sampling methodology for C_w and C_m is summarized in this section.

Four crop species were grown at the University of Idaho Pitkin's forest research nursery during the summers of 2015 and 2016: three monocotyledons (hard red wheat, *Triticum durum* Desf.,

soft white wheat *Triticum aestivum* L., and upland rice, *Oryza sativa* L.) and one dicotyledon (soy, *Glycine max* L.). Leaf area, fresh weight, and dry weight measurements were taken at the same frequency of spectral measurements and from the same samples in Boren et al. (2019). The leaf area measurement protocol was adapted from (Fladung and Ritter 1991), scanning all the leaves of the sample with a flatbed scanner (Epson 4490 Photo Scanner) to measure the total leaf area [cm^2]. The total fresh weight (g) of all the leaves was measured immediately after measuring the leaf area, and the total dry weight (g) was measured after drying at 60 ºC for 48 h. C_w (g cm^{-2}) for each leaf sample was measured using Equation (1), and C_m (g cm^{-2}) was measured using Equation (2):

$$C_w = \frac{FW - DW}{LA}, \quad (1)$$

$$C_m = \frac{DW}{LA}, \quad (2)$$

where *FW* (g) and *DW* (g) are the average fresh and dry weights of the leaves, and *LA* (cm^2) is the corresponding plot average leaf area. The distributions of C_w and C_m from the leaf measurements are presented in Figure 2.3.

LAI and leaf water content

Field measurements of LAI and C_w were collected on a number of 30 m × 30 m plots, over the course of three years (2015 to 2017) during the entire crop season of the study area (April–September); thus, ensuring that the dataset captures the full range of water content and phenological stages of the vegetation. Samples were collected from crops which were aggregated into three crop type groups: dicotyledon (Garbanzo fields), spring monocotyledon (Barley), and winter monocotyledon (Winter Wheat).

Each plot corresponds to a single 30 m × 30 m pixel in the HLS product grid; all field measurements were conducted on Landsat-8 and Sentinel-2A overpass days, within 1 h of the overpass time. Because the study area is located in the overlap region of neighboring Landsat-8 and Sentinel-2A paths, up to two Landsat-8 acquisitions were available every 16 days (every 7 and 9 days) and two Sentinel-2A acquisitions every 10 days.

To ensure that field measurements could be meaningfully compared to remotely sensed data, the site sampling followed a "scaled up" approach adapted from the sampling methods used in the VALERI field campaigns (Baret 2016). For each plot, 17 sample locations were established along the perimeter and on two transects, as illustrated in Figure 2.4.

At each sample location, LAI was estimated, and fresh leaf material was destructively extracted; for wheat and barley, one stem was removed, while for garbanzo, one average leaf was extracted from the top of the plant. Leaf quality, size, and health were considered when selecting for an average leaf. After extraction, leaf material was bagged, and put in a cooler for further processing in the lab.

The PocketLAI® smartphone app was used for the estimation of LAI. A Samsung Galaxy Rugby Pro™ 5-megapixel camera was used for image collection below the canopy at each sampling location; LAI was estimated from the images using the 57.5˚ gap fraction algorithm (Francone et al. 2014).

Upon returning to the lab, garbanzo leaves were scanned using a leaf scan protocol adapted from Fladung and Ritter (1991) to calculate the average leaf area. Wheat and barley average leaf area was determined instead by dividing LAI by the plant population density (# plants m^{-2}) using the density information provided by the grower. The fresh leaf weight was recorded and divided by the number of samples for an average fresh leaf weight. Leaves were dried in an oven at 60 ˚C for 48 h and weighed again to determine average dry leaf weight. Average plot C_w was calculated using Equation (1). CCWC was calculated using:

$$\mathrm{CCWC} = \mathrm{C_w} \text{ x } \mathrm{LAI} \quad (3)$$

where C_w is leaf water content calculated from (1) and *LAI* (m^2 m^{-2}) is leaf area index. The units for CCWC are (g m^{-2}).

Field plot data points corresponding to missing, poor quality or cloudy HLS acquisitions were discarded using the HLS data quality assessment (QA) band (Claverie et al. 2016) and excluded from further analysis. Observations with low, average, and high aerosol quality were retained, while observations labeled as cloud shadow, adjacent cloud, cloud, or cirrus were rejected. A summary of the field sampling plots is presented in Tables 2 and 3. In total, 102 CCWC field data points were retained.

Methods

An integrated (spatial, temporal, and statistical) PRO4SAIL inversion strategy workflow was designed and implemented using HLS reflectances as the primary input, and the accuracy of the resulting CCWC product was validated using the CCWC field reference dataset. A conceptual diagram, which illustrates the processing flow of the integrated strategy, is presented in Figure 2.5.

The inversion is performed adopting a LUT approach, which is conceptually simple and widely used in RTM inversion (Combal et al. 2002; Darvishzadeh et al. 2008b; Weiss et al. 2000). In the first

step, a comprehensive database of possible values of the input variables is compiled, based on *a priori* information, and the model is run in forward mode to generate corresponding modeled reflectance values (i.e., the look-up table). The inversion is then performed by minimizing the difference between the observed and modeled reflectance using a cost function, then retrieving the corresponding value of the biophysical parameters from the table.

To determine the effectiveness of the proposed integrated LUT inversion strategy, two other LUT generation strategies were carried out and analyzed. The various strategies are outlined in detail in the LUT generation section. Details about the spectral pre-processing and inversion cost-function is presented in the spectral pre-processing and LUT inversion section. Finally, the metrics of success for validation of the various strategies are presented in the validation section.

While the individual components of the constraining and inversion strategies used in this paper have been used in previous studies, this is the first study to comprehensively compare them on the same dataset, and the first study to perform CCWC inversion using HLS data. Furthermore, this study directly builds on the results of Boren et al. (2019), evaluating the effectiveness of constraining LUT inversion of field-level parameters by stratifying N_s as a function of crop type and phenology.

LUT generation

In this study, a LUT size of 100,000 was selected as a compromise between computing resource requirement and inversion accuracy (Weiss et al. 2000**)**. Probability distributions were used to generate a range of parameter values for running the coupled model in the forward mode, using three strategies that increasingly incorporate *a priori* knowledge and ancillary datasets to constrain the possible values of the parameters. The three strategies, including the key elements of constraint, are summarized in subsections 1, 2, and 3, respectively. All the relevant parameter value constraints for each strategy is presenting in Table 4. Additional relevant information related to constraints of strategy 2 and strategy 3 are presented in Tables 2.5 and 2.6.

For each realization of the set of input parameters, the PRO4SAIL model was run in forward mode, resulting in simulated spectral reflectances. The coastal aerosol, water vapor, and cirrus HLS bands were excluded from LUT generation and inversion because they do not contain relevant spectral information for the retrieval of *CCWC.*

Strategy 1: Single LUT from nominal range of the parameters:

A single LUT, of a size of 100,000, with gaussian distributions of inputs for leaf-level C_{cab}, C_{car}, C_w, and C_m was generated for strategy 1. The probability distributions of the pigment parameters,

C_{cab} and C_{car}, were characterized using basic statistics retrieved from 17 independent leaf datasets, which contain biophysical information from a large range of species, growing conditions, and developmental stages (Féret et al. 2011). The gaussian probability distributions of C_w and C_m were generated using the leaf measurements described in Section 2.1.3. ALA was minimally constrained using nominal *a priori* knowledge for the study region and plants. N_s values were generated in a uniform distribution using a previously characterized reasonable range between 1.0 and 4.0 (Ceccato et al. 2001).

In PRO4SAIL, the soil reflectance for 4SAIL is governed by a user input soil coefficient (value between 0 and 1) which scales two archived soil reflectance endmember signatures (400–2500 nm), dry and wet soil, in a linear mixture model:

$$\rho\text{soil}(\lambda) = \alpha\text{soil x } \rho\text{soil}_{\text{dry}}(\lambda) + (1 - \alpha\text{soil }) \text{ x } \rho\text{soil}_{\text{wet}}(\lambda) \quad (4)$$

where $\rho soil$ is the soil reflectance at wavelength λ, $\alpha soil$ is the user input soil coefficient, $\rho soil_{dry}$ and $\rho soil_{wet}$ is the reflectance of dry and wet soil, respectively. In this study, the wet and dry soil endmember spectral data provided with the model was used (accessed via: teledetection.ipgp.jussieu.fr).

Strategy 2: Phenology-specific LUTs with constrained N_s:

The second strategy uses the same probability distribution of C_{cab}, C_{car}, C_w, C_m, ALA, and $\alpha soil$ as strategy 1 but uses crop type and phenological stage dependent values for the N_s parameter. Since it is known that the N_s parameter varies with species and phenology (Boren et al. 2019; Jacquemoud et al. 1996), strategy 2 is designed to assess the effectiveness of constraining the N_s parameter based on crop species and phenological class. The N_s parameter was constrained by using the values, stratified by crop type and phenological stage, presented in Boren et al. (2019). Three separate LUTs, with 100,000 realizations each, were generated, based on the observed range of the N_s parameter (Table 6): one LUT for monocotyledons in the early development stage (N_s between 1.0 and 1.5), one for monocotyledons in the mid and late development stages (N_s between 1.5 and 2.0), and one for dicotyledons in all stages (N_s between 2.0 and 2.5).

To spatially stratify the study area for constraining the inversion based on crop type, the USDA CDL landcover classes were aggregated into the three crop type classes (spring monocotyledon, winter monocotyledon, and dicotyledon) for each year to create a cropland landcover thematic map. The cropland landcover map was used to assign each pixel a class which was used to identify the appropriate LUT for inversion. The USDA CDL landcover layer was determined to be an accurate layer for spatial segmentation of the study area based on observations made in the field between 2015 and 2017.

The study periods were segmented using normalized difference vegetation index (NDVI) calculated from the HLS product and the 50% threshold method (White et al. 1997) adapted from Rojas et al. (2011) to temporally aggregate days of the study period into phenological stages for each crop type. The NDVI (Tucker 1979) was calculated using the HLS surface reflectance values extracted for each overpass and field plot location as:

$$\mathrm{NDVI} = \frac{\rho\mathrm{NIR} - \rho\mathrm{Red}}{\rho\mathrm{NIR} + \rho\mathrm{Red}} \quad (5)$$

where ρNIR is the near-infrared band 5 and 8A for Landsat-8 and Sentinel-2, respectively, and ρRed is the red band 4 for both Landsat-8 and Sentinel-2.

For each plot pixel, the maximum and preceding minimum NDVI values were identified to determine the start-of-season (SOS) and end-of-season (EOS). SOS is the moment when NDVI reached the average between maximum and minimum NDVI for the year. EOS was identified as the moment when NDVI returns to the average between maximum and minimum. The growing season period, defined as the time between SOS and EOS, was subsequently divided into three phenological classes for each crop type using knowledge of the local growing season: early, mid, and late, corresponding to vegetative development, flowering, and yield formation and ripening, respectively. SOS generally coincided with the onset of the early phenological class for all pixels. The mid phenological class was determined using observations made in the field during measurements. The remaining days before EOS were classified as the late phenological class (Figure 2.6).

The plots were aggregated into crop types. An average NDVI threshold was calculated for each crop type using the pixels of each plot. The averaged NDVI thresholds were then applied to all pixels in an image for each crop type. Each pixel was assigned a phenological period depending on the crop type landcover class. This step was repeated for each year.

Strategy 3: Crop and time dependent LUTs with constrained N_s, LAI, and ALA:

The third strategy adopts an integrated LUT generation approach where ancillary information and *a priori* knowledge is used for constraining LAI and ALA. The field boundaries and crop information from the CDL were combined with the MCD15A2H product to generate LAI probability distributions, for each crop and 8-day period. The MCD15A2H product, with the minimum time difference to the HLS overpass used in the inversion, was resampled, using B-spline interpolation, to a 30 m spatial resolution, and was used to extract LAI statistics for each CDL field boundary area within the entire HLS scene (Figure 2.7).

The CDL map was also used to inform the selection of reference ALA values. The SAIL presets for erectophile leaf distribution was used for the inversion of monocotyledon crops, and the uniform leaf distribution was used for pixels classified as dicotyledon.

Multivariate log-gaussian distributions were used for C_w, and C_m based on the data collection presented in the field sampling dataset section (Tables 2.4 and 2.5). The leaf measurements from Boren, et al. [88] were used to further constrain the N_s parameter based on estimated N_s for different crop types and phenological stages; generating different gaussian probability distributions for monocotyledon and dicotyledon plants at various growth stages are listed in Table 2.6. The soil parameter was constrained to the 0.3 to 0.7 range, to reflect realistic canopy closure conditions for the study area.

Spectral pre-processing and LUT inversion

After the LUTs were generated by forward model computation, reflectance spectra were converted to Landsat-8 and Sentinel-2 band reflectance as an integral product of the spectra with each Landsat-8 (Zhang and Roy 2016) and Sentinel-2 (ESA 2015) band spectral response functions. As per the HLS product (Claverie et al. 2018), spectral band pass adjustments were made to the Sentinel-2 bands to reflect the HLS Sentinel product more closely.

Finding the solution for LUT inversion consists of selecting the reflectance realization, the difference of which from measured reflectance is minimal and identifying the corresponding set of input variables. The choice of a cost function is critical when running an inversion problem, since it may dictate the quality of the inversion given the unknown distribution of errors and nonlinearity on the model (Rivera et al. 2013; Verrelst et al. 2014). In accordance with the results of the comparison of cost functions presented in Rivera et al. (2013), the absolute error cost function was used in the present study, defined as:

$$D(P,Q) = \sum_{i=1}^{\lambda_n} |p(\lambda_i) - q(\lambda_i)| \quad (6)$$

where D(P,Q) is the distance between the satellite observed reflectances (P) and LUT reflectances (Q), p(λi) is the satellite observed surface reflectance and q(λi) is the LUT retrieved surface reflectance at wavelength λi, and n is the number of available spectral bands.

For strategies 1 and 2, the inversion was performed by selecting the spectral realization which had the lowest absolute difference compared to the measured spectra across all bands of interest. The inversion of the strategy 3 LUT instead used spectra normalization.

Spectra normalization has shown to improve performances of inverse problem solving by compressing dataset; thereby, increasing the probability of matching observed and simulated spectra (Rivera et al. 2013). This is especially useful in spectral regions where variation is narrow, such as the visible region with C_{cab} (Rivera et al. 2013). To our knowledge, normalization has not been applied to solve LUT inversion problems for retrieving C_w. Lastly, it has been found that the non-linear correlation between parameters can be better handled when applying regularization methods on the individual variables, rather than simultaneously on the combined synthetic variable (Bacour et al. 2006; Dorigo et al. 2007; Rivera et al. 2013). Often, inversions for a combined synthetic variable (i.e., CCWC) are successful, but due to a compensation effect between the individual parameters (i.e., high C_w and low LAI or vice versa), the results are poor for the individual parameters which make up the synthetic canopy parameter.

Since it is better to have balanced successful performance in retrieving all individual parameters in an operational setting (Verrelst et al. 2014), we treated the inversion of each single variable of interest (C_w and *LAI*) separately in the third strategy. The inversion of C_w was also spectrally constrained to the NIR and SWIR bands for both Landsat-8 and Sentinel-2 retrievals. For inversion of LAI, we spectrally constrain the inversion to exclude only the coastal aerosol, water vapor, cirrus bands as mentioned above. Since it was recommended in a previous study that normalization not be applied to solve for LAI due to the broad range of spectral variation (Rivera et al. 2013), normalization was exclusively used for the retrieval of $C_{w.}$

Finally, instead of using the single best solution, the mean of top solutions has improved the robustness of inversion problems in the past (Koetz et al. 2005; Richter et al. 2011). The mean of the top 1% of inversion solutions with the lowest difference from the observation was used as the solution in strategy 3.

Validation

A quantitative comparison between estimated and measured leaf and canopy parameters was completed through linear regression analysis, and calculation of the root-mean-square error (RMSE), mean absolute error (MAE), and the Nash–Sutcliffe efficiency (NSE), Equations (7), (8), and (9):

$$\mathrm{RMSE} = \sqrt{\frac{\sum_{i=1}^{n}(y_i' - y_i)^2}{n}}, \tag{7}$$

$$\mathrm{MAE} = \frac{\sum_{i=1}^{n}|y_i' - y_i|}{n}, \tag{8}$$

$$\mathrm{NSE} = 1 - \frac{\sum_{i=1}^{n}(y_i - y_i')^2}{\sum_{i=1}^{n}(y_i - \bar{y})^2}, \quad (9)$$

where yi and yi' are the measured and estimated CCWC values, respectively, and n the number of measurements.

These measures are commonly used as goodness-of-fit measures for biophysical parameter retrieval (Richter et al. 2012). MAE was used together with RMSE to characterize variation in the errors of predicted parameters, the greater the difference between the measures, the greater the variance in the individual errors. The NSE score ranges between -∞ to 1, where a score of 1 indicates a perfect match between estimated and observed data. An NSE score of 0 corresponds to an outcome where the observed mean is a better predictor than the model (Nash and Sutcliffe 1970).

Results

The HLS LUT inversion strategies were applied to the 8 km by 8 km study area (Figure 2.1) throughout the 2015–2017 growing seasons, using all the HLS images (Table 2.3) that were retained after the QA screening described in the field sampling dataset section. Figure 2.8 illustrates a comparison of inversion strategy results for four dates during the 2016 growing season (May 2, June 1, June 20, and July 15); for each crop type. Table 2.7 presents the phenological stages at these four dates.

Qualitatively, the inversion results are consistent with the typical CCWC patterns observed throughout the growing season: increase in water content during emergence to peak dates in June, to then decrease during senescence and maturation in mid-July. Figure 2.8 also shows that the within-field variability and the salt-and-pepper noise in the maps of estimated CCWC is greatly reduced by the introduction of constraints of biophysical parameters in strategy 3, compared to strategies 1 and 2. This is also evident from Figure 2.9, reporting the boxplots of the estimated CCWC for each inversion strategy and crop-type for the same dates as the images in Figure 2.8, and showing that the spread of the estimated values is greatly reduced by Strategy 3, compared to Strategies 2 and 3.

The estimated CCWC spatial variation and temporal progression are consistent with the retrieved NDWI spectral index derived from the coincident HLS imagery for each of the dates from Figure 2.8 (Figure 2.10).

Figure 2.11 compares the time series of values of CCWC estimated through the three inversion strategies, with the coincident measurements acquired on the five field plots in the 2016 growing season. Overall, CCWC estimated through all three strategies are consistent with the field measurements; however, there is an evident underestimation by strategies 1 and 2 of the peak water content in wheat and barley plots (plots A, B, and C), and a slight overestimation of the peak water

content by strategy 3 in one of the garbanzo plots (plot E). The correlation between measured and estimated CCWC increases progressively with each strategy, as more ancillary information is used: R^2 = 0.73, R^2 = 0.74, and R^2 = 0.81, for strategies 1, 2, and 3, respectively.

The scatterplots of estimated and measured C_w, CCWC, and LAI, obtained using all points acquired in the three years of field data collection campaigns, are presented in Figure 2.12, and the relevant regression metrics (slope, offset, and linear correlation coefficient) and validation metrics described in the validation section are presented in Table 2.8.

In all three strategies, the retrieval of LAI and C_w were considerably less accurate than the retrieval of CCWC. Apart from strategy 2, CCWC estimation using Sentinel-2A imagery, all strategies yielded NSE scores greater than 0.5 for retrieving CCWC. Retrieval of LAI yielded NSE scores less than 0 for all strategies with exception to strategy 3 using Landsat-8 imagery. C_w retrieval was slightly better than LAI retrieval, but unable to yield an NSE score over 0.5 in any of the strategies. The coefficient of determination shows a similar behavior.

Considering CCWC, which is the primary objective of the current study, the best performance for CCWC retrieval was achieved using the Sentinel-2A dataset with strategy 3 constraints, yielding a R^2 of 0.82, NSE score of 0.73, and RMSE of 0.41 x 10^3g m^{-2}. The highest error in CCWC retrieval was observed using Landsat-8 imagery with strategy 2 constraints, yielding a R^2 of 0.71, NSE score of 0.56, and RMSE of 0.59 x 10^3g m^{-2}. In inverting the combined HLS imagery dataset for CCWC retrieval, strategy 3 yielded the best performance (R^2 = 0.76, NSE = 0.71, RMSE = 0. 46 x 10^3g m^{-2}) while strategy 2 had slightly higher errors than strategy 1, but slightly higher coefficient of determination than strategy 1 (R^2 = 0.70, NSE = 0.53, RMSE = 0. 58 x 10^3g m^{-2}).

Finally, a comparison between retrieved CCWC from Landsat-8 and Sentinel-2A imagery indicated better CCWC retrieval using the Sentinel-2A imagery than Landsat-8 in each of the three strategies. The CCWC retrieval using Sentinel-2A imagery was also more negatively impacted by the additional constraint of the N_s parameter, showing an increase in RMSE from strategy 1 to strategy 2 of about 0.11 x 10^3g m^{-2}, compared to the 0.03 x 10^3g m^{-2} increase from strategy 1 to strategy 2 using Landsat-8 imagery.

Discussion

Among the three approaches considered in this study, inversion strategy 3, which constrained the possible values of the PRO4SAIL parameters through the use of *a priori* information and ancillary data, resulted in the best performance in the estimation of CCWC, as reflected by all the validation metrics and by the analysis of the time series of estimated values. A major benefit of the validation

dataset assembled for the present study, and encompassing the full phenological cycle of wheat, barley, and garbanzo crops, is the ability to assess the stability of the inversion throughout the growing season.

These results are in agreement with past studies, showing improved PRO4SAIL inversion results by imposing spatial, temporal, and spectral constraints (Dorigo et al. 2009; Lauvernet et al. 2008; Rivera et al. 2013), and by using optimization techniques (Koetz et al. 2005; Richter et al. 2011; Richter et al. 2009), and normalization (Rivera et al. 2013).

The compensation between C_w and LAI for CCWC retrieval is well known (Verrelst et al. 2014) and evident in the results of this paper, with considerably less accurate retrieval for C_w and LAI than for CCWC across each strategy.

There are a few known issues with PRO4SAIL inversion for estimating canopy biochemical and physical properties that can explain the presence of data points with high errors, evident in the scatterplots of Figure 12, corresponding to observations acquired either at the beginning or at the end of the growing season. It is known that the PRO4SAIL model is more sensitive to small variations in LAI and soil background reflectance during periods of low canopy closure (Bacour et al. 2002a). Anisotropic effects are also critical when considering the sensitivity of PRO4SAIL to LAI, ALA, and soil background; viewing angles close to nadir show the largest sensitivity to ALA and soil background as compared to LAI, while off nadir angles display more sensitivity to LAI (Jacquemoud et al. 2009). Finally, spectral endmembers characterizing typical wet and dry soil signatures were used throughout the entire study period. It has been found in other similar studies that parameter retrieval may be improved in late season periods by replacing the original soil spectral profile with the spectral signature of non-photosynthetic vegetative material (crop residue) (Danner et al. 2017).

To some extent, some of the errors could be attributed to limitations of the adopted model. The canopy system within the 30 m pixel, as modeled by SAIL, is assumed to a homogenous turbid medium and does not account for leaves at various positions within the canopy with different water content, i.e., leaves having higher water content being more distributed near the top of the canopy. Furthermore, multiple-scattering effects within the canopy were not taken into account, potentially resulting in an overestimation of water content in some cases.

The intrinsic limitations of the HLS dataset should also be considered. The spectral resolution of the OLI and MSI instruments is not optimal for canopy water retrieval, as both instruments lack specific liquid water absorption bands at 970 nm and 1200 nm. Future missions with improved spectral capabilities may have better performance in CCWC retrieval under the same inversion techniques. The HLS reflectances are atmospherically corrected and normalized for BRDF, but no topographic

correction is currently performed, and slope effects could potentially translate into errors in the RTM inversion. Because all the validation data were acquired on relatively flat portions of the study area, we could not assess the occurrence of such errors. Further evaluation of the HLS atmospheric correction would be also needed, to assess whether there is any residual effect due to the atmospheric water vapor absorption, which would impact the precision of the canopy water retrieval.

It is worth noticing that use of the MCD15A2H product to define *a priori* probability distribution in for LAI in Strategy 3 resulted only in a very modest improvement in LAI retrieval accuracy compared to the other strategies (e.g., using both Landsat-8 and Sentinel-2 data, RMSE = 1.87 m^2 m^{-2} and R^2 = 0.25 in Strategy 1, RMSE = 1.69 m^2 m^{-2} and R^2 = 0.22 in Strategy 2, RMSE = 1.43 m^2 m^{-2} and R^2 = 0.33 in Strategy 3). Arguably, this is due to the coarse spatial resolution of the MODIS product relative to the field size in the study area (evident in Figure 2.7), which resulted in inaccurate *a priori* values for a large proportion of the image. The availability of higher resolution LAI products would likely result in a large improvement of the retrievals.

Future research is required to investigate the characterization of ALA, as it is one of the most important canopy structure parameters affecting canopy radiation scattering and least studied in PRO4SAIL research (Berger et al. 2018).

The comparison of the results of Strategy 1 and 2 shows that constraining the N_s parameter was not sufficient to significantly improve the accuracy of the retrievals; strategy 2 resulted in slightly better estimation of LAI and slightly worse estimation of C_w and CCWC. The inversion results hence imply that N_s does not impact the output of PRO4SAIL as much as canopy structural parameters like LAI or ALA, as indicated from previous theoretical studies (Jacquemoud et al. 2009). The slight increase in accuracy in LAI estimation when constraining N_s may warrant further investigation in future studies which explore the sensitivity of N_s to LAI, with an emphasis on the need to collecting a more exhaustive field dataset during periods of increasing LAI, i.e., at the beginning of the growing season. Finally, the inversion of C_w did not substantially improve with the added ancillary information of strategy 3.

Conclusion

In this paper, we developed and demonstrated a new methodology for the retrieval of cropland canopy water content (CCWC) through inversion of the PRO4SAIL radiative transfer model (RTM), constraining the possible values of the model parameters by using *a priori* information derived from lab measurements, previously published literature, and operational remotely sensed products. The validation data from field measurements were taken throughout the growing season for wheat, barley, and garbanzo fields over three growing seasons and capture a complete representation of biophysical

characteristics over each phenological growth stage. The method was demonstrated by inverting reflectances from the Harmonized Landsat Sentinel (HLS) Landsat-8 and Sentinel-2A product, resulting in the first HLS-based CCWC product generated through radiative transfer model inversion.

The results were validated with field measurements collected over three growing seasons. Comparison with unconstrained PRO4SAIL inversions, demonstrate that the proposed method is effective in reducing the uncertainty of the estimates.

The results also illustrated that crop type and phenology may play a significant role in which parameters are more sensitive for PRO4SAIL top-of-canopy reflectance modeling. Retrievals on early and late stage crops had larger errors, due to known issues in PRO4SAIL inversion at low LAI values when the soil is partially exposed.

Combining Landsat-8 and Sentinel-2 sensors in a seamless and regridded form, the HLS product affords the opportunity for cropland monitoring with sufficient temporal and spatial resolution to meet the requirements of operational users. The slope close to unity, low intercept and high coefficient of determination (0.78, 0.07, and 0.76, respectively) of the regression between the estimated CCWC and the field validation dataset clearly indicate the potential of the proposed approach; while the present prototype was developed on a limited study area, the methods proposed are general ones, and could potentially path-find the systematic generation of regional to continental HLS-based CCWC products. Future work will investigate the scalability of the proposed approach, with a priority on testing the prototype on different agricultural regions.

Acknowledgements

This project was supported by the NASA Idaho Space Grant Consortium Fellowship and by the College of Natural Resources of the University of Idaho Doctoral Finishing Fellowship. We would like to acknowledge the growers at Zenner Family Farms, Genesee, ID.

References

Allen, W.A., Gausman, H.W., Richardson, A.J., & Thomas, J.R. (1969). Interaction of isotropic light with a compact plant leaf. JOSA, 59, 1376-1379

Anderson, M., Kustas, W., Norman, J., Hain, C., Mecikalski, J., Schultz, L., González-Dugo, M., Cammalleri, C., d'Urso, G., & Pimstein, A. (2010). Mapping daily evapotranspiration at field to global scales using geostationary and polar orbiting satellite imagery. Hydrology and Earth System Sciences Discussions, 7, 5957-5990

Asner, G.P., Martin, R.E., Knapp, D.E., Tupayachi, R., Anderson, C., Carranza, L., Martinez, P., Houcheime, M., Sinca, F., & Weiss, P. (2011). Spectroscopy of canopy chemicals in humid tropical forests. Remote sensing of environment, 115, 3587-3598

Atzberger, C. (2013). Advances in remote sensing of agriculture: Context description, existing operational monitoring systems and major information needs. Remote Sensing, 5, 949-981

Bacour, C., Baret, F., Béal, D., Weiss, M., & Pavageau, K. (2006). Neural network estimation of LAI, fAPAR, fCover and LAI× C ab, from top of canopy MERIS reflectance data: principles and validation. Remote sensing of environment, 105, 313-325

Bacour, C., Baret, F., & Jacquemoud, S. (2002a). Information content of HyMap hyperspectral imagery. In, Proceedings of the 1st International Symposium on Recent Advances in Quantitative Remote Sensing, Valencia (Spain), 16 (pp. 503-508)

Bacour, C., Jacquemoud, S., Leroy, M., Hautecœur, O., Weiss, M., Prévot, L., Bruguier, N., & Chauki, H. (2002b). Reliability of the estimation of vegetation characteristics by inversion of three canopy reflectance models on airborne POLDER data. Agronomie-Sciences des Productions Vegetales et de l'Environnement, 22, 555-566

Bailey, R. (1995). Description of the Ecoregions of the United States, 2nd. Edition. Rev. and Expanded. Misc. Publ

Bandyopadhyay, K., Pradhan, S., Sahoo, R., Singh, R., Gupta, V., Joshi, D., & Sutradhar, A. (2014). Characterization of water stress and prediction of yield of wheat using spectral indices under varied water and nitrogen management practices. Agricultural water management, 146, 115-123

Baret, F. (2016). VAlidation of Land European Remote sensing Instruments. In

Baret, F., & Buis, S. (2008). Estimating canopy characteristics from remote sensing observations: Review of methods and associated problems. Advances in land remote Sensing (pp. 173-201): Springer

Baret, F., & Guyot, G. (1991). Potentials and limits of vegetation indices for LAI and APAR assessment. Remote sensing of environment, 35, 161-173

Baret, F., Houles, V., & Guérif, M. (2007). Quantification of plant stress using remote sensing observations and crop models: the case of nitrogen management. Journal of Experimental Botany, 58, 869-880

Baret, F., Jacquemoud, S., Guyot, G., & Leprieur, C. (1992). Modeled analysis of the biophysical nature of spectral shifts and comparison with information content of broad bands. Remote sensing of environment, 41, 133-142

Becker-Reshef, I., Justice, C., Sullivan, M., Vermote, E., Tucker, C., Anyamba, A., Small, J., Pak, E., Masuoka, E., & Schmaltz, J. (2010). Monitoring global croplands with coarse resolution earth observations: The Global Agriculture Monitoring (GLAM) project. Remote Sensing, 2, 1589-1609

Belward, A., Bourassa, M., Dowell, M., Briggs, S., Dolman, H., & Holmlund, K. (2016). The global observing system for climate: Implementation needs. Report to World Meteorological Organization

Berger, K., Atzberger, C., Danner, M., D'Urso, G., Mauser, W., Vuolo, F., & Hank, T. (2018). Evaluation of the PROSAIL model capabilities for future hyperspectral model environments: a review study. Remote Sensing, 10, 85

Boren, E.J., Boschetti, L., & Johnson, D.M. (2019). Characterizing the Variability of the Structure Parameter in the PROSPECT Leaf Optical Properties Model. Remote Sensing, 11, 1236

Boryan, C., Yang, Z., Mueller, R., & Craig, M. (2011). Monitoring US agriculture: the US department of agriculture, national agricultural statistics service, cropland data layer program. Geocarto International, 26, 341-358

Campbell, G. (1990). Derivation of an angle density function for canopies with ellipsoidal leaf angle distributions. Agricultural and Forest Meteorology, 49, 173-176

Carlson, T.N., Gillies, R.R., & Perry, E.M. (1994). A method to make use of thermal infrared temperature and NDVI measurements to infer surface soil water content and fractional vegetation cover. Remote Sensing Reviews, 9, 161-173

Ceccato, P., Flasse, S., Tarantola, S., Jacquemoud, S., & Grégoire, J.-M. (2001). Detecting vegetation leaf water content using reflectance in the optical domain. Remote sensing of environment, 77, 22-33

Cheng, Y.-B., Ustin, S.L., Riaño, D., & Vanderbilt, V.C. (2008). Water content estimation from hyperspectral images and MODIS indexes in Southeastern Arizona. Remote sensing of environment, 112, 363-374

Claps, P., & Laguardia, G. (2004). Assessing spatial variability of soil water content through Thermal Inertia and NDVI. In, Remote Sensing for Agriculture, Ecosystems, and Hydrology V (pp. 378-388): International Society for Optics and Photonics

Claverie, M., Ju, J., Masek, J.G., Dungan, J.L., Vermote, E.F., Roger, J.-C., Skakun, S.V., & Justice, C. (2018). The Harmonized Landsat and Sentinel-2 surface reflectance data set. Remote sensing of environment, 219, 145-161

Claverie, M., Masek, J.G., & Ju, J. (2016). Harmonized Landsat-8 Sentinel-2 (HLS) Product User's Guide. In

Colombo, R., Meroni, M., Marchesi, A., Busetto, L., Rossini, M., Giardino, C., & Panigada, C. (2008). Estimation of leaf and canopy water content in poplar plantations by means of hyperspectral indices and inverse modeling. Remote sensing of environment, 112, 1820-1834

Combal, B., Baret, F., & Weiss, M. (2002). Improving canopy variables estimation from remote sensing data by exploiting ancillary information. Case study on sugar beet canopies. Agronomie, 22, 205-215

Combal, B., Baret, F., Weiss, M., Trubuil, A., Mace, D., Pragnere, A., Myneni, R., Knyazikhin, Y., & Wang, L. (2003). Retrieval of canopy biophysical variables from bidirectional reflectance: Using prior information to solve the ill-posed inverse problem. Remote sensing of environment, 84, 1-15

Cosh, M.H., Tao, J., Jackson, T.J., McKee, L., & O'Neill, P.E. (2010). Vegetation water content mapping in a diverse agricultural landscape: National Airborne Field Experiment 2006. Journal of Applied Remote Sensing, 4, 043532

Cox, D., Bezdicek, D., & Fauci, M. (2001). Effects of compost, coal ash, and straw amendments on restoring the quality of eroded Palouse soil. Biology and fertility of soils, 33, 365-372

Danner, M., Berger, K., Wocher, M., Mauser, W., & Hank, T. (2017). Retrieval of biophysical crop variables from multi-angular canopy spectroscopy. Remote Sensing, 9, 726

Darvishzadeh, R., Skidmore, A., Atzberger, C., & van Wieren, S. (2008a). Estimation of vegetation LAI from hyperspectral reflectance data: Effects of soil type and plant architecture. International Journal of Applied Earth Observation and Geoinformation, 10, 358-373

Darvishzadeh, R., Skidmore, A., Schlerf, M., & Atzberger, C. (2008b). Inversion of a radiative transfer model for estimating vegetation LAI and chlorophyll in a heterogeneous grassland. Remote sensing of environment, 112, 2592-2604

Djamai, N., Fernandes, R., Weiss, M., McNairn, H., & Goïta, K. (2019). Validation of the Sentinel Simplified Level 2 Product Prototype Processor (SL2P) for mapping cropland biophysical variables using Sentinel-2/MSI and Landsat-8/OLI data. Remote sensing of environment, 225, 416-430

Dorigo, W., Richter, R., Baret, F., Bamler, R., & Wagner, W. (2009). Enhanced automated canopy characterization from hyperspectral data by a novel two step radiative transfer model inversion approach. Remote Sensing, 1, 1139-1170

Dorigo, W.A., Zurita-Milla, R., de Wit, A.J., Brazile, J., Singh, R., & Schaepman, M.E. (2007). A review on reflective remote sensing and data assimilation techniques for enhanced agroecosystem modeling. International Journal of Applied Earth Observation and Geoinformation, 9, 165-193

Duan, S.-B., Li, Z.-L., Wu, H., Tang, B.-H., Ma, L., Zhao, E., & Li, C. (2014). Inversion of the PROSAIL model to estimate leaf area index of maize, potato, and sunflower fields from unmanned aerial vehicle hyperspectral data. International Journal of Applied Earth Observation and Geoinformation, 26, 12-20

Entekhabi, D., Njoku, E.G., O'Neill, P.E., Kellogg, K.H., Crow, W.T., Edelstein, W.N., Entin, J.K., Goodman, S.D., Jackson, T.J., & Johnson, J. (2010). The soil moisture active passive (SMAP) mission. Proceedings of the IEEE, 98, 704-716

ESA (2015). Sentinel-2A Spectral Response Functions (S2A-SRF) COPE-GSEG-EOPG-TN-15-0007. In E.E.S. Agency) (Ed.)

Féret, J.-B., François, C., Asner, G.P., Gitelson, A.A., Martin, R.E., Bidel, L.P., Ustin, S.L., Le Maire, G., & Jacquemoud, S. (2008). PROSPECT-4 and 5: Advances in the leaf optical properties model separating photosynthetic pigments. Remote sensing of environment, 112, 3030-3043

Féret, J.-B., François, C., Gitelson, A., Asner, G.P., Barry, K.M., Panigada, C., Richardson, A.D., & Jacquemoud, S. (2011). Optimizing spectral indices and chemometric analysis of leaf chemical properties using radiative transfer modeling. Remote sensing of environment, 115, 2742-2750

Féret, J.-B., Gitelson, A., Noble, S., & Jacquemoud, S. (2017). PROSPECT-D: Towards modeling leaf optical properties through a complete lifecycle. Remote sensing of environment, 193, 204-215

Fladung, M., & Ritter, E. (1991). Plant Leaf Area Measurements by Personal Computers. Journal of Agronomy and Crop Science, 166, 69-70

François, C., Ottlé, C., Olioso, A., Prévot, L., Bruguier, N., & Ducros, Y. (2002). Conversion of 400-1100 nm vegetation albedo measurements into total shortwave broadband albedo using a canopy radiative transfer model. Agronomie, 22, 611-618

Francone, C., Pagani, V., Foi, M., Cappelli, G., & Confalonieri, R. (2014). Comparison of leaf area index estimates by ceptometer and PocketLAI smart app in canopies with different structures. Field Crops Research, 155, 38-41

Fritz, S., See, L., Bayas, J.C.L., Waldner, F., Jacques, D., Becker-Reshef, I., Whitcraft, A., Baruth, B., Bonifacio, R., & Crutchfield, J. (2019). A comparison of global agricultural monitoring systems and current gaps. Agricultural Systems, 168, 258-272

Fritz, S., See, L., McCallum, I., You, L., Bun, A., Moltchanova, E., Duerauer, M., Albrecht, F., Schill, C., & Perger, C. (2015). Mapping global cropland and field size. Global Change Biology, 21, 1980-1992

Gao, B.-C. (1996). NDWI—A normalized difference water index for remote sensing of vegetation liquid water from space. Remote sensing of environment, 58, 257-266

Grafton, R., Williams, J., Perry, C., Molle, F., Ringler, C., Steduto, P., Udall, B., Wheeler, S., Wang, Y., & Garrick, D. (2018). The paradox of irrigation efficiency. Science, 361, 748-750

Grossman, Y., Ustin, S., Jacquemoud, S., Sanderson, E., Schmuck, G., & Verdebout, J. (1996). Critique of stepwise multiple linear regression for the extraction of leaf biochemistry information from leaf reflectance data. Remote sensing of environment, 56, 182-193

Han, W., Yang, Z., Di, L., & Mueller, R. (2012). CropScape: A Web service based application for exploring and disseminating US conterminous geospatial cropland data products for decision support. Computers and electronics in agriculture, 84, 111-123

Hazaymeh, K., & Hassan, Q.K. (2016). Remote sensing of agricultural drought monitoring: A state of art review

Houborg, R., Soegaard, H., & Boegh, E. (2007). Combining vegetation index and model inversion methods for the extraction of key vegetation biophysical parameters using Terra and Aqua MODIS reflectance data. Remote sensing of environment, 106, 39-58

Hu, G., Wang, Y., & Cui, W. (2008). Drought monitoring based on remotely sensed data in the key growing period of winter wheat: A case study in Hebei province, China. Int Arch Photogramm Remote Sens Spat Inf Sci Beijing, 37, 403-408

Jackson, T.J., Schmugge, T.J., & Wang, J.R. (1982). Passive microwave sensing of soil moisture under vegetation canopies. Water Resources Research, 18, 1137-1142

Jacquemoud, S., Bacour, C., Poilve, H., & Frangi, J.-P. (2000). Comparison of four radiative transfer models to simulate plant canopies reflectance: Direct and inverse mode. Remote sensing of environment, 74, 471-481

Jacquemoud, S., & Baret, F. (1990). PROSPECT: A model of leaf optical properties spectra. Remote sensing of environment, 34, 75-91

Jacquemoud, S., Baret, F., Andrieu, B., Danson, F., & Jaggard, K. (1995). Extraction of vegetation biophysical parameters by inversion of the PROSPECT+ SAIL models on sugar beet canopy reflectance data. Application to TM and AVIRIS sensors. Remote sensing of environment, 52, 163-172

Jacquemoud, S., Ustin, S., Verdebout, J., Schmuck, G., Andreoli, G., & Hosgood, B. (1996). Estimating leaf biochemistry using the PROSPECT leaf optical properties model. Remote sensing of environment, 56, 194-202

Jacquemoud, S., Verhoef, W., Baret, F., Bacour, C., Zarco-Tejada, P.J., Asner, G.P., François, C., & Ustin, S.L. (2009). PROSPECT+ SAIL models: A review of use for vegetation characterization. Remote sensing of environment, 113, S56-S66

Jay, S., Maupas, F., Bendoula, R., & Gorretta, N. (2017). Retrieving LAI, chlorophyll and nitrogen contents in sugar beet crops from multi-angular optical remote sensing: Comparison of

vegetation indices and PROSAIL inversion for field phenotyping. Field Crops Research, 210, 33-46

Knyazikhin, Y., Martonchik, J., Myneni, R.B., Diner, D., & Running, S.W. (1998). Synergistic algorithm for estimating vegetation canopy leaf area index and fraction of absorbed photosynthetically active radiation from MODIS and MISR data. Journal of Geophysical Research: Atmospheres, 103, 32257-32275

Koetz, B., Baret, F., Poilvé, H., & Hill, J. (2005). Use of coupled canopy structure dynamic and radiative transfer models to estimate biophysical canopy characteristics. Remote sensing of environment, 95, 115-124

Koetz, B., Kneubuehler, M., Huber, S., Schopfer, J., & Baret, F. (2007). LAI estimation based on multi-temporal CHRIS/PROBA data and radiative transfer modeling. In, Proc. Envisat Symposium 2007 (pp. 1-6)

Kumar, S., Peters-Lidard, C., Santanello, J., Reichle, R., Draper, C., Koster, R., Nearing, G., & Jasinski, M. (2015). Evaluating the utility of satellite soil moisture retrievals over irrigated areas and the ability of land data assimilation methods to correct for unmodeled processes. Hydrology and Earth System Sciences, 19, 4463

Kumar, S.V., Jasinski, M., Mocko, D., Rodell, M., Borak, J., Li, B., Kato Beaudoing, H., & Peters-Lidard, C.D. (2018). NCA-LDAS land analysis: Development and performance of a multisensor, multivariate land data assimilation system for the National Climate Assessment. Journal of Hydrometeorology

Kuusk, A. (1995). A fast, invertible canopy reflectance model. Remote sensing of environment, 51, 342-350

Laurent, V.C., Verhoef, W., Damm, A., Schaepman, M.E., & Clevers, J.G. (2013). A Bayesian object-based approach for estimating vegetation biophysical and biochemical variables from APEX at-sensor radiance data. Remote sensing of environment, 139, 6-17

Lauvernet, C., Baret, F., Hascoët, L., Buis, S., & Le Dimet, F.-X. (2008). Multitemporal-patch ensemble inversion of coupled surface–atmosphere radiative transfer models for land surface characterization. Remote sensing of environment, 112, 851-861

Le Maire, G., Francois, C., & Dufrene, E. (2004). Towards universal broad leaf chlorophyll indices using PROSPECT simulated database and hyperspectral reflectance measurements. Remote sensing of environment, 89, 1-28

Li, J., & Roy, D.P. (2017). A global analysis of Sentinel-2A, Sentinel-2B and Landsat-8 data revisit intervals and implications for terrestrial monitoring. Remote Sensing, 9, 902

Li, P., & Wang, Q. (2011). Retrieval of leaf biochemical parameters using PROSPECT inversion: A new approach for alleviating ill-posed problems. IEEE Transactions on Geoscience and Remote Sensing, 49, 2499-2506

Li, Z., Roy, D., & Zhang, H. (2017). There is no bidirectional hot-spot in Sentinel-2 data. In, AGU Fall Meeting Abstracts

Liu, J., Pattey, E., Nolin, M.C., Miller, J.R., & Ka, O. (2008). Mapping within-field soil drainage using remote sensing, DEM and apparent soil electrical conductivity. Geoderma, 143, 261-272

Martin, M.E., Plourde, L., Ollinger, S., Smith, M.-L., & McNeil, B. (2008). A generalizable method for remote sensing of canopy nitrogen across a wide range of forest ecosystems. Remote sensing of environment, 112, 3511-3519

Meesters, A.G., De Jeu, R.A., & Owe, M. (2005). Analytical derivation of the vegetation optical depth from the microwave polarization difference index. IEEE Geoscience and Remote Sensing Letters, 2, 121-123

Myneni, R., Knyazikhin, Y., & Park, T. (2015). MCD15A2H MODIS/Terra+ Aqua leaf area index/FPAR 8-day L4 Global 500 m SIN Grid V006. NASA EOSDIS Land Processes DAAC. Available online: https://lpdaac. usgs. gov/dataset_discovery/modis/modis_products_table/mcd15a2h_v006 (accessed on 16 October 2016)

Nash, J.E., & Sutcliffe, J.V. (1970). River flow forecasting through conceptual models part I—A discussion of principles. Journal of hydrology, 10, 282-290

Ollinger, S. (2011). Sources of variability in canopy reflectance and the convergent properties of plants. New Phytologist, 189, 375-394

Papendick, R. (1996). Farming systems and conservation needs in the northwest wheat region. American Journal of Alternative Agriculture, 11, 52-57

Peñuelas, J., Filella, I., Biel, C., Serrano, L., & Save, R. (1993). The reflectance at the 950–970 nm region as an indicator of plant water status. International Journal of Remote Sensing, 14, 1887-1905

Peñuelas, J., Gamon, J., Fredeen, A., Merino, J., & Field, C. (1994). Reflectance indices associated with physiological changes in nitrogen-and water-limited sunflower leaves. Remote sensing of environment, 48, 135-146

Peters, J., De Baets, B., De Clercq, E.M., Ducheyne, E., & Verhoest, N.E. (2011). The potential of multitemporal Aqua and Terra MODIS apparent thermal inertia as a soil moisture indicator. International Journal of Applied Earth Observation and Geoinformation, 13, 934-941

Quan, X., He, B., & Li, X. (2015). A Bayesian network-based method to alleviate the ill-posed inverse problem: A case study on leaf area index and canopy water content retrieval. IEEE Transactions on Geoscience and Remote Sensing, 53, 6507-6517

Richter, K., Atzberger, C., Hank, T.B., & Mauser, W. (2012). Derivation of biophysical variables from Earth observation data: validation and statistical measures. Journal of Applied Remote Sensing, 6, 063557-063551-063557-063523

Richter, K., Atzberger, C., Vuolo, F., & D'Urso, G. (2011). Evaluation of sentinel-2 spectral sampling for radiative transfer model based LAI estimation of wheat, sugar beet, and maize. IEEE Journal of selected topics in applied earth observations and remote sensing, 4, 458-464

Richter, K., Atzberger, C., Vuolo, F., Weihs, P., & d'Urso, G. (2009). Experimental assessment of the Sentinel-2 band setting for RTM-based LAI retrieval of sugar beet and maize. Canadian Journal of Remote Sensing, 35, 230-247

Rivera, J.P., Verrelst, J., Leonenko, G., & Moreno, J. (2013). Multiple cost functions and regularization options for improved retrieval of leaf chlorophyll content and LAI through inversion of the PROSAIL model. Remote Sensing, 5, 3280-3304

Rojas, O., Vrieling, A., & Rembold, F. (2011). Assessing drought probability for agricultural areas in Africa with coarse resolution remote sensing imagery. Remote sensing of environment, 115, 343-352

Roy, D.P., Zhang, H., Ju, J., Gomez-Dans, J.L., Lewis, P.E., Schaaf, C., Sun, Q., Li, J., Huang, H., & Kovalskyy, V. (2016). A general method to normalize Landsat reflectance data to nadir BRDF adjusted reflectance. Remote sensing of environment, 176, 255-271

Rud, R., Cohen, Y., Alchanatis, V., Levi, A., Brikman, R., Shenderey, C., Heuer, B., Markovitch, T., Dar, Z., & Rosen, C. (2014). Crop water stress index derived from multi-year ground and aerial thermal images as an indicator of potato water status. Precision agriculture, 15, 273-289

Si, Y., Schlerf, M., Zurita-Milla, R., Skidmore, A., & Wang, T. (2012). Mapping spatio-temporal variation of grassland quantity and quality using MERIS data and the PROSAIL model. Remote sensing of environment, 121, 415-425

Tucker, C.J. (1979). Red and photographic infrared linear combinations for monitoring vegetation. Remote sensing of environment, 8, 127-150

Ullah, S., Skidmore, A.K., Ramoelo, A., Groen, T.A., Naeem, M., & Ali, A. (2014). Retrieval of leaf water content spanning the visible to thermal infrared spectra. ISPRS Journal of Photogrammetry and Remote Sensing, 93, 56-64

Ustin, S.L., Darling, D., Kefauver, S., Greenberg, J., Cheng, Y.-B., & Whiting, M.L. (2004). Remotely sensed estimates of crop water demand. In, Remote Sensing and Modeling of Ecosystems for Sustainability (pp. 230-241). Denver, CO: International Society for Optics and Photonics

van Emmerik, T., Steele-Dunne, S.C., Judge, J., & van de Giesen, N. (2015). Impact of diurnal variation in vegetation water content on radar backscatter from maize during water stress. IEEE Transactions on Geoscience and Remote Sensing, 53, 3855-3869

Verger, A., Baret, F., & Camacho, F. (2011). Optimal modalities for radiative transfer-neural network estimation of canopy biophysical characteristics: Evaluation over an agricultural area with CHRIS/PROBA observations. Remote sensing of environment, 115, 415-426

Verhoef, W. (1984). Light scattering by leaf layers with application to canopy reflectance modeling: the SAIL model. Remote sensing of environment, 16, 125-141

Verhoef, W., Jia, L., Xiao, Q., & Su, Z. (2007). Unified optical-thermal four-stream radiative transfer theory for homogeneous vegetation canopies. IEEE Transactions on Geoscience and Remote Sensing, 45, 1808-1822

Verrelst, J., Rivera, J.P., Leonenko, G., Alonso, L., & Moreno, J. (2014). Optimizing LUT-based RTM inversion for semiautomatic mapping of crop biophysical parameters from Sentinel-2 and-3 data: Role of cost functions. IEEE Transactions on Geoscience and Remote Sensing, 52, 257-269

Verrelst, J., Romijn, E., & Kooistra, L. (2012). Mapping vegetation density in a heterogeneous river floodplain ecosystem using pointable CHRIS/PROBA data. Remote Sensing, 4, 2866-2889

Verstraeten, W.W., Veroustraete, F., van der Sande, C.J., Grootaers, I., & Feyen, J. (2006). Soil moisture retrieval using thermal inertia, determined with visible and thermal spaceborne data, validated for European forests. Remote sensing of environment, 101, 299-314

Weiss, M., Baret, F., Myneni, R., Pragnère, A., & Knyazikhin, Y. (2000). Investigation of a model inversion technique to estimate canopy biophysical variables from spectral and directional reflectance data. Agronomie, 20, 3-22

Whitcraft, A.K., Becker-Reshef, I., & Justice, C.O. (2015a). A framework for defining spatially explicit earth observation requirements for a global agricultural monitoring initiative (GEOGLAM). Remote Sensing, 7, 1461-1481

Whitcraft, A.K., Becker-Reshef, I., Killough, B.D., & Justice, C.O. (2015b). Meeting earth observation requirements for global agricultural monitoring: An evaluation of the revisit capabilities of current and planned moderate resolution optical earth observing missions. Remote Sensing, 7, 1482-1503

White, M.A., Thornton, P.E., & Running, S.W. (1997). A continental phenology model for monitoring vegetation responses to interannual climatic variability. Global biogeochemical cycles, 11, 217-234

Yang, Y., & Ling, P. (2004). Improved model inversion procedure for plant water status assessment under artificial lighting using PROSPECT+ SAIL. Transactions of the ASAE, 47, 1833

Yebra, M., & Chuvieco, E. (2009). Linking ecological information and radiative transfer models to estimate fuel moisture content in the Mediterranean region of Spain: Solving the ill-posed inverse problem. Remote sensing of environment, 113, 2403-2411

Yebra, M., Dennison, P.E., Chuvieco, E., Riaño, D., Zylstra, P., Hunt, E.R., Danson, F.M., Qi, Y., & Jurdao, S. (2013). A global review of remote sensing of live fuel moisture content for fire danger assessment: Moving towards operational products. Remote sensing of environment, 136, 455-468

Yi, Q., Wang, F., Bao, A., & Jiapaer, G. (2014). Leaf and canopy water content estimation in cotton using hyperspectral indices and radiative transfer models. International Journal of Applied Earth Observation and Geoinformation, 33, 67-75

Zarco-Tejada, P.J., Rueda, C., & Ustin, S. (2003). Water content estimation in vegetation with MODIS reflectance data and model inversion methods. Remote sensing of environment, 85, 109-124

Zargar, A., Sadiq, R., Naser, B., & Khan, F.I. (2011). A review of drought indices. Environmental Reviews, 19, 333-349

Zhang, A., & Jia, G. (2013). Monitoring meteorological drought in semiarid regions using multi-sensor microwave remote sensing data. Remote sensing of environment, 134, 12-23

Zhang, C., Pattey, E., Liu, J., Cai, H., Shang, J., & Dong, T. (2017). Retrieving Leaf and Canopy Water Content of Winter Wheat Using Vegetation Water Indices. IEEE Journal of selected topics in applied earth observations and remote sensing

Zhang, H.K., & Roy, D.P. (2016). Computationally inexpensive Landsat 8 operational land imager (OLI) pansharpening. Remote Sensing, 8, 180

Zhang, H.K., Roy, D.P., & Kovalskyy, V. (2016). Optimal solar geometry definition for global long-term Landsat time-series bidirectional reflectance normalization. IEEE Transactions on Geoscience and Remote Sensing, 54, 1410-1418

Zhang, N., Hong, Y., Qin, Q., & Liu, L. (2013). VSDI: a visible and shortwave infrared drought index for monitoring soil and vegetation moisture based on optical remote sensing. International Journal of Remote Sensing, 34, 4585-4609

Table 2.1. Harmonized Landsat Sentinel (HLS) product spectral bands. Table was adapted from Claverie et al. (2016).

Band name	OLI Band Number	MSI Band Number	Wavelength (µm)
Coastal Aerosol	1	1	0.43–0.45
Blue	2	2	0.45–0.51
Green	3	3	0.53–0.59
Red	4	4	0.64–0.67
Red-Edge1	-	5	0.69–0.71
Red-Edge 2	-	6	0.73–0.75
Red-Edge 3	-	7	0.77–0.79
NIR Narrow	5	8A	0.85–0.88
NIR Broad	-	8	0.78–0.88
SWIR 1	6	11	1.57–1.65
SWIR 2	7	12	2.11–2.29
Water vapor	-	9	0.93–0.95
Cirrus	9	10	1.36–1.38
Thermal Infrared 1	10	-	10.60–11.19
QA			

Table 2.2. Summary table of field sampling plots for each year.

Year	Plot	Crop	Number of Field Measurements
2015	A	Barley	4
	B	Barley	3
	C	Barley	4
	D	Barley	4
	E	Garbanzo	3
2016	A	Winter Wheat	13
	B	Winter Wheat	12
	C	Barley	8
	D	Garbanzo	11
	E	Garbanzo	11
2017	A	Barley	5
	B	Winter Wheat	6
	C	Winter Wheat	6
	D	Garbanzo	6
	E	Garbanzo	6

Table 2.3. Summary table of field sampling plots for each year, crop type, and sensor overpass.

	Total	Dicot	Mono. Winter	Mono. Spring	L8 observations	S2 observations	L8	S2
2015	**18**	3	0	15	18	0	5	0
2016	**55**	22	25	8	33	22	12	7
2017	**29**	12	12	5	15	14	3	4
Total	**102**	**37**	**37**	**28**	**66**	**36**	**20**	**11**

Table 2.4. Parameterization of the PRO4SAIL radiative transfer model. The distributions used during LUT generation for each parameter are listed along with fixed values. The asterisk indicates that water thickness and dry matter content log-gaussian distributions in Strategy 3 were generated using a covariance matrix to simulate the correlation between water thickness and dry matter content. The covariances are presented in Table 2.5.

			Strategy 1	**Strategy 2**	**Strategy 3**
Model Parameters	**Symbol**	**Units**	**Parameter values**		
Leaf Parameters PROSPECT-5					
Leaf chlorophyll content	C_{cab}	$\mu g\ cm^{-2}$	Gaussian μ = 32.81, σ = 18.87	Gaussian μ = 32.81, σ = 18.87	Gaussian μ = 32.81, σ = 18.87
Leaf carotenoid content	C_{car}	$\mu g\ cm^{-2}$	Gaussian μ = 8.51, σ = 3.92	Gaussian μ = 8.51, σ = 3.92	Gaussian μ = 8.51, σ = 3.92
Water thickness	C_w	$g\ cm^{-2}$	Gaussian μ = 0.027, σ = 0.018	Gaussian μ = 0.027, σ = 0.018	Log-Gaussian* μ = 0.027, σ = 0.018
Dry matter content	C_m	$g\ cm^{-2}$	Gaussian μ = 0.013, σ = 0.01	Gaussian μ = 0.013, σ = 0.01	Log-Gaussian* μ = 0.013, σ = 0.01
Leaf structure index	N_s	-	Uniform: 1.0–4.0	Uniform: plant type and phenological stage dependent (Table 6)	Gaussian: plant type and phenological stage dependent (Table 6)
Canopy variables 4SAIL					
Leaf area index	LAI	$m^2\ m^{-2}$	Uniform: 0.0–8.0	Uniform: 0.0–8.0	Gaussian: plant type and date dependent
Average leaf angle	ALA	degree	Uniform: 30–70	Uniform: 30–70	Plant type dependent: Erectophile and Uniform
Soil coefficient	$\alpha soil$	unitless	Uniform: 0–1	Uniform: 0–1	Uniform: 0.3 – 0.7

Table 2.5. Covariance matrix of C_w and C_m parameters used for LUT generation in strategy 3.

	C_w	C_m
C_w	3.2×10^{-4}	1.5×10^{-4}
C_m	1.5×10^{-4}	1.0×10^{-4}

Table 2.6. Parameterization of the N_s parameter in PRO4SAIL. Values in the strategy 2 column were used as the minimum and maximum range bounds for generating uniform N_s values while the values in strategy 3 were used as the mean and standard deviation values for generating gaussian N_s values. Values based on Table 2.2 results in Boren et al. (2019).

	Strategy 2		**Strategy 3**	
Phenological stage	**Monocotyledon**	**Dicotyledon**	**Monocotyledon**	**Dicotyledon**
Early	1.0–1.5	2.0–2.5	$\mu = 1.35, \sigma = 0.28$	$\mu = 2.15, \sigma = 0.27$
Mid	1.5–2.0	2.0–2.5	$\mu = 1.5, \sigma = 0.23$	$\mu = 1.96, \sigma = 0.25$
Late	1.5–2.0	2.0–2.5	$\mu = 1.66, \sigma = 0.25$	$\mu = 2.15, \sigma = 0.27$

Table 2.7. Phenological stages used for inversion strategies 2 and 3 for each crop type in Figure 2.8 images; early, mid, and late phenological stages correspond to emergence, establishment, and maturation.

Crop type	**2-May**	**1-Jun**	**20-Jun**	**15-Jul**
Dicotyledon	Early	Early	Early	Late
Spring Monocotyledon	Early	Early	Mid	Late
Winter Monocotyledon	Early	Mid	Mid	Late

Table 2.8. Regression and validation metrics for *LAI*, C_w, and *CCWC* estimated through the three inversion strategies. The table presents the results obtained considering Landsat-8 (L8) data only, Sentinel-2A (S2) data only, and both sensors (L8/S2).

C_w (10^{-2}g cm^{-2})							
		RMSE	**MAE**	**NSE**	**Slope**	**Intercept**	**R^2**
L8	Strategy 1	1.90	1.50	0.19	0.35	1.89	0.30
	Strategy 2	2.01	1.56	0.07	0.29	1.97	0.24
	Strategy 3	1.90	1.50	0.18	0.27	2.62	0.21
S2	Strategy 1	2.30	1.70	-0.39	0.17	1.80	0.10
	Strategy 2	2.20	1.57	-0.26	0.19	1.77	0.16
	Strategy 3	2.05	1.55	-0.10	0.17	2.36	0.10
L8/S2	Strategy 1	2.04	1.56	0.00	0.30	1.80	0.22
	Strategy 2	2.07	1.57	-0.04	0.26	1.87	0.21
	Strategy 3	1.95	1.53	0.09	0.24	2.49	0.17
LAI (m^2 m^{-2})							
		RMSE	**MAE**	**NSE**	**Slope**	**Intercept**	**R^2**
L8	Strategy 1	1.58	1.25	-0.17	0.57	1.51	0.26
	Strategy 2	1.67	1.31	-0.30	0.47	1.65	0.18
	Strategy 3	1.42	1.14	0.06	0.61	0.86	0.33
S2	Strategy 1	2.30	1.79	-2.07	1.01	1.04	0.30
	Strategy 2	1.73	1.32	-0.73	0.86	0.80	0.31
	Strategy 3	1.44	1.12	-0.19	0.76	0.61	0.34
L8/S2	Strategy 1	1.87	1.44	-0.75	0.71	1.41	0.25
	Strategy 2	1.69	1.31	-0.43	0.59	1.41	0.22
	Strategy 3	1.43	1.14	-0.02	0.66	0.79	0.33
CCWC (10^3g m^{-2})							
		RMSE	**MAE**	**NSE**	**Slope**	**Intercept**	**R^2**
L8	Strategy 1	0.56	0.43	0.59	0.66	0.28	0.63
	Strategy 2	0.59	0.44	0.56	0.57	0.24	0.71
	Strategy 3	0.49	0.35	0.69	0.78	0.09	0.74
S2	Strategy 1	0.46	0.37	0.66	0.66	0.21	0.73
	Strategy 2	0.57	0.43	0.48	0.57	0.16	0.69
	Strategy 3	0.41	0.33	0.73	0.78	0.03	0.82

	Strategy 1	0.53	0.40	0.62	0.66	0.25	0.66
L8/S2	Strategy 2	0.58	0.44	0.53	0.57	0.21	0.70
	Strategy 3	0.46	0.34	0.71	0.78	0.07	0.76

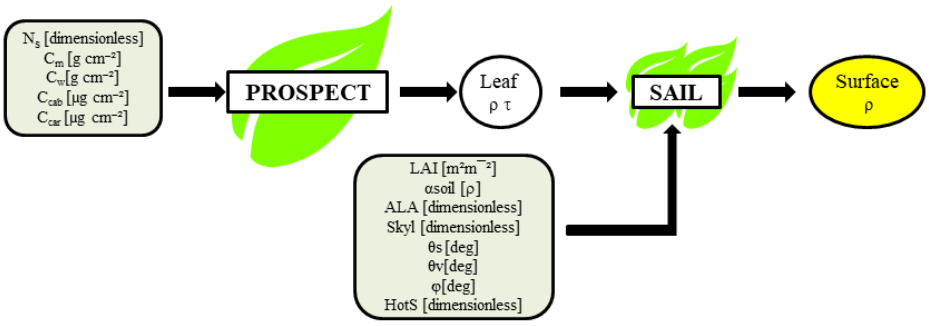

Figure 2.1. Conceptual diagram of PRO4SAIL forward use. The input parameters are listed in the light green boxes with the respective units. The leaf biophysical acronyms definitions: internal leaf structure (N_s), dry matter content (C_m), water content (C_w), chlorophyll content (C_{cab}), and carotenoid content (C_{car}). PROSPECT produces leaf reflectance (ρ) and transmittance (τ) which are used as inputs in SAIL, along with the SAIL canopy architectural inputs: leaf area index (*LAI*), a soil reflectance scale parameter ($\alpha soil$), average leaf angle (*ALA*), fraction of diffuse incoming solar radiation (*skyl*), sun zenith angle (θ_s), sensor viewing angle (θ_v), relative azimuth angle between the sensor and sun (φ), and the hot-spot size parameter (*HotS*) to produce an estimated bidirectional surface reflectance (*surface* ρ).

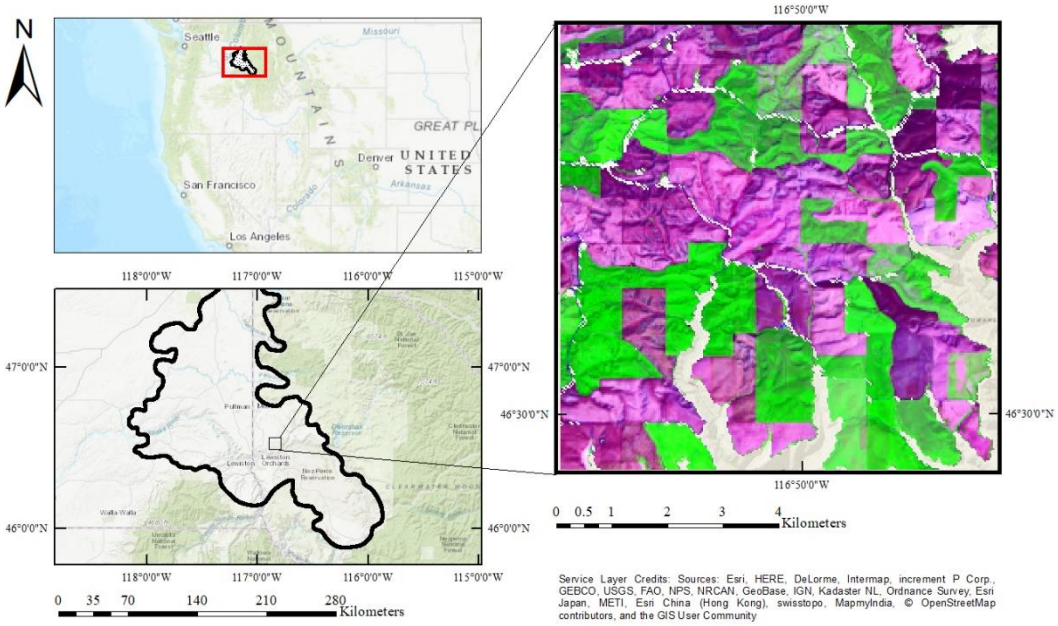

Figure 2.2. Location of the Palouse bioregion within the conterminous United States (top left) and location 8 km by 8 km study area within the Palouse bioregion (bottom left). Biophysical and top of canopy spectral data were collected from plots located in wheat, barley, and garbanzo fields (right). Sentinel-2 HLS product reflectances during early phenological stages for wheat, garbanzo, and barley on 2 May 2016, with crop mask, are used to

provide geographic context and displayed as false color composition: R = SWIR 1.6 (1.57–1.65 µm), G = NIR (0.85–0.88 µm), and B = Blue (0.45–0.51 µm).

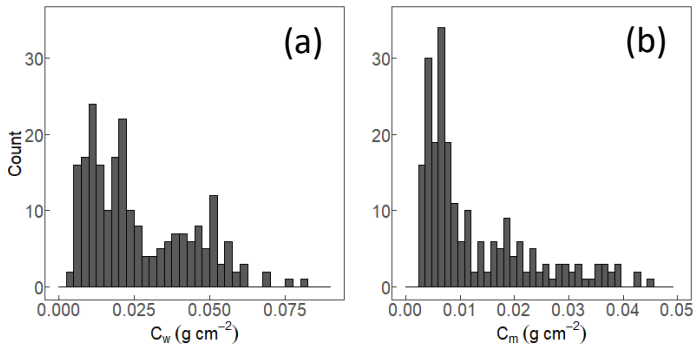

Figure 2.3. Histogram of C_w (**a**) and C_m (**b**), measured on 225 leaf samples grown in controlled conditions.

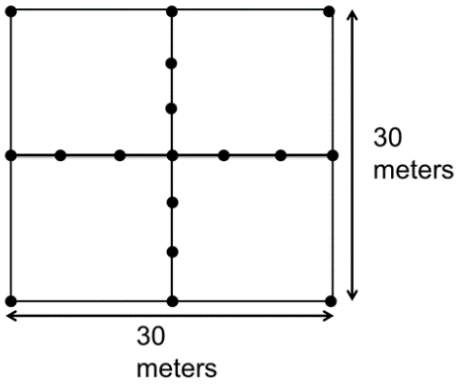

Figure 2.4. Sampling scheme. Measurements were acquired at 17 locations (black dots) within the 30m × 30m plot.

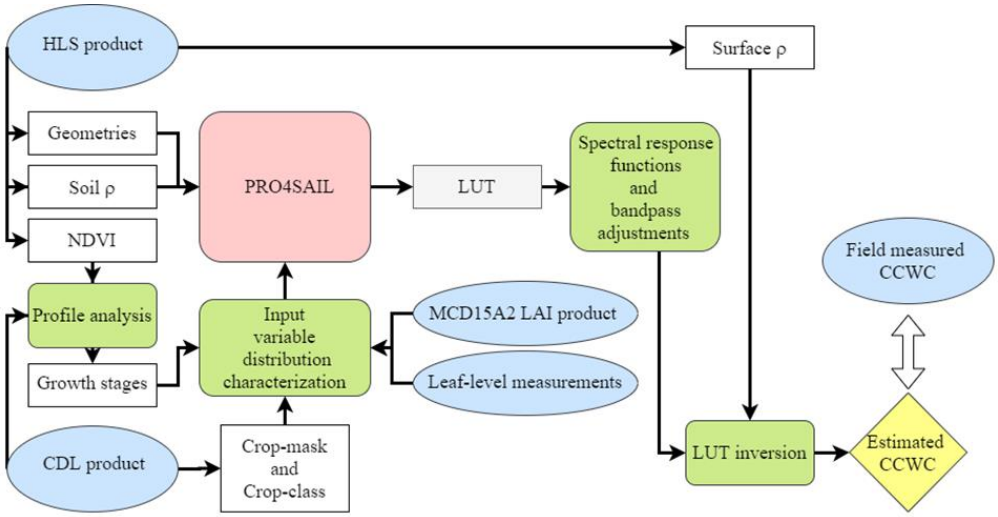

Figure 2.5. Conceptual diagram of PRO4SAIL inversion optimization using *a priori* information and HLS product. Input datasets are presented in the blue ovals while processing steps and intermediate data are presented in the green and white rectangles, respectively. Finally, the final cropland canopy water content (CCWC) output is presented in the yellow diamond.

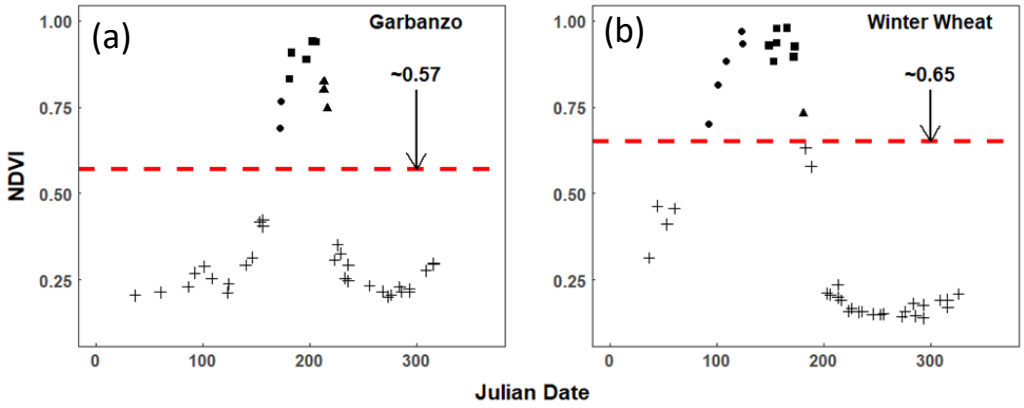

Figure 2.6. Temporal profile of normalized difference vegetation index (NDVI) for a garbanzo plot (**a**) and winter wheat plot (**b**) from 2016. The red dashed line indicates the average between maximum and minimum NDVI observed for each plot during 2016. The value is indicated in the plot. NDVI values are from pixels which passed the QA filter described in the methods section.

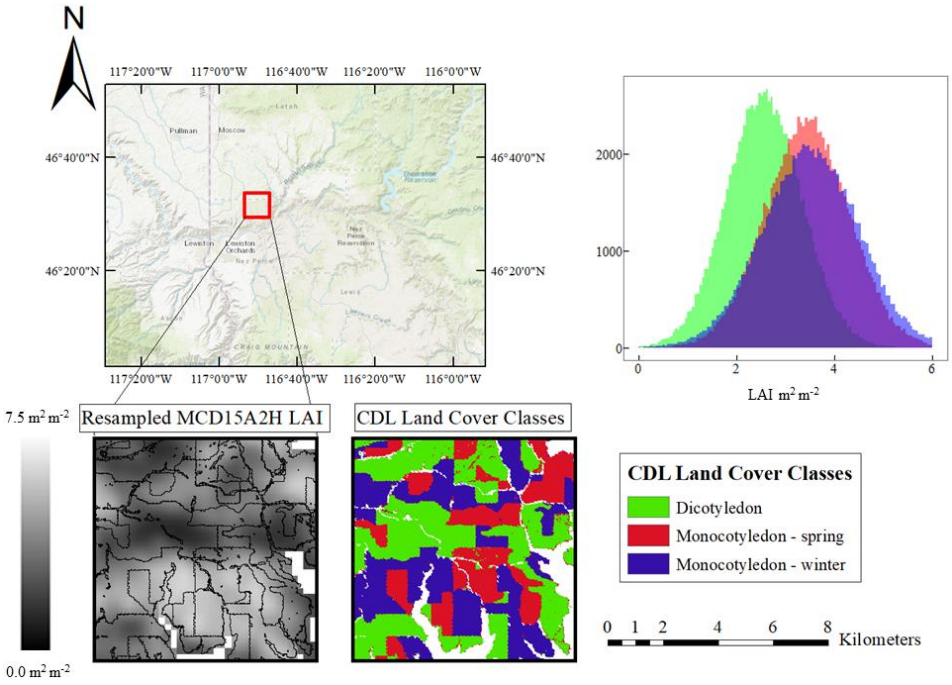

Figure 2.7. Extraction of LAI pdf for each crop type (upper right), obtained by combining the resampled MCD15A2H product from June 1st, 2016 (lower left) and the aggregated CDL product from 2016 (lower right). The resampled MCD15A2H was masked to exclude any area not been identified as cropland by the USDA CDL product.

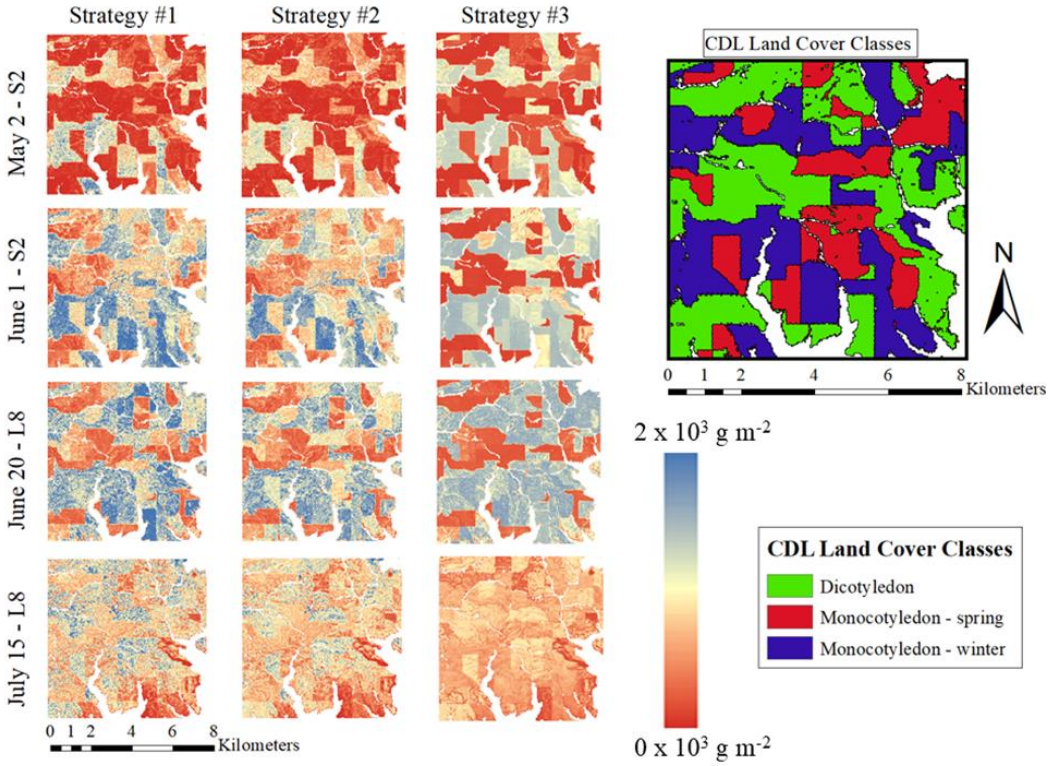

Figure 2.8. HLS-CCWC inversion results on 8 km by 8 km subsets of both Sentinel-2 and Landsat-8 HLS data for each inversion strategy (presented as columns). The inversions were performed during the 2016 growing season for May 2 (top), June 1 (second from top), June 20 (second from bottom), and July 15 (bottom) overpasses. The sensor during overpass as is labeled next to the date as S2 and L8 for Sentinel-2 and Landsat-8, respectively. The corresponding crop-type CDL land cover field boundaries are present on the right.

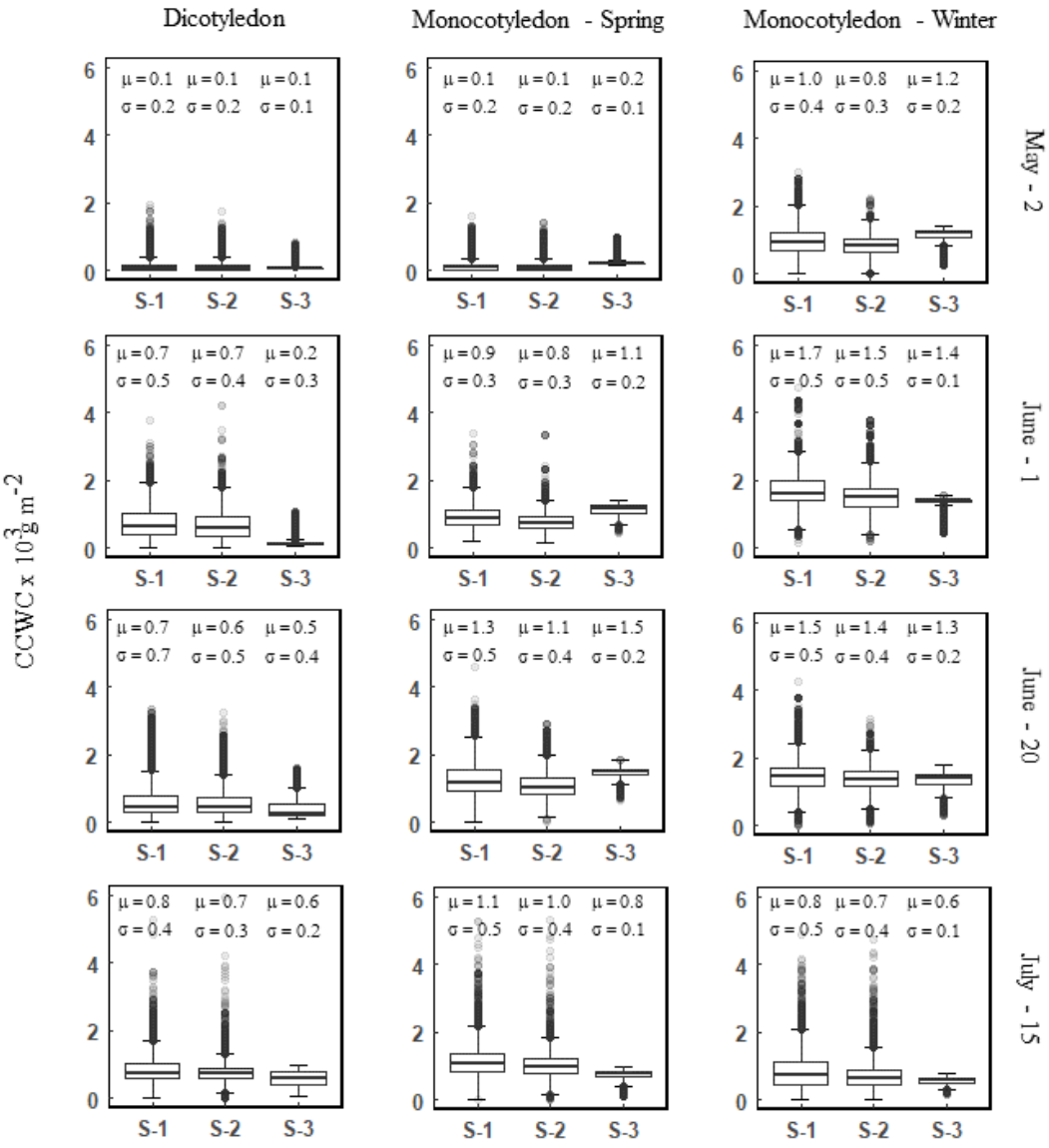

Figure 2.9. Box plots of the distribution of estimated CCWC in the 8 km x 8 km study area for May 2, June 1, June 20, and July 15 during the 2016 growing season. Results are aggregated into CCWC values for each crop-type: dicotyledon (left column), spring monocotyledon (middle column), and winter monocotyledon (right column). Mean and standard deviations are plotted above each respective box plot for each strategy, labeled S-1, S-2, and S-3 for strategy 1, 2, and 3, respectively.

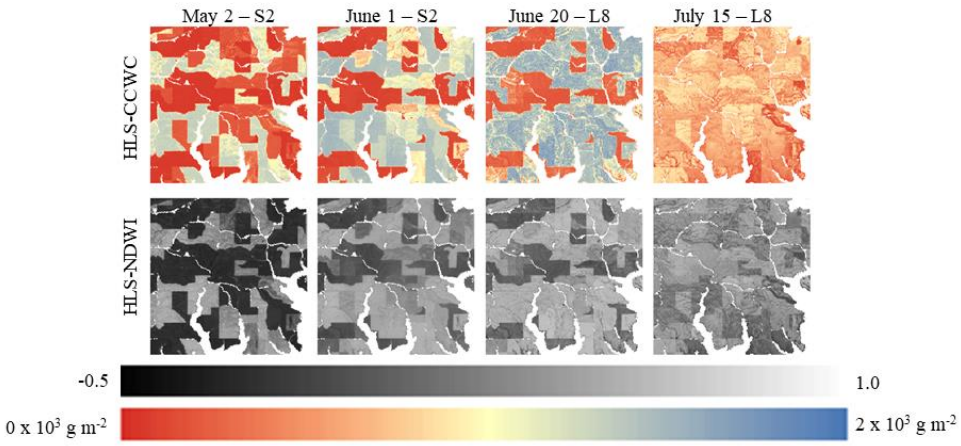

Figure 2.10. Comparisons of strategy 3 CCWC product (top) for each labeled date and sensor (S2 and L8 for Sentinel-2 and Landsat-8, respectively) with the coincident normalized difference water index (NDWI) derived image (bottom) for the 8 km x 8 km study area.

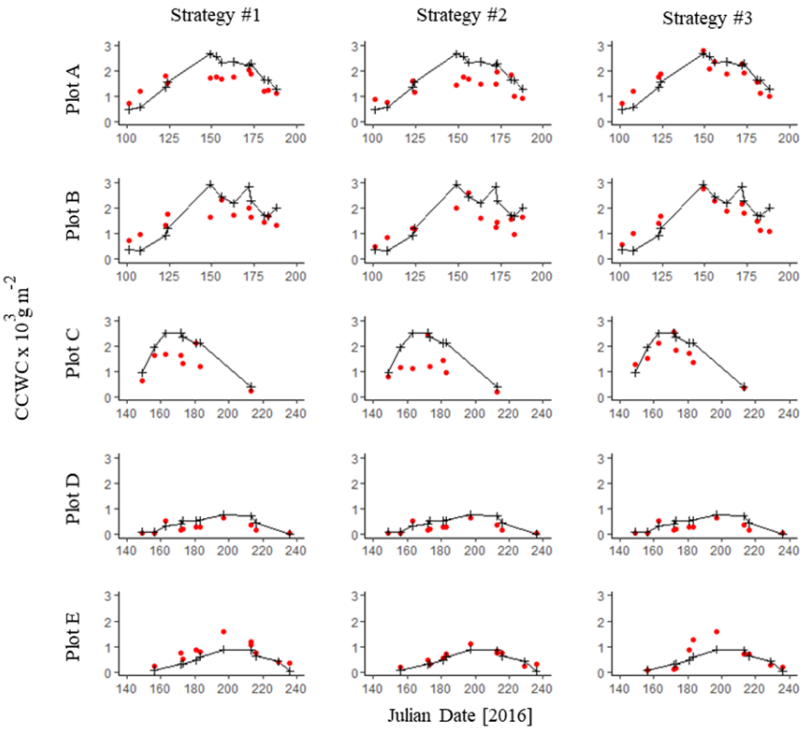

Figure 2.11. Time series of measured (black crosses) and estimated (red dots) *CCWC* for each inversion strategy (#1: left, #2: middle, and #3: right) during the 2016 growing season. Plots A and B were located in winter wheat fields. Plot C was located in a barley field. Plots D and E were located in from garbanzo fields.

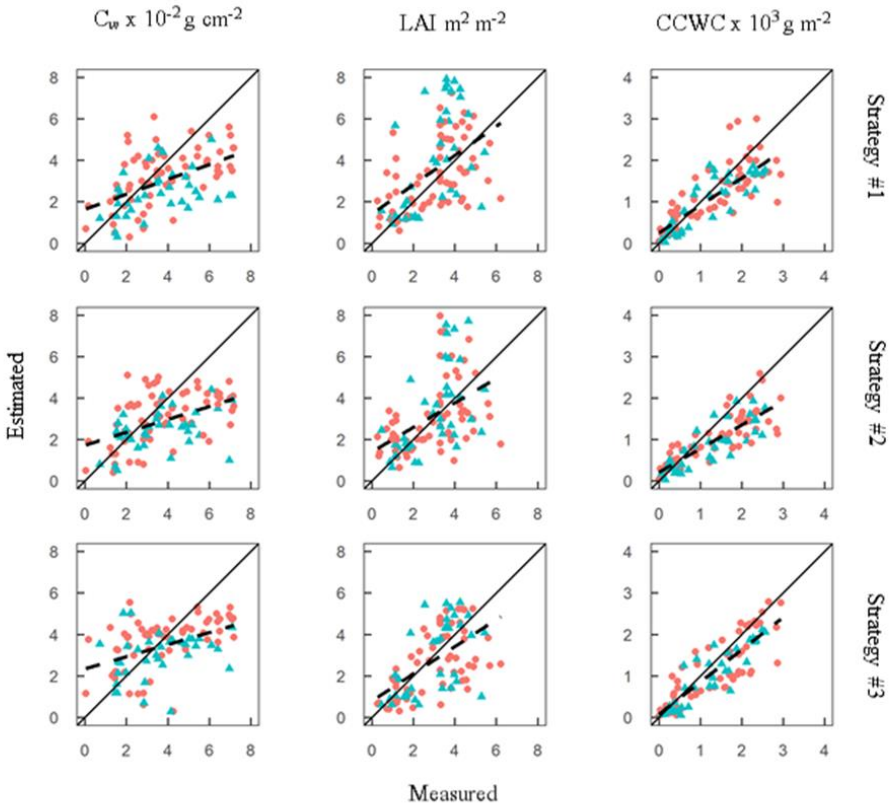

Figure 2.12. Scatter plots of measured and estimated C_w, *LAI*, and *CCWC* (Left, middle, and right, respectively), presented for strategies 1, 2, and 3 (top, middle, and bottom, respectively). The regression lines are plotted as a dashed line, the solid 1:1 line is shown for reference. The red dots and green triangles correspond to Landsat-8 and Sentinel-2 HLS derived observations, respectively.

Chapter 3: Using cropland canopy water content (CCWC) to predict drought stress induced yield loss

Abstract

Drought stress inhibits agricultural productivity more than any other abiotic factor. Traditional methods for monitoring drought require measurements of meteorological variables from weather stations to be used as inputs in drought stress indices but lack the spatial resolution for farm-level yield prediction, especially in data sparse regions. Research, which contributes to mapping and predicting the outcomes of drought stress at the spatial and temporal scales necessary for agricultural monitoring, is of paramount importance, especially when considering the growing availability of 10-30 m moderate resolution satellite products made available by the Landsat and Sentinel satellite missions. The normalized differenced vegetation index (NDVI) is used with success to predict yield in major crops but is limited by its transferability across different regions and during late drought events after the crop has fully established. Cropland canopy water content (CCWC) is the biophysical quantity of water in the canopy which has known relationships with plant health status and may be estimated through inversion of the couple radiative transfer model, PRO4SAIL. In this study, the link between CCWC and yield was explored by combining a previously published logistic relationship between leaf water content (LWC) and available soil water content (ASWC) with the Food and Agricultural Organization (FAO) Irrigation and Drainage 56 definitions of water balances, drought stress, and yield. Using a new framework proposed in this study, which links a time series of satellite-derived CCWC to yield loss through the FAO-56 crop water use framework, yield loss was estimated from Landsat-8 Operational Land Imager (OLI) data for different treatment plots of an independent irrigation study which created late drought during the late vegetative, reproductive, and maturation growth stage in maize (*Zea mays*). The modeled and estimated yield loss from the CCWC time series both corresponded to the treatment amounts of the experiment. The comparison between CCWC and NDVI time series demonstrated CCWC being more sensitive to the different irrigation treatments than NDVI. Finally, the satellite based CCWC estimates were used to predict yield for each of the treatments.

Introduction

Two-thirds of the world's population live under severe water scarcity conditions at least 1 month of the year, while more than a half billion people experience severe water scarcity throughout the year in regions of dense population and intense irrigated agriculture (Mekonnen and Hoekstra 2016). Water-demand, driven by an increasing world population and food demand (Amprako 2016), is projected to be more pronounced in low-latitude regions where more frequent and severe occurrences of extreme heat, drought, and flooding take place (Easterling et al. 2007; Mahlstein et al. 2011). Small-

scale rural agricultural regions, where the agricultural sector is characterized as the primary economic driver, are at the highest risk due to poor infrastructure and farming systems being unable to withstand extreme events (Mthembu and Zwane 2017).

Drought is a meteorological term which is frequently defined as a period without significant rainfall. Drought stress in plants occurs when the rate of transpiration is higher than the rate of water uptake from the soil, resulting in an imbalance in the water supply. Light to moderate drought stress can result in stomatal closure, reduced gas exchange, and reduction in cell enlargement and growth (Jaleel et al. 2009). Prolonged drought stress can lead to the reduction of photosynthesis, metabolic pathway disruption, and cell tissue death. In agriculture, drought stress is the most prominent abiotic factor for yield loss (Boyer 1982; Solomon et al. 2007).

The temporal and spatial distributions of rainfall, evapotranspiration (ET), and soil water holding capacity dictate crop yield and production, and therefore require effective monitoring to characterize drought risk and response actions for mitigating the negative impacts of drought stress on yield. The most historic and accurate methods for monitoring the hydro-climatic drivers of drought stress is through in-situ based indices (Hazaymeh and Hassan 2016). The Palmer Drought Severity Index (PDSI) (Palmer 1965), Crop Moisture Index (CMI) (Palmer 1968), and the Standardized Precipitation Index (SPI) (McKee et al. 1993) are a few examples of the most commonly used in-situ based agricultural drought monitoring indices and are known to provide a comprehensive and accurate view of drought conditions at point locations where the input variables are acquired. The methods presented in the Food and Agriculture Organization (FAO) Irrigation and Drainage Paper 56 have also provided crop water use and yield prediction guidelines and recommendations for landowners, managers, and irrigation consultants for many years and presently (Jovanovic et al. 2020). The FAO-56 paper outlines simple and transferrable methods, based on simple water balancing, crop phenology, and the FAO Penman-Monteith definition of ET, for approximating crop water use and yield for a suite of commonly grown crops (Allen et al. 1998). The strength of the approach is in its ability to be scaled easily and dynamically track yield throughout the season. For any in-situ based drought index, including the FAO-56 crop water use method, uncertainty in the spatial delineation of drought conditions exist in landscapes where the distribution of meteorological stations, to collect the input data, is sparse (Hazaymeh and Hassan 2016; Li and Heap 2014). Remote sensing technology have been widely used to monitor the hydro-climatic drivers of drought stress and yield loss in agricultural landscapes as a solution to lowering the spatial uncertainty of in-situ based indices (Hazaymeh and Hassan 2016).

Satellite-based rainfall estimates are primarily retrieved using thermal infrared imaging methods from geosynchronous satellites. Most rainfall estimate products are 4 to 25 km in spatial

resolution and available daily over 30 years in record (Coleman et al. 2017). This approach uses a technique to estimate cloud height through thermal measurements of the cloud (i.e. clouds at higher altitudes having cooler temperatures) and relies on the assumption that more rain results from clouds with a deeper vertical extent. The main strengths of satellite-based rainfall are the length of record and complete spatial coverage over remote areas (Coleman et al. 2017). Thermal infrared imaging does not measure variation in spatial intensity, which is especially significant in regions where rainfall may be influenced by coastal or mountainous features (Dinku et al. 2011; Sun et al. 2018). A study in Senegal, which examined total seasonal satellite-based rainfall as a metric of crop success, resulted in two villages a few kilometers apart having similar rainfall estimates but reported very different rainfall amounts over the growing season (Coleman et al. 2017). Because the timing of phenology and water deficit is crucial to estimating crop yield loss (Sah et al. 2020; Steduto et al. 2012; Yavuz et al. 2021), characterizing rainfall at a fine temporal resolution during the growing season is critical. This emphasizes the importance of daily rainfall estimates. Daily estimates, however, are cited as having higher uncertainty than monthly estimates (Coleman et al. 2017).

Satellite-based soil moisture products may also be used to track crop water status through change detection of wetness in the soil. Observations from both active and passive microwave sensors are limited to the detection of soil wetness in the upper soil layer (2-5 cm) (Srivastava et al. 2016) with most products being available daily, between 3 km and 50 km in spatial resolution. An advantage of active and passive microwave sensors is the ability to penetrate cloud cover, which is critical in agricultural regions with frequent cloud presence. Since water uptake by the roots occur below the surface, however, additional methods, which require information about the soil properties, are necessary to estimate coincident root-zone soil moisture (Albergel et al. 2008; Wagner et al. 1999). The natural variability of rainfall, topology, soil properties, and even canopy water content also affect the geographic consistency of global soil moisture products (Dorigo et al. 2015).

The optical domain may also be used to retrieve information about the crop's health. The most widely used optical index, NDVI, is recognized as an excellent indicator of the abundance and condition of vegetation (Carlson and Ripley 1997; Magney et al. 2016; Pettorelli et al. 2005), which is especially effective in cases where drought has impacted growth. NDVI and other optical vegetation health indices have the benefit of moderate spatial resolution products (10 m – 1 km), which separates it from most rainfall and soil moisture monitoring methods. The link between NDVI and yield has also been found to be strong in some cases (Duan et al. 2017; Marti et al. 2007), even showing a stronger relationship with yield than rainfall in a pilot study which examined historical crop yield data in Zimbabwe (Makaudze and Miranda 2010). NDVI has also been used in the past to estimate the crop coefficient

(K_c) which is used to link phenology and total leaf area to ET and separates the reference crop from a specific crop in the FAO-56 method (Jovanovic et al. 2020).

Nonetheless, a broader examination of NDVI revealed the relationship between NDVI, rainfall, temperature, and crop yield were still shown to be highly site-specific and, as a result, required calibration for each location (Turvey and Mclaurin 2012). NDVI is also cited as being less straight forward for certain crops where average 'greenness' over a period does not necessarily relate to yield as well as nutrient and water availability during critical growth periods (Hellmuth et al. 2009). The timing of the stress event is often a challenge in connecting remote sensing datasets to yield. In many major crops, including maize, the most important phenological stages related to yield occur later in the season after vegetative growth and during yield formation (Sah et al. 2020). A drought event during the early vegetative or maturity stages would result in relatively little yield loss compared to an event which occurred during late vegetative or reproductive stages. As a result, NDVI is known to have a weaker relationship with yield during seasons with ideal conditions early in the season and drought occurring later in the season before yield formation (Rowley et al. 2007), since growth was able to occur early without being stunted, resulting in full development of the canopy, and in the case of FAO-56, fully established K_c.

Cropland canopy water content (CCWC), defined as the total amount of water stored in the canopy [g m^{-2}], is a biophysical parameter which has been successfully estimated and monitored as an indicator of plant stress in agricultural drought assessment and irrigation decision studies (Yi et al. 2014; Zhang et al. 2017; Zhang and Zhou 2019). Unlike NDVI or other band ratio indices, CCWC represents the physical quantity of water in the canopy, which is a direct indicator of crop water status. Using CCWC as an indicator of crop water status also enables the use of the physical-based radiative transfer model (RTM) inversion methods, which has a known advantage over empirical-based approaches in transferability (Grossman et al. 1996; Li and Wang 2011; Yebra et al. 2013). Finally, to our knowledge, no study exists which examines the link between CCWC and FAO-56 definitions of crop water use, drought, and yield loss. The development of a remotely sensed biophysical estimate, which can be assimilated into the FAO-56 crop water use framework, may enable FAO-56 application for farm-level water mapping and precision irrigation (Pereira et al. 2020).

The goal of this study was to develop the first steps towards a novel method which exploits a time series of satellite estimated CCWC to predict the yield loss in maize. To do this, two objectives were met: 1) establish the theoretical link between CCWC, drought stress, and yield loss using well known crop water use equations from the FAO-56 paper and previously established relationships

between leaf water content (LWC) and available soil water content (ASWC), and 2) evaluate the method using a published irrigation experiment dataset with known water control inputs, meteorological conditions, and phenological information.

Methods and Materials

Theoretical link between CCWC, drought stress, and yield loss

In this section, we define the theoretical link between CCWC and yield loss using previously published definitions and relationships. In the following subsections, we first define drought stress and resulting yield loss using the FAO-56 crop water use and soil water balance equations. Second, we establish a link between CCWC, and the FAO-56 crop water use and soil water balance framework.

FAO Irrigation and Drainage paper 56 drought stress and yield loss

The FAO-56 definition of drought stress in crops is characterized by a crop water use approach: calculated using daily ET, water inputs through rainfall and irrigation, and various field specific information related to crop species, phenology, and soil properties (Allen et al. 1998). The FAO-56 crop water use approach was developed and intended to provide guidance to land managers and researchers for approximating crop water requirements for both rainfed and irrigated agricultural systems. In this study, the FAO-56 crop water use approach was used to define the moment in which drought stress occurs. There are several FAO-56 terms and definitions which require explanation. First, the reference ET (ET_o) [mm day^{-1}] is calculated using the FAO Penman-Monteith method (Allen et al. 1998; Monteith 1965) and is defined as the amount of water that would be lost through the combined process of evaporation and transpiration by a hypothetical reference grass surface with unlimited water supply. ET_o is expressed below:

$$\mathrm{ET}_o = \frac{0.408\Delta(R_n - \mathrm{G}) + \gamma \frac{900}{T + 273} u_2 (e_s - e_a)}{\Delta + \gamma(1 + 0.34u_2)}, \quad (1)$$

where R_n is net radiation at the crop surface [MJ m^{-2} day^{-1}], G is soil heat flux density [MJ m^{-2} day^{-1}], T is air temperature at 2 m height [˚C], u_2 is wind speed at 2 m height [m s^{-1}], e_s is saturation vapor pressure [kPa], e_a is actual vapor pressure [kPa], Δ is slope vapor pressure curve [kPa ˚C^{-1}], and γ is psychrometric constant [kPa ˚C^{-1}].

Next, the potential ET (ET_c) [mm day^{-1}] is defined as the amount of water that would evaporate and transpire by a specific crop surface (i.e. maize, soy, wheat, etc.) with unlimited water supply. ET_c is calculated using the single crop coefficient method and is expressed below:

$$\mathrm{ET}_c = ET_o * K_c\,, \tag{2}$$

where K_c is the dimensionless crop coefficient term. K_c represents an integration of four properties that distinguish a specific crop from the reference grass: 1) crop height, 2) albedo, 3) canopy resistance, and 4) evaporation from the soil (Allen et al. 1998). Consequently, K_c primarily varies by crop species and growth period. A table of K_c values for different crops and growth stages are available in the FAO-56 paper (Allen et al. 1998). There are two growth periods where K_c remains constant: $K_{c\ ini}$ [initial season], and $K_{c\ mid}$ [mid-season]. The period between $K_{c\ ini}$ and $K_{c\ mid}$ growth period is called $K_{c\ dev}$. The approximation of K_c between each of the three growth periods, as well as the $K_{c\ end}$ [late season], is expressed as:

$$\mathrm{K}_{C\,i} = K_{c\,prev} + \left[\frac{\mathrm{i} - \sum(L_{prev})}{L_{stage}}\right](K_{c\,next} - K_{c\,prev}), \tag{3}$$

where i is the day number within the growing season, $K_{c\ i}$ is the crop coefficient on day i, L_{stage} is the length of the stage under consideration [days], and $\Sigma(L_{prev})$ is the sum of lengths of all previous stages [days]. Similar to the K_c values of different crops and periods, a table of reference L_{stage} values may be retrieved from the FAO-56 paper for approximating a seasonal K_c curve. An example of the K_c curve for maize plotted over time (days in season) is presented in Figure 3.1.

Lastly, the actual ET ($ET_{c\ adj}$) [mm day^{-1}] is defined as the actual amount of water that would evaporate and transpire by a specific crop surface through considering soil water supply and crop stress conditions. $ET_{c\ adj}$ is expressed below:

$$\mathrm{ET}_{c\,adj} = ET_o * K_c * K_s\,, \tag{4}$$

where K_s is a dimensionless transpiration reduction factor dependent on available water content in the soil [0 – 1]. K_s may be calculated through a simple water balance approach:

$$\mathrm{K}_s = \frac{\mathrm{TAW} - D_r}{TAW - RAW}, \tag{5}$$

where D_r is the root-zone depletion [mm], TAW is the total available soil water in the root-zone [mm]:

$$TAW = 1000 * (\theta_{FC} - \theta_{WP}) * Z_r\,, \tag{6}$$

where θ_{FC} is the water content at field holding capacity [m^3 m^{-3}], θ_{WP} is the water content at wilting point [m^3 m^{-3}], and Z_r is the rooting depth [m]. RAW from equation 5 is the readily available soil water in the root-zone [mm]:

$$RAW = \mathrm{p} * \mathrm{TAW}, \quad (7)$$

where p is the average fraction of total available soil water (TAW) that can be depleted from the root-zone before moisture stress (reduction in ET) occurs [0 – 1]. A conceptual diagram of the water balance terms above is presented in Figure 3.2. The K_s value curve, plotted over the amount of water approximated in the balance, is presented in Figure 3.3.

Root-zone water content may be expressed by depletion (D_r) (i.e. the water shortage relative to field holding capacity). As water is removed from the soil, D_r increases. When D_r becomes equal to or exceeds RAW, drought stress will be induced, stomatal closure on the leaves will begin to conserve water, and K_s will begin to decrease until reaching the wilting point and total crop failure is achieved. Any period where K_s is less than one is a period where the crops are defined as experiencing drought stress. The simple water balance computation for the root-zone, which approximates daily D_r, is done through the means of a "container-like" system in which water may fluctuate: subtracting water through daily ET and adding water through daily precipitation or irrigation. It is assumed that water may be stored in the container until field holding capacity is reached, with any additional water added to the container through heavy rain or excessive irrigation being lost the same day by deep percolation and runoff. Likewise, it is assumed depletion cannot exceed the wilting point, as no more water will be left for evapotranspiration in the root-zone.

Finally, the FAO introduced a set of rules in the FAO Irrigation and Drainage paper 33 for predicting yield loss depending on the phenological period and the number of days with drought stress which were presented in FAO-56 (Doorenbos and Kassam 1979). The yield loss ratio ($\frac{Y}{Ym}$), opposed to a quantity of yield, may be estimated using:

$$\frac{Y}{Ym} = \prod_{n=1}^{N}\left[1 - K_{y\,n}(1 - K_{s\,n})\right], \quad (8)$$

where Y is the actual yield, Ym is the maximum yield, K_y is the yield response factor, n is an index representing each growth stage, and N corresponds to the number of functions between the square brackets (Doorenbos and Kassam 1979).

The K_y factor describes the reduction in relative yield according to the reduction in $ET_{c\ adj}$ caused by soil water shortage. The K_y values are crop specific and vary depending on the growth stage. In general, a decrease in yield from drought stress during early vegetative development will be relatively small, while drought stress during flowering and yield formation stages will be large. Crop and growth stage specific values are available in the FAO Irrigation and Drainage paper 66 (Smith and

Steduto 2012). The K_y values used in this study were 0.4, 1.5, 0.5, and 0.2 for vegetative, flowering, yield formation, and ripening growth stages, respectively.

Plant-soil water content relationship

The relationship between plant and soil water content is critical for characterizing the water-carbon and energy exchange processes in the soil-plant-atmosphere system (Giménez et al. 2013; Ouyang and Zheng 2000). Several methods for modeling the relationship and flow of water from the soil to the leaf tissue of a plant exist in varying degrees of complexity (e.g. (Grifoll et al. 2005; Sperry et al. 1998)). In this study, a logistic function, which was used in a recent publication (Zhou et al. 2021) for linking maize leaf water content (LWC) to available soil water content (ASWC), was used to quantify the plant-soil water content relationship. LWC is expressed as:

$$LWC = \frac{LFW - LDM}{LFW} * 100\% \quad (9)$$

where LFW is the fresh leaf weight and LDM is the dry leaf weight. ASWC is expressed as:

$$ASWC = \frac{SWC - WP}{FHC - WP} * 100\%, \quad (10)$$

where SWC is the soil moisture content [mm], FHC is the field holding capacity [mm], and WP is the wilting point [mm]. The logistic function to link LWC to ASWC used in Zhou et al. (2021) is expressed as:

$$LWC = LWC_{max} + \frac{LWC_{min} - LWC_{max}}{1 + \left(\frac{ASWC}{b}\right)^{a}}, \quad (11)$$

where LWCmax and LWCmin represent the maximum and minimum leaf water content, respectively. The parameter *a* represents a value that is proportional to the sensitivity of LWC in response to changing ASWC, and parameter *b* represents the ASWC value when LWC is the midpoint between LWCmax and LWCmin. LWCmax and LWCmin values were set based on the LOPEX93 leaf data set (Hosgood et al. 1995) for maize values: 80.9 % and 65.5%, respectively. Parameters *a* and *b* were estimated using similar methods as outlined in Zhou et al. (2021). A maximum iteration algorithm (Nelder-Mead) (Nelder and Mead 1965) was run until the minimum sum of squares was found. The parameter values for *a* and *b* were determined to be 4.79 and 51.04, respectively. These values were similar to those used in the Zhou et al. (2021) paper.

The primary objective of this study was to establish and evaluate the link between CCWC retrieved from satellite observations and yield loss. Since the relationship between plant and soil water

content is expressed as a relationship between LWC and ASWC (eq. 11), necessary conversions were made to enable the use of CCWC to estimate soil water content for K_s estimation, and subsequent yield ratio estimation. CCWC is converted to LWC through the following equations:

$$EWT = \frac{CCWC}{LAI}, \tag{12}$$

where EWT is the equivalent water thickness [g cm^{-2}], which represents the total weight of water over a square centimeter of leaf surface area and LAI is the leaf area index [m^2 m^{-2}], which represents the total leaf area in a square meter of ground area. EWT estimated from CCWC and LAI is used to approximate the LWC percentage:

$$LWC = \frac{EWT}{EWT + DMC} * 100\%, \tag{13}$$

where DMC is the dry matter content [g cm^{-2}], which represents the total weight of dry matter over a square centimeter of leaf surface area. The LWC is inverted through equation 11 to approximate the coincident ASWC. ASWC is used to estimate K_s through D_r:

$$Dr = TAW - \left(\frac{ASWC}{100} * TAW\right), \tag{14}$$

The D_r is then used as an input in equation 5 which can be used to estimate the yield ratio in equation 8.

Evaluation of theoretical link between CCWC, drought stress, and yield loss

The goal of the evaluation was to test whether the FAO-56 and CCWC-ASWC relationships, presented in the first section, can be combined to produce the basis of an approach for monitoring changes in yield ratios using a satellite derived CCWC time series. This was performed by 1) modeling CCWC and the resulting yield ratio for a set of published experimental irrigation treatment data with known environmental controls, soils, and crop phenology using the FAO-56 crop water use framework and a simple crop model and, 2) performing RTM inversion using Landsat-8 OLI surface reflectances to create the CCWC time series to be used for estimating yield loss in each treatment of the irrigation experiment and compare with the modeled CCWC and yield loss. The methods for evaluating the theoretical link between CCWC and yield ratio are presented in the following subsections.

Irrigation experiment

Published water treatment data, phenology, and soil properties information from an independent field-level irrigation experiment in Inner Mongolia, China (Zhang et al. 2019), were used to 1) evaluate the applicability of CCWC and NDVI in mapping late drought conditions, and 2) evaluate

the time series of CCWC to predict yield for each irrigation treatment. Briefly, the purpose of the Zhang et al. (2019) study was to evaluate methods for mapping water stress in maize using several band ratio vegetation indices under various water deficit conditions during late vegetative, reproductive, and maturation growth stages. The irrigation experiment was conducted on a 1.13 ha irrigation pivot maize research field (40˚ 2600.29" N, 109˚ 36025.99" E, Elev. 1010 m), located in Zhaojun Town, Dalate Banner, Ordos, Inner Mongolia, China (Figure 3.4). The maize for the experiment was planted on May 20, 2017 and harvested as silage 110 days later

FHC and WP were estimated to be 12.9% and 5.6% volumetric using multiple soil samples taken from the research field. Water treatments were designed and based on the crop water use FAO definitions. The K_c values reported in the irrigation experiment were 0.55, 1.09, and 0.45 during the initial, mid-season, and late season developmental stages. More information about the study areas soils and the irrigation system may be retrieved from Zhang et al. (2019). The applied irrigation for each treatment is presented in table 3.1.

According to Zhang et al. (2019) the total crop water requirements of the maize during the late vegetation, reproductive, and maturation stages was estimated to be 407 mm, which was approximate to the total water applied to the control treatment (402 mm in treatment 1). Each of the other treatments were a percentage of the water applied to treatment 1.

Soil Water Balance and K_s Estimation

As described in the *FAO Irrigation and Drainage paper 56 drought stress and yield loss* section above, daily D_r is required for estimating daily K_s of each treatment. To do this using the information from the Zhang et al. (2019) study, a daily soil water budget was characterized for each treatment throughout the study period:

$$D_{r\,t} = FHC - SWC_t, \tag{15}$$

where FHC is the field holding capacity [mm] and SWC_t is the soil water content [mm] at time t:

$$SWC_t = SWC_{t-1} - (ET_{c\,t-1} - WI_{t-1}), \tag{16}$$

where WI is the daily water applied [mm]. Daily ET_c was approximated using the values in table 3.1 over the period of the treatment. For example, the total crop water requirements for the maize plants during the late vegetative period (25 days in length) was 188 mm so the estimated daily ET_c for the period was 7.52 mm. Because treatment 1 was administered based on the total crop water requirement, the ET_c over the period was equal to the total the amount of water administered to treatment 1, while

other treatments received a percentage of this water throughout the treatment period. This daily water applied is expressed by:

$$WI_t = ET_{c\,t} * (1 - TRT_t), \quad (17)$$

where TRT is ratio between water applied and the total crop water requirement (0 - 1) and $ET_{c\,t}$ is the total daily crop water requirement for day t. It is assumed that the experiment was initialized on planting date with the soil water content equal to the field holding capacity ($D_r = 0$). Finally, daily K_s may be estimated using daily D_r in equations 5 and 7 above. The average fraction of TAW (p) is dependent on the crop and may change throughout the season dependent on water requirements:

$$p_t = p_{table22} + 0.04 * (5 - ET_{c\,t}), \quad (18)$$

where $p_{table22}$ is a predefined value for a specific crop which may be retrieved from table 22 of the FAO-56 paper (Allen et al. 1998). $p_{table22}$ was set for maize ($p_{table22} = 0.55$).

Simple Crop Model

A set of stepwise equations were used to simulate leaf area index (LAI) [m^2 m^{-2}], dry matter content (DMC) [g cm^{-2}] and equivalent water thickness (EWT) [g cm^{-2}] for maize over the growing season of the different treatments of the Zhang et al. (2019) irrigation experiment. The goals of the simple crop model were to 1) generate K_c, LAI, and DMC values required to assimilate satellite-derived CCWC into the FAO-56 framework, and 2) evaluate the satellite derived yield loss prediction against the yield loss prediction through inputting the known water control, soil capacity, and ET conditions into the FAO-56 water balance equation. The overall process is expressed as:

$$(DMC, EWT, LAI, Kc) = f(DSP, aGDD), \quad (19)$$

where days since planting (DSP), and accumulated growing degree days (aGDD) were used as inputs in a function to approximate DMC, EWT, LAI, and K_c parameters. To begin, K_c is approximated using DSP and the steps described in the *FAO Irrigation and Drainage paper 56 drought stress and yield loss* section. However, since K_c values and lengths of the growing season and study area were retrieved from the Zhang et al. (2019) paper, the only period required for estimation was the end of the $K_{c\ ini}$ period. According to FAO, $K_{c\ ini}$ ends when canopy cover (CC) [%] reaches a value greater than 10% (Allen et al. 1998). A FAO approach was used which inputs aGDD to approximate CC. To calculate aGDD, the daily maximum and minimum temperature was retrieved from the NASA Project Data

Portal (accessed via: http://power.larc.nasa.gov/), between May 20 and September 7, 2017 for the center coordinates of the irrigation pivot. Daily aGDD was calculated by:

$$aGDD = \sum_{t=1}^{n} GDD_t, \quad (20)$$

where GDD was calculated as:

$$GDD = max\left(\frac{T_{max} + T_{min}}{2} - T_{base}, 0\right), \quad (21)$$

where T_{max} and T_{min} are the maximum and minimum daily temperature [˚C], and T_{base} is the base temperature for maize which was set to 8 ˚C according to crop tables in Allen et al. (1998). CC is estimated by:

$$CC = CC_o * e^{aGDD*CGC}, \quad (22)$$

where CC_o is defined as the soil surface covered by an individual seedling at 90% emergence [cm^2 $planet^{-1}$] and CGC is the canopy growth coefficient [fraction per growing degree day]. CC_o and CGC were set to nominal values for maize according to Allen et al. (1998): 0.0048 cm^2 $plant^{-1}$ and 0.012 fraction per growing degree day for CC_o and CGC, respectively. Next, LAI is estimated through adapting a K_c equation (eq. 2) in Beeri et al. (2020):

$$LAI = -\frac{-0.3547 + \sqrt{-0.1132 * Kc + 0.1345}}{0.0566}, \quad (23)$$

Next, a maize biomass allometric equation (Lemaire et al. 2007; Plénet and Lemaire 1999) was used to estimate DMC from LAI:

$$DMC = \frac{LAI}{1.234}^{1.473} * 0.001, \quad (24)$$

EWT and CCWC were estimated using the theoretical relationship between LWC and ASWC from the Zhou et al. (2021) study. To do this, the SWC was estimated on a daily time step using the simple water balance output from equation 16 which were input into equation 11 to estimate LWC. The LWC was used to compute a daily estimate of EWT using the relationship from equation 13. Finally, CCWC was estimated by multiplying LAI and EWT.

Landsat-8 OLI Collection 2 Level-2

Seven cloud-free Landsat-8 OLI Collection 2 Level-2 surface reflectance scenes were accessed from the USGS EarthExplorer web GUI (accessed via: http://earthexplorer.usgs.gov/). Collection 2 includes several improvements to collection 1 including improved radiometric calibration, geometric accuracy, digital elevation modeling, and QA band (Hartpence 2021). Level-2 surface reflectance is generated from Collection 2 Level-1 data that meet the < 76 degrees solar zenith angle constraint. The imagery that pass this constraint are processed using the Land Surface Reflectance Code (LaSRC) algorithm for correcting atmospheric effects (Skakun et al. 2019). Scenes were acquired for overpasses between June 11 and August 30, 2017. Table 3.2 presents the dates, path, and row imagery used in this analysis is presented.

Surface reflectances values were taken from a single fixed pixel, located near the middle of the treatment zone, for each treatment and overpass date. The NDVI was calculated for each treatment pixel location and date:

$$NDVI = \frac{\rho nir + \rho red}{\rho nir - \rho red}, \tag{25}$$

where ρred and ρnir are the red and near-infrared Landsat-8 reflectances, respectively.

Estimating CCWC using PRO4SAIL Inversion

CCWC was estimated using Landsat-8 reflectances through PRO4SAIL inversion (Jacquemoud et al. 2009). The PRO4SAIL model is the coupled result of the leaf model PROSPECT (Jacquemoud and Baret 1990) and canopy model 4SAIL (Verhoef 1984; Verhoef et al. 2007).

The PROSPECT model generates synthetic leaf directional-hemispherical reflectance and transmittance spectra between 400-2500 nm. The model generalizes a leaf as a stack of plates (N_s) with absorption properties which are governed by the coefficients of their respective leaf constituents and refractive indices. The PROSPECT-5B model was used in the version of PRO4SAIL used in this analysis.

To couple PROSPECT with 4SAIL, the outputs of leaf reflectance, transmission, and absorption from PROSPECT is assimilated into 4SAIL and, along with other canopy structure property parameters, calculates top-of-canopy surface reflectance between 400-2500 nm. The 4SAIL model considers a canopy system as a horizontal one-dimensional turbid medium made up of leaves which are randomly distributed with a characterized leaf orientation and density.

The PRO4SAIL model has been widely used with success decades after its first release (Colombo et al. 2008; Darvishzadeh et al. 2008; Yebra et al. 2013; Zarco-Tejada et al. 2003), but particularly in agriculture (Atzberger 2004; Verger et al. 2011; Zhang et al. 2017) as the model assumes a turbid homogenous canopy system for surface reflectance calculation. The inversion of PRO4SAIL is performed by minimizing the distance between measured and modeled spectra, which in the case of Earth observation sensor measurement comparison, spectral resampling is required to make the comparison possible. Several methods exist for minimizing distance between measured and modeled spectra (Atzberger 2004, 2010; Berger et al. 2018), with Look-Up-Table (LUT) methods as one of the more popular methods due to its simplicity and computational requirements (Rivera et al. 2013). The LUT method requires the user to generate a large table of spectral realizations, traditionally a size of 100,000, and then locate the realization with the smallest difference with the measured spectra. LUT inversion of Landsat-8 reflectances was used to estimate CCWC following the spectral pre-processing and LUT strategy 1 methods outline in Boren and Boschetti (2020). A table of PRO4SAIL parameters and constraints are presented in table 3.3.

Statistical comparison between modeled and satellite derived variables

A quantitative comparison was made between the modeled NDVI, CCWC, and yield loss ratio values to those that were estimated from Landsat-8 OLI observations through calculation of the root mean squared error (RMSE):

$$RMSE = \sqrt{\frac{\sum_{i=1}^{n}(y_i' - y_i)^2}{n}}, \quad (26)$$

where yi and yi' are the modeled and satellite derived values, respectively, and n the number of measurements.

Results

Modeled NDVI, CCWC, and Yield Ratio

The K_c value was estimated over the entire season using a combination of FAO values and published information about the field experiment in Zhang et al (2019). The K_c curve for the maize grown in the Zhang et al (2019) experiment and coincident aGDD is shown in Figure 3.5. A description of values in figure 3.5 is presented in table 3.4.

The K_c curve was computed primarily using the published field information from the Zhang et al. (2019) experiment, including $K_{c\ ini} = 0.55$, $K_{c\ mid} = 1.09$, $K_{c\ end} = 0.45$, and the lengths of $K_{c\ mid}$ and $K_{c\ end}$ stages, 22 and 18 days respectively. The lengths of $K_{c\ ini}$ and $K_{c\ dev}$ (the time between $K_{c\ ini}$ and $K_{c\ mid}$)

was determined using the canopy coefficient equation 3: the estimated time for canopy development to reach > 10% was 25 DSP. With the known start days of $K_{c\ dev}$ and $K_{c\ mid}$, the length of $K_{c\ ini}$ and $K_{c\ dev}$ was determined to be 25 and 45 days, respectively.

The K_c values in figure 3.5 were used to begin the step-wise computation of biophysical parameters (eq 23 - eq 24). Using the methods outlined in the *FAO Irrigation and drainage paper 56 drought stress and yield loss* subsection, the yield ratio for each treatment of the irrigation experiement in Zhang et al. (2019) was estimated. Lastly, the biophysical parameters were inputted into the PRO4SAIL model to produce Landsat-8 like surface reflectances which were used to calculate a NDVI time series at the same time step of actual Landsat-8 overpasses. The modeled CCWC, treatment yield ratios, and NDVI times series are presented in figure 3.6.

Figure 3.6 illustrates peak CCWC is reached (CCWC = 1.16 x 10^3 g m^{-2}) after the late vegetative period ends and the reproductive period begins. During the late vegetative period, treatments 2-5 began to diverge from treatment 1. At the end of the late vegetative period, there was a modeled 0.24 x 10^3 g m^{-2} difference between treatment 1 and the remaining treatments. During the reproductive period, treatment 4 was 69% of the total crop water requirements, while treatments 2, 3, and 5 were 97%, 95%, and 94%, respectively, according to Zhang et al (2019). Treatment 4 CCWC decreased 0.35 x 10^3 g m^{-2} from July 29 to August 20, while treatments 2,3, and 5 decreased 0.08 x 10^3 g m^{-2},0.13 x 10^3 g m^{-2} , and 0.15 x 10^3 g m^{-2} , respectively. Following the prescribed treatments to compute the soil water balance, treatment 4 reached wilting point by the end of the reproductive period.

The modeled yield ratio time series for each treatment reflected the amount of water each treatment received. The quickest drop in yield ratio was modeled for treatment 4, where the yield ratio decreased approximately 0.9 within the first 14 days of the reproductive period and approached zero at the end of the reproductive period. This was an expected result of treatment 4, which was 69% crop water use during the reproductive period and resulted in the soil water balance reaching wilting point at the end of the period. The modeled yield ratio for treatments 2 and 3 started to decrease during the onset of the maturation period. The resulting yield ratios for treatments 2 and 3 were 0.7 and 0.61, respectively at the end of the maturation period. The yield ratio began to decrease towards the end of the reproductive treatment (yield ratio of 0.99 at the end of the reproductive period) but stabilized during the beginning of the maturation period when water treatment was 100% of crop water use. As expected, the yield ratio was unchanged for treatment 1 as water treatment was never below 100% of crop water use for the entire time series.

The resulting shape of the NDVI time series curve was as expected: increasing NDVI during the vegetative period corresponding to growing LAI, peaking during the reproductive stage, and declining during maturation. The largest modeled NDVI difference between treatments did not surpass 0.001 for the entire time series and occurred during the maturation stage.

Observed NDVI and Estimated CCWC and Yield Ratio

The NDVI, estimated CCWC from PRO4SAIL inversion of Landsat-8 surface reflectances, and approximated yield using coincident CCWC estimates is presented in figure 3.7.

NDVI and CCWC progressed on each date as expected, increasing from June 11 to July 29, peaking on July 29, and decreased from August 7 to August 30. Differences between treatment 4 and the rest of the treatments were more evident in the CCWC images than with NDVI from August 7th onwards. The CCWC image on August 30 clearly shows the contrast in values between treatments 1 and 4. In general, yield ratio was not observed to decrease until August 7: nine days after the reproductive treatments began. Like the CCWC image, clear contrast can be seen in the estimated yield ratios between treatments 1 and 4. The sampled pixel time series for each treatment is illustrated in Figure 3.8.

The general trends between modeled CCWC and NDVI values in figure 3.6 and observed CCWC and NDVI values in 3.8 show agreement. Very little separation can be seen in the observed NDVI between treatments, with a max difference of 0.11 observed between treatment 1 and 4 on the last observation date. The RMSE between modeled and observed NDVI was 0.14. Similar to figure 3.6, CCWC does show a peak on July 29 for each treatment and the time series ends in the expected order of treatment, with highest satellite-dervied CCWC in treatment 5 (CCWC = 1.1 x 10^3 g m^{-2}) and lowest CCWC in treatment 4 (CCWC = 0.8 x 10^3 g m^{-2}). The RMSE between modeled and satellite-derived CCWC was 0.17 x 10^3 g m^{-2} . Unlike the values presented in figure 3.6, however, CCWC is shown decreasing from July 29 onward for each treatment, including treatment 1. The yield ratio estimated using the satellite-derived CCWC time series illustrates a yield ratio loss in order of water treatment at the end of the season (1, 0.98, 0.97, 0.4, and 1 for treatments 1, 2, 3, 4, and 5, respectively). The RMSE between modeled and satellite-derived yield ratio was 0.16.

Discussion

This study proposed a link between CCWC and drought stress and demonstrated an approach to estimate yield loss in drought stressed maize from satellite retrieved CCWC. The modeled NDVI and CCWC showed good agreement with the observed NDVI and satellited-derived CCWC (RMSE of 0.14 and was 0.17 x 10^3 g m^{-2}, respectively). The time series of NDVI in figure 3.6 and figure 3.8 fit

closely except for early dates in the timeseries, where the first observed NDVI was ~0.2 for each treatment and modeled was ~0.4 for each treatment. The forward mode of PRO4SAIL was run assuming dry soil conditions, whereas the soil was likely wetter during overpass in the early season from abundant water application of the irrigation system. After LAI grew > 2 m^2 m^{-2}, the overall spectral signature of top-of-canopy reflectance produced by PRO4SAIL was no longer sensitive to soil background scattering effects (Bacour et al. 2002), bringing observed and modeled NDVI closer in agreement.

The time series of CCWC in figures 3.6 and 3.8 show a general agreement but differ in that CCWC is not maintained as constant throughout the reproductive growth stage like it was for modeled treatments 1-3 and treatment 5. There are a few weaknesses of the approach presented in this paper which may explain the differences. First, the modeled CCWC was generated following the assumption of a "container-like" soil profile during the soil water balance steps. In the model, no water was allowed to leave the soil profile through any path other than $ET_{c\ adj}$, which may have resulted in underestimated actual water lost to runoff or surface evaporation. This may also explain the relatively large disagreement between modeled CCWC in treatment 1 and the satellite-derived CCWC from Landsat-8 surface reflectance of all treatments during the onset of the reproductive period (difference of 0.27 x 10^3 g m^{-2} on July 29). Another possible source for the disagreement may be the error in ET_c calculations used to generate the treatments in the irrigation experiment. Crop water use in the irrigation experiment was estimated for the maize using the FAO-56 methods for calculating ET_c from local weather observations (Zhang et al. 2019). Uncertainty from the Penman-Monteith calculation of ET_o or estimated K_c, if underestimated, can lead to under watering crops if the goal is to strictly replace only the amount for water replacement. It is also possible for the irrigation pivot pressure sensor to misrepresent the actual amount of water being pumped (Fanning et al. 2001).

The modeled and satellite-derived yield ratio also showed general agreement (RMSE = 016). The biggest overall contrast between the modeled and satellite-derived yield ratio is the rate in which the modeled yield ratio decreases, particularly with treatment 4 during the reproductive stage. The yield ratio equation (eq. 8) is the cumulative product of daily water conditions throughout the time series, which results in a rapidly decreasing yield ratio during a series of days with poor water conditions, as was the case in the current study for the modeled yield ratio values. The FAO-56 soil water balance was performed assuming a daily average of water inputs and ET for each treatment during three growth phases. If the average daily ET was greater than the average daily water input (as was the case for each treatment except for the control treatment), the soil water profile decreased on a consistent daily time step. In reality, periods exist when the water input is greater than ET (irrigation or rainfall event) which

may allow the soil water content to recharge above the RAW threshold and stunt the decline of the yield ratio for the period. As a result, the modeled yield ratios are likely an underestimate of yield conditions in reality. Conversely, the satellite derived yield ratios are likely to be overestimated, as the current assumption of this approach is $K_s = 1$ in between Landsat-8 overpasses. A future expansion of this study to improve this method and converge both modeled and satellite-derived yield ratios towards the true yield ratio could be done in a couple of ways. First, the modeled yield ratio should be computed using daily records of water inputs and ET, instead of averaged daily values over entire growth stages, which should allow for the soil water balance to recharge for periods after a significant water event. Finally, a data assimilation technique, such as a Kalman filter (Welch and Bishop 1995), could be used to gap-fill the satellite-derived yield ratio time series using the modeled yield ratio time series. In this way, the yield ratio time series is driven by model inputs of watering, soil capacity, and ET, and then updated with satellite-derived estimates of the yield ratio when they become available.

This approach is not meant to replace the use of NDVI for yield estimation. In cases where drought is severe throughout the entire year, delayed or stunted crop development is easily detectable using NDVI and less computationally expensive than CCWC retrieval. Estimation of CCWC for deriving yield ratio can improve yield ratio prediction during seasons with late drought events after full vegetation development, which is a known weakness in yield estimation through NDVI. The overall strength of an approach which uses CCWC to estimate yield, opposed to empirical models based on vegetation indices, is in its transferability and ability to detect drought stress when the canopy is already fully developed. Retrieving the physical quantity of water in the canopy also allows for a direct physical link to the FAO-56 soil water balance, drought stress, and yield ratio equations to be made.

The demonstrated approach in this study is limited by the requirements of additional parameters K_c, K_y, and stage length for producing CCWC and yield estimates. The FAO-56 paper states that the parameters are known to vary between cultivars and regions (Allen et al. 1998b), which hinder the transferability of the approach. A current priority in further developing methods which use the FAO-56 soil water balance approach for yield estimation is to refine and archive the crop and site-specific coefficients (Jovanovic et al. 2020). Further research which assimilates phenology timing retrieval methods from optical data into this approach may improve the overall transferability, such as a satellited-derived LAI or DMC product which could be assimilated into the simple crop model. Finally, because no yield data were published in the Zhang et al. (2019) irrigation study, the method presented in this study needs to be tested under the configuration of a similar irrigation study with ground collected yield data.

Conclusions

In this study, we proposed and demonstrated an approach to estimate yield impact in late growth stage drought stressed maize of an independent irrigation experiment (Zhang et al. 2019) using satellite retrieved cropland canopy water content (CCWC) which was integrated into the FAO-56 crop water use framework. To our knowledge, this is the first study to establish a direct link between CCWC and drought stress to bridge the gap between CCWC and yield using FAO-56 definitions of drought stress, phenology, and yield. Information from FAO-56 tables, the irrigation experiment, and known relationships of biophysical parameters (Allen and Pereira 2009; Allen et al. 1998b; Beeri et al. 2020; Hosgood et al. 1995; Lemaire et al. 2007; Zhang et al. 2019) were used in concert to model CCWC, NDVI, and yield for each date of cloudless Landsat-8 Operational Land Imager (OLI) imagery over the irrigation study field. Coincident Landsat-8 OLI surface reflectances were inverted through PRO4SAIL using methods outlined in strategy 1 from Boren and Boschetti (2020) to estimate coincident CCWC for each treatment of the irrigation study and date. Using a previously established logistic relationship between leaf water content (LWC) and available soil water content (ASWC) (Zhou et al. 2021), satellite-derived CCWC was used to approximate the current soil water conditions, and through the FAO-56 crop water use approach, estimate the yield ratio at the 30 m pixel level.

The results indicated good general agreement of overall time series trends between modeled and estimated CCWC as well as modeled and observed NDVI. The expected change in modeled and satellited-derived CCWC was observed for each treatment throughout the growing season and demonstrated better detection ability than NDVI for differentiating between each treatment. Modeled and satellite-derived yield ratio using the CCWC time series showed the general expected patterns reflecting each irrigation treatment as well, although the underestimation in modeled yield ratio and overestimation of the satellite derived yield ratio may be present due to weaknesses of both approaches.

The main goal of establishing the first steps towards a novel approach to predict yield from satellite retrieved CCWC was achieved. Satellite derived CCWC has the potential to contribute to FAO-56 crop water use model development for yield ratio prediction, through bridging the gap between LWC and ASWC, and enabling the development of a field level 30 m FAO-56 derived yield ratio prediction. More research is needed to test the approach against field-level ground collected daily meteorological measurements and yield data under different irrigation treatments. Data assimilation techniques should also be explored to combine modeled FAO-56 yield ratio with the satellite derived yield ratio to gap fill information in between satellite overpasses.

References

Albergel, C., Rüdiger, C., Pellarin, T., Calvet, J.-C., Fritz, N., Froissard, F., Suquia, D., Petitpa, A., Piguet, B., & Martin, E. (2008). From near-surface to root-zone soil moisture using an exponential filter: an assessment of the method based on in-situ observations and model simulations. *Hydrology and Earth System Sciences, 12*, 1323-1337

Allen, R.G., & Pereira, L.S. (2009). Estimating crop coefficients from fraction of ground cover and height. *Irrigation Science, 28*, 17-34

Allen, R.G., Pereira, L.S., Raes, D., & Smith, M. (1998). Crop evapotranspiration-Guidelines for computing crop water requirements-FAO Irrigation and drainage paper 56. *Fao, Rome, 300*, D05109

Amprako, J.L. (2016). The United Nations World Water Development Report 2015. *Future of Food: Journal on Food, Agriculture and Society, 4*, 64-65

Atzberger, C. (2004). Object-based retrieval of biophysical canopy variables using artificial neural nets and radiative transfer models. *Remote sensing of environment, 93*, 53-67

Atzberger, C. (2010). Inverting the PROSAIL canopy reflectance model using neural nets trained on streamlined databases. *Journal of Spectral Imaging, 1*

Bacour, C., Baret, F., & Jacquemoud, S. (2002). Information content of HyMap hyperspectral imagery. In, *Proceedings of the 1st International Symposium on Recent Advances in Quantitative Remote Sensing, Valencia (Spain), 16* (pp. 503-508)

Beeri, O., Netzer, Y., Munitz, S., Mintz, D.F., Pelta, R., Shilo, T., Horesh, A., & Mey-tal, S. (2020). Kc and LAI Estimations Using Optical and SAR Remote Sensing Imagery for Vineyards Plots. *Remote Sensing, 12*, 3478

Berger, K., Atzberger, C., Danner, M., D'Urso, G., Mauser, W., Vuolo, F., & Hank, T. (2018). Evaluation of the PROSAIL model capabilities for future hyperspectral model environments: A review study. *Remote Sensing, 10*, 85

Boren, E.J., & Boschetti, L. (2020). Landsat-8 and Sentinel-2 Canopy Water Content Estimation in Croplands through Radiative Transfer Model Inversion. *Remote Sensing, 12*, 2803

Boyer, J.S. (1982). Plant productivity and environment. *Science, 218*, 443-448

Carlson, T.N., & Ripley, D.A. (1997). On the relation between NDVI, fractional vegetation cover, and leaf area index. *Remote sensing of environment, 62*, 241-252

Coleman, E., Dick, W., Gilliams, S., Piccard, I., Rispoli, F., & Stoppa, A. (2017). Remote Sensing for Index Insurance, Findings and Lessons Learned for Smallholder Agriculture. In: International Fund of Agricultural Development (IFAD)

Colombo, R., Meroni, M., Marchesi, A., Busetto, L., Rossini, M., Giardino, C., & Panigada, C. (2008). Estimation of leaf and canopy water content in poplar plantations by means of hyperspectral indices and inverse modeling. *Remote sensing of environment, 112*, 1820-1834

Darvishzadeh, R., Skidmore, A., Schlerf, M., & Atzberger, C. (2008). Inversion of a radiative transfer model for estimating vegetation LAI and chlorophyll in a heterogeneous grassland. *Remote sensing of environment, 112*, 2592-2604

Dinku, T., Ceccato, P., & Connor, S.J. (2011). Challenges of satellite rainfall estimation over mountainous and arid parts of east Africa. *International Journal of Remote Sensing, 32*, 5965-5979

Doorenbos, J., & Kassam, A. (1979). Yield response to water. *Irrigation and drainage paper, 33*, 257

Dorigo, W., Gruber, A., De Jeu, R., Wagner, W., Stacke, T., Loew, A., Albergel, C., Brocca, L., Chung, D., & Parinussa, R. (2015). Evaluation of the ESA CCI soil moisture product using ground-based observations. *Remote sensing of environment, 162*, 380-395

Duan, T., Chapman, S., Guo, Y., & Zheng, B. (2017). Dynamic monitoring of NDVI in wheat agronomy and breeding trials using an unmanned aerial vehicle. *Field Crops Research, 210*, 71-80

Easterling, W.E., Aggarwal, P.K., Batima, P., Brander, K.M., Erda, L., Howden, S.M., Kirilenko, A., Morton, J., Soussana, J.-F., & Schmidhuber, J. (2007). Food, fibre and forest products. *Climate change*, 273-313

Fanning, J.L., Schwarz, G.E., & Lewis, W.C. (2001). *A field and statistical modeling study to estimate irrigation water use at benchmark farms study sites in southwestern Georgia, 1995-96*. US Department of the Interior, US Geological Survey

Giménez, C., Gallardo, M., & Thompson, R.B. (2013). Plant–Water Relations☆. *Reference Module in Earth Systems and Environmental Sciences*: Elsevier

Grifoll, J., Gastó, J.M., & Cohen, Y. (2005). Non-isothermal soil water transport and evaporation. *Advances in water resources, 28*, 1254-1266

Grossman, Y., Ustin, S., Jacquemoud, S., Sanderson, E., Schmuck, G., & Verdebout, J. (1996). Critique of stepwise multiple linear regression for the extraction of leaf biochemistry information from leaf reflectance data. *Remote sensing of environment, 56*, 182-193

Hartpence, A. (2021). Landsat Collection 2. In: US Geological Survey

Hazaymeh, K., & Hassan, Q.K. (2016). Remote sensing of agricultural drought monitoring: A state of art review. *AIMS Environmental Science, 3*, 604-630

Hellmuth, M.E., Osgood, D.E., Hess, U., Moorhead, A., & Bhojwani, H. (2009). Index insurance and climate risk: Prospects for development and disaster management

Hosgood, B., Jacquemoud, S., Andreoli, G., Verdebout, J., Pedrini, G., & Schmuck, G. (1995). Leaf optical properties experiment 93 (LOPEX93). *European commision, joint research center, institute for remote sensing applications report EUR 16095 EN*

Jacquemoud, S., & Baret, F. (1990). PROSPECT: A model of leaf optical properties spectra. *Remote sensing of environment, 34*, 75-91

Jacquemoud, S., Verhoef, W., Baret, F., Bacour, C., Zarco-Tejada, P.J., Asner, G.P., François, C., & Ustin, S.L. (2009). PROSPECT+ SAIL models: A review of use for vegetation characterization. *Remote sensing of environment, 113*, S56-S66

Jaleel, C.A., Manivannan, P., Wahid, A., Farooq, M., Al-Juburi, H.J., Somasundaram, R., & Panneerselvam, R. (2009). Drought stress in plants: a review on morphological characteristics and pigments composition. *Int. J. Agric. Biol, 11*, 100-105

Jovanovic, N., Pereira, L., Paredes, P., Pôças, I., Cantore, V., & Todorovic, M. (2020). A review of strategies, methods and technologies to reduce non-beneficial consumptive water use on farms considering the FAO56 methods. *Agricultural water management, 239*, 106267

Lemaire, G., van Oosterom, E., Sheehy, J., Jeuffroy, M.H., Massignam, A., & Rossato, L. (2007). Is crop N demand more closely related to dry matter accumulation or leaf area expansion during vegetative growth? *Field Crops Research, 100*, 91-106

Li, J., & Heap, A.D. (2014). Spatial interpolation methods applied in the environmental sciences: A review. *Environmental Modelling & Software, 53*, 173-189

Li, P., & Wang, Q. (2011). Retrieval of leaf biochemical parameters using PROSPECT inversion: A new approach for alleviating ill-posed problems. *IEEE Transactions on Geoscience and Remote Sensing, 49*, 2499-2506

Magney, T.S., Eitel, J.U., Huggins, D.R., & Vierling, L.A. (2016). Proximal NDVI derived phenology improves in-season predictions of wheat quantity and quality. *Agricultural and Forest Meteorology, 217*, 46-60

Mahlstein, I., Knutti, R., Solomon, S., & Portmann, R.W. (2011). Early onset of significant local warming in low latitude countries. *Environmental Research Letters, 6*, 034009

Makaudze, E.M., & Miranda, M.J. (2010). Catastrophic drought insurance based on the remotely sensed normalised difference vegetation index for smallholder farmers in Zimbabwe. *Agrekon, 49*, 418-432

Marti, J., Bort, J., Slafer, G., & Araus, J. (2007). Can wheat yield be assessed by early measurements of Normalized Difference Vegetation Index? *Annals of Applied biology, 150*, 253-257

McKee, T.B., Doesken, N.J., & Kleist, J. (1993). The relationship of drought frequency and duration to time scales. In, *Proceedings of the 8th Conference on Applied Climatology* (pp. 179-183): Boston

Mekonnen, M.M., & Hoekstra, A.Y. (2016). Four billion people facing severe water scarcity. *Science advances, 2*, e1500323

Monteith, J.L. (1965). Evaporation and environment. In, *Symposia of the society for experimental biology* (pp. 205-234): Cambridge University Press (CUP) Cambridge

Mthembu, N.N., & Zwane, E.M. (2017). The adaptive capacity of smallholder mixed-farming systems to the impact of climate change: The case of KwaZulu-Natal in South Africa. *Jàmbá: Journal of Disaster Risk Studies, 9*, 1-9

Nelder, J.A., & Mead, R. (1965). A simplex method for function minimization. *The computer journal, 7*, 308-313

Ouyang, Y., & Zheng, C. (2000). Surficial processes and CO2 flux in soil ecosystem. *Journal of hydrology, 234*, 54-70

Palmer, W.C. (1965). *Meteorological drought*. US Department of Commerce, Weather Bureau

Palmer, W.C. (1968). Keeping track of crop moisture conditions, nationwide: the new crop moisture index

Pereira, L., Paredes, P., & Jovanovic, N. (2020). Soil water balance models for determining crop water and irrigation requirements and irrigation scheduling focusing on the FAO56 method and the dual Kc approach. *Agricultural water management, 241*, 106357

Pettorelli, N., Vik, J.O., Mysterud, A., Gaillard, J.-M., Tucker, C.J., & Stenseth, N.C. (2005). Using the satellite-derived NDVI to assess ecological responses to environmental change. *Trends in ecology & evolution, 20*, 503-510

Plénet, D., & Lemaire, G. (1999). Relationships between dynamics of nitrogen uptake and dry matter accumulation in maize crops. Determination of critical N concentration. *Plant and soil, 216*, 65-82

Raes, D., Geerts, S., Kipkorir, E., Wellens, J., & Sahli, A. (2006). Simulation of yield decline as a result of water stress with a robust soil water balance model. *Agricultural water management, 81*, 335-357

Rivera, J.P., Verrelst, J., Leonenko, G., & Moreno, J. (2013). Multiple cost functions and regularization options for improved retrieval of leaf chlorophyll content and LAI through inversion of the PROSAIL model. *Remote Sensing, 5*, 3280-3304

Rowley, R.J., Price, K.P., & Kastens, J.H. (2007). Remote sensing and the rancher: Linking rancher perception and remote sensing. *Rangeland Ecology & Management, 60*, 359-368

Sah, R., Chakraborty, M., Prasad, K., Pandit, M., Tudu, V., Chakravarty, M., Narayan, S., Rana, M., & Moharana, D. (2020). Impact of water deficit stress in maize: Phenology and yield components. *Scientific reports, 10*, 1-15

Skakun, S., Vermote, E.F., Roger, J.-C., Justice, C.O., & Masek, J.G. (2019). Validation of the LaSRC cloud detection algorithm for Landsat 8 images. *IEEE Journal of selected topics in applied earth observations and remote sensing, 12*, 2439-2446

Smith, M., & Steduto, P. (2012). Yield response to water: the original FAO water production function. *FAO Irrigation and Drainage Paper*, 6-13

Solomon, S., Qin, D., Manning, M., Chen, Z., Marquis, M., Averyt, K., Tignor, M., & Miller, H. (2007). IPCC fourth assessment report (AR4). *Climate change, 374*

Sperry, J.S., Adler, F., Campbell, G., & Comstock, J. (1998). Limitation of plant water use by rhizosphere and xylem conductance: results from a model. *Plant, Cell & Environment, 21*, 347-359

Srivastava, P.K., Petropoulos, G.P., & Kerr, Y.H. (2016). *Satellite soil moisture retrieval: techniques and applications*. Elsevier

Steduto, P., Hsiao, T.C., Fereres, E., & Raes, D. (2012). *Crop yield response to water*. Food and Agriculture Organization of the United Nations Rome

Sun, Q., Miao, C., Duan, Q., Ashouri, H., Sorooshian, S., & Hsu, K.L. (2018). A review of global precipitation data sets: Data sources, estimation, and intercomparisons. *Reviews of Geophysics, 56*, 79-107

Turvey, C.G., & Mclaurin, M.K. (2012). Applicability of the Normalized Difference Vegetation Index (NDVI) in index-based crop insurance design. *Weather, Climate, and Society, 4*, 271-284

Verger, A., Baret, F., & Camacho, F. (2011). Optimal modalities for radiative transfer-neural network estimation of canopy biophysical characteristics: Evaluation over an agricultural area with CHRIS/PROBA observations. *Remote sensing of environment, 115*, 415-426

Verhoef, W. (1984). Light scattering by leaf layers with application to canopy reflectance modeling: the SAIL model. *Remote sensing of environment, 16*, 125-141

Verhoef, W., Jia, L., Xiao, Q., & Su, Z. (2007). Unified optical-thermal four-stream radiative transfer theory for homogeneous vegetation canopies. *IEEE Transactions on Geoscience and Remote Sensing, 45*, 1808-1822

Wagner, W., Lemoine, G., & Rott, H. (1999). A method for estimating soil moisture from ERS scatterometer and soil data. *Remote sensing of environment, 70*, 191-207

Welch, G., & Bishop, G. (1995). An introduction to the Kalman filter

Yavuz, D., Seymen, M., Yavuz, N., Çoklar, H., & Ercan, M. (2021). Effects of water stress applied at various phenological stages on yield, quality, and water use efficiency of melon. *Agricultural water management, 246*, 106673

Yebra, M., Dennison, P.E., Chuvieco, E., Riaño, D., Zylstra, P., Hunt, E.R., Danson, F.M., Qi, Y., & Jurdao, S. (2013). A global review of remote sensing of live fuel moisture content for fire danger assessment: Moving towards operational products. *Remote sensing of environment, 136*, 455-468

Yi, Q., Wang, F., Bao, A., & Jiapaer, G. (2014). Leaf and canopy water content estimation in cotton using hyperspectral indices and radiative transfer models. *International Journal of Applied Earth Observation and Geoinformation, 33*, 67-75

Zarco-Tejada, P.J., Rueda, C., & Ustin, S. (2003). Water content estimation in vegetation with MODIS reflectance data and model inversion methods. *Remote sensing of environment, 85*, 109-124

Zhang, C., Pattey, E., Liu, J., Cai, H., Shang, J., & Dong, T. (2017). Retrieving Leaf and Canopy Water Content of Winter Wheat Using Vegetation Water Indices. *IEEE Journal of selected topics in applied earth observations and remote sensing*

Zhang, F., & Zhou, G. (2019). Estimation of vegetation water content using hyperspectral vegetation indices: A comparison of crop water indicators in response to water stress treatments for summer maize. *BMC ecology, 19*, 18

Zhang, L., Zhang, H., Niu, Y., & Han, W. (2019). Mapping maize water stress based on UAV multispectral remote sensing. *Remote Sensing, 11*, 605

Zhou, H., Zhou, G., He, Q., Zhou, L., Ji, Y., & Lv, X. (2021). Capability of leaf water content and its threshold values in reflection of soil–plant water status in maize during prolonged drought. *Ecological Indicators, 124*, 107395

Table 3.1. Applied irrigation treatments for each treatment 1-5 for each growth stage. The range of dates with the observed growth stages are shown under the growth stage. The amounts are in [mm] with the percent of treatment 1 shown in parentheses.

Treatment	Late Vegetative 7/4 - 7/28	Reproductive 7/29 - 8/20	Maturation 8/21 - 9/7	Total
TRT 1	188 (100%)	132 (100%)	82 (100%)	402
TRT 2	158 (84%)	128 (97%)	43 (52%)	329
TRT 3	158 (84%)	125 (95%)	43 (52%)	326
TRT 4	158 (84%)	91 (69%)	23 (28%)	272
TRT 5	158 (84%)	124 (94%)	82 (100%)	365

Table 3.2. Landsat-8 OLI Scene information.

Date	Path	Row
June 11	128	32
June 20	127	32
July 13	128	32
July 29	128	32
August 7	127	32
August 14	128	32
August 30	128	32

Table 3.3. Parameterization for PRO4SAIL model LUT generation. The asterisked values are the means retrieved from maize leaf measurements from the LOPEX93 dataset (Hosgood et al. 1995).

Model Parameters	Symbol	Units	Parameter values
Leaf Parameters PROSPECT-5			
Leaf chlorophyll content	C_{cab}	µg/cm2	41.42 *
Leaf carotenoid content	C_{car}	µg/cm2	8.47 *
Water thickness	C_w	cm	Input Parameter
Dry matter content	C_m	g/cm^2	Input Parameter
Leaf structure index	N_s	-	1.5
Canopy variables 4SAIL			
Leaf area index	LAI	m^2/m^2	Input Parameter
Average leaf angle	ALA	degree	Erectophile
Soil coefficient	αsoil	unitless	1 (dry soil)
Hot spot parameter	HotS	m/m	0.01
Solar zenith angle	θs	degree	25
View zenith angle	θv	degree	0
Sun-sensor azimuth angle	φ	degree	0

Table 3.4. Seasonal phenology period descriptions, Ky coefficient values and days since planting (DSP). The sources for information are shown in the source column.

Period Designation	Period	DSP	Value	Source
A	Planting	0	--	Zhang et al. (2019)
B	Emergence	12	--	"
C	Kc ini ends	25	--	FAO Irrigation Paper No. 56
D	Flowering	70	--	Zhang et al. (2019)
E	Yield formation begins	79	--	FAO Irrigation Paper No. 56
F	Maturity begins	92	--	Zhang et al. (2019)
G	Harvest	110	--	"
I	Vegetative Ky	0 - 69	0.4	FAO Irrigation Paper No. 56
II	Flowering Ky	70-78	1.5	"
III	Yield Formation Ky	79-91	0.5	"
IV	Ripening Ky	92-110	0.2	"

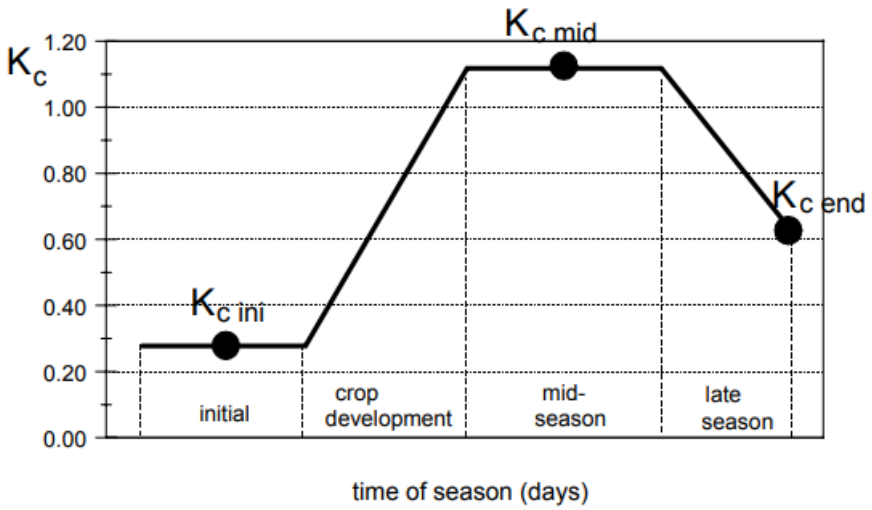

Figure 3.1. An example K_c curve of an annual crop during the growing season. Initial, crop development, mid-season, and late-season growth periods are shown with respective K_c values. The figure was taken from Allen et al. (1998).

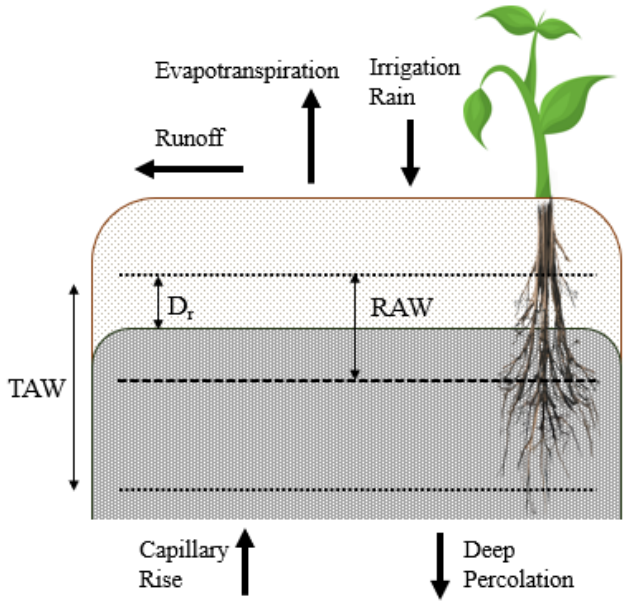

Figure 3.2. Conceptual diagram of soil water balance water flow as described in Allen et al. (1998). The light shaded area represents soil and dark shaded area represents the water level in the soil profile. TAW, RAW, and Dr are the total water availability, readily available water, and depletion, respectively.

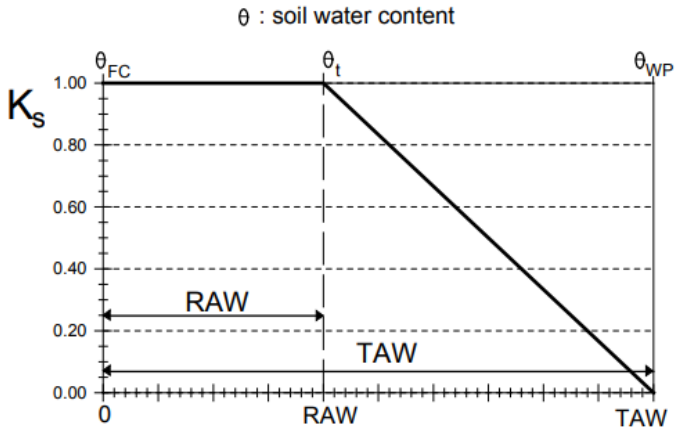

Figure 3.3. K_s coefficient relationship with water level between $D_r = 0$ and $D_r = 1$. θ_{FC}, θ_t, and θ_{WP} represent the field holding capacity, readily available water threshold, and wilting point, respectively. The figure was taken from Allen et al. (1998).

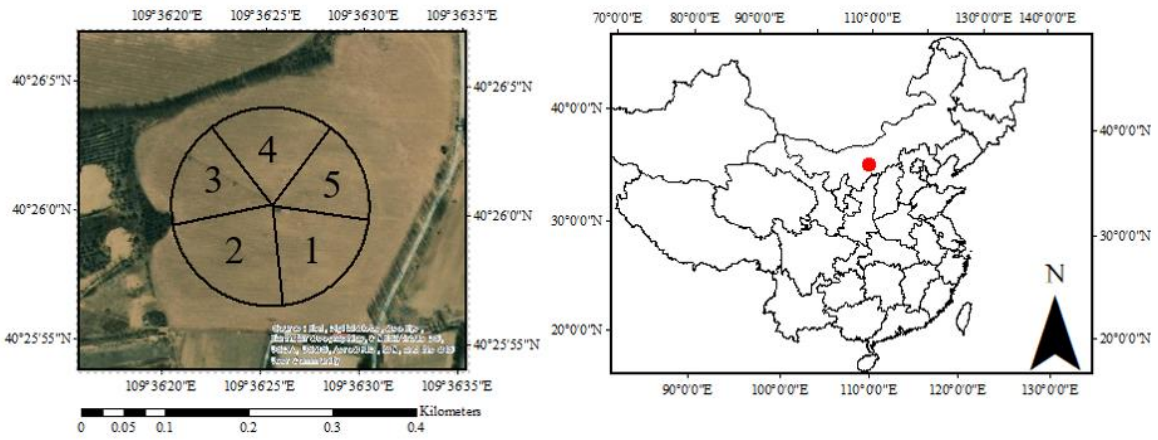

Figure 3.4. Irrigation study field within Inner Mongolia, China (Zhang et al. 2019). The approximate location of the experimental field is shown with the red dot on the map on the right. The map on the left shows the aerial view of the experimental treatment field with approximate delineation of each treatment, numbered 1-5. Treatments for 1-5 are shown in table 3.1.

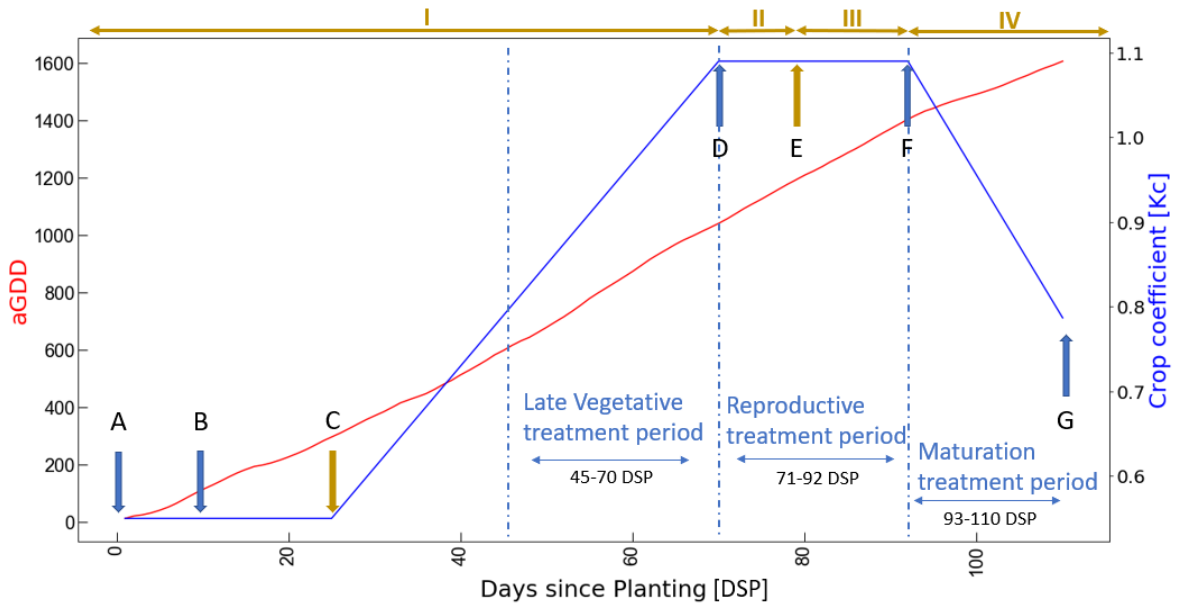

Figure 3.5. Plotted K_c curve (blue) and aGDD (red) against days since planting (DSP) for the 2017 growing season in the irrigation experiment. Blue arrows signify information that was taken from the independent irrigation study paper (Zhang et al. 2019). Gold arrows signify information taken from the FAO Irrigation and Drainage paper 56. Roman numerals and letters are the period designation keys for table 3.4.

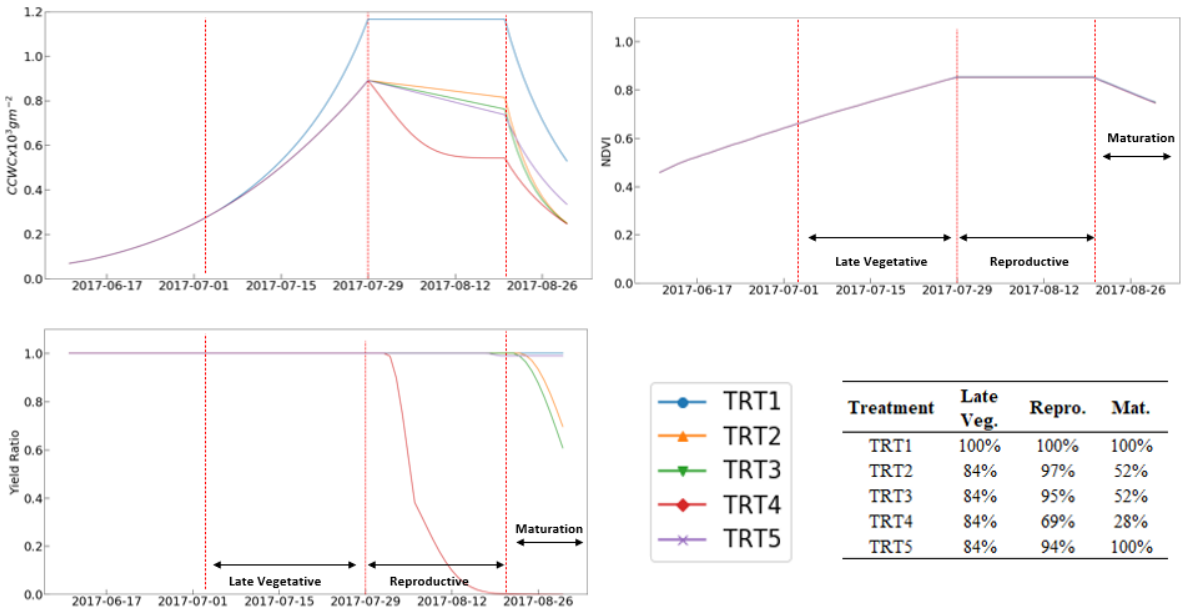

Treatment	Late Veg.	Repro.	Mat.
TRT1	100%	100%	100%
TRT2	84%	97%	52%
TRT3	84%	95%	52%
TRT4	84%	69%	28%
TRT5	84%	94%	100%

Figure 3.6. Modeled daily CCWC (upper left), NDVI (upper right), and yield ratio (bottom left). The symbology is presented in the legend for each treatment 1-5. The table (lower right) shows the irrigation treatment percentage of treatment 1 (TRT1) reported in Zhang et al. (2019) for each growth period. The range of growth periods are represented using the dashed red lines on the plots.

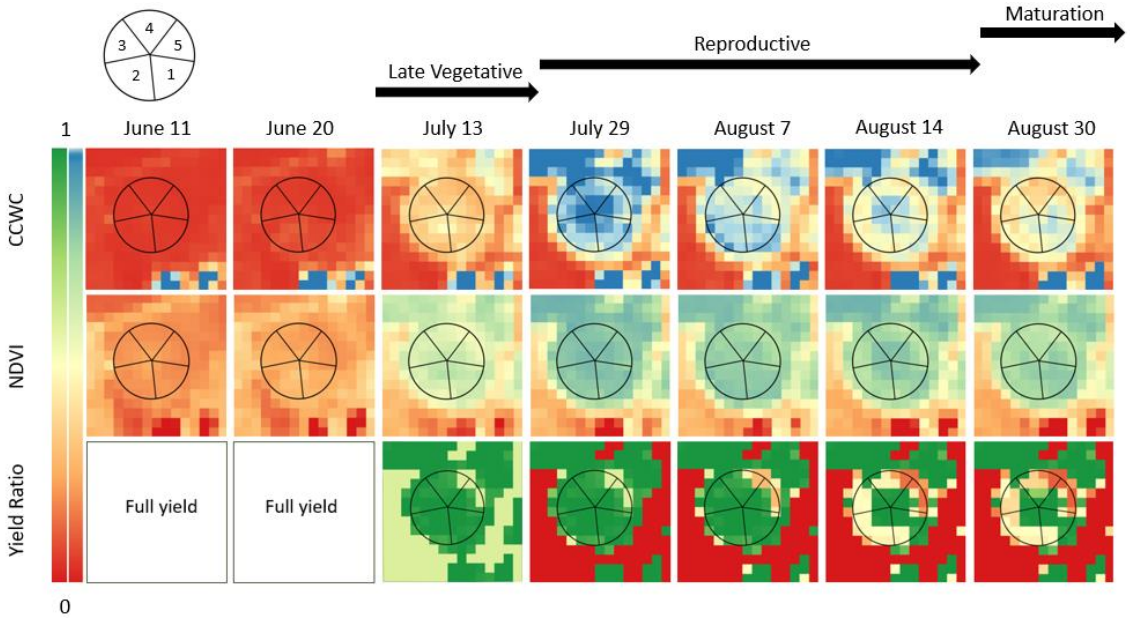

Figure 3.7. Estimated CCWC [10^3 g m^{-2}] (red to blue) (top row), observed NDVI [unitless] (red to blue) (middle row), and estimated yield ratio [unitless] (red to green) (bottom) for the study irrigation pivot. The approximate delineated treatment boundaries are shown in the upper left hand of the figure. The arrows above present the period of growth for the experimental treatments.

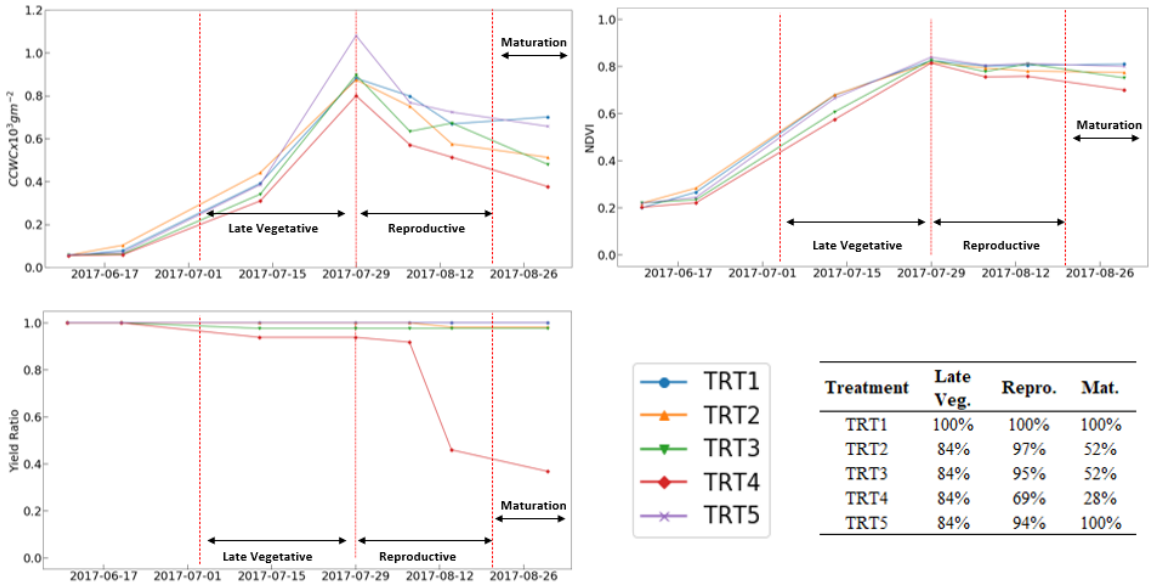

Treatment	Late Veg.	Repro.	Mat.
TRT1	100%	100%	100%
TRT2	84%	97%	52%
TRT3	84%	95%	52%
TRT4	84%	69%	28%
TRT5	84%	94%	100%

Figure 3.8. Estimated CCWC (upper left), observed NDVI (upper right), and estimated yield ratio (bottom left) for points each Landsat-8 overpass date. The symbology is presented in the legend for each treatment 1-5. The table (lower right) shows the irrigation treatment percentage of treatment 1 (TRT1) reported in Zhang et al. (2019) for each growth period. The range of growth periods are represented using the dashed red lines on the plots.

Conclusion

A drought is characterized as a period where a deficit of water is experienced relative to normal conditions. Water availability restricts agricultural productivity more than any other factor (Boyer 1982), therefore research that seeks to improve scalability of methods for agricultural drought monitoring is of paramount importance. The presented research has demonstrated the feasibility of using scalable remote sensing data and techniques in PRO4SAIL inversion (Jacquemoud et al. 2009) for estimating cropland canopy water content (CCWC) at the temporal and spatial resolution required for effective cropland monitoring. Our research also established a well-characterized link between CCWC and the Food and Agricultural Organization (FAO) Irrigation and Drainage paper 56 (Allen et al. 1998) definition of yield ratio which may be used to predict yield loss in crops, even during late drought conditions after the canopy has reached full and un-inhibited development. The main objective of the research, therefore, has been achieved: contribute research towards the first steps of a novel approach to estimate yield ratio changes from physical-based and moderate spatial resolution EO-data derived CCWC.

A step-wise approach was carried out to achieve the research goal of this dissertation: 1) assess the variation of the leaf structure parameter (N_s) as a function of phenology and irrigation and to provide *a priori* information to improve inversion of PROSPECT, 2) propose and test a methodology which uses phenology, species type, and a number of other biophysical and canopy constraints for generating a multi-temporal CCWC product from inverting a time series of the Harmonized Landsat-Sentinel (HLS) product through PRO4SAIL, and 3) develop the first steps towards a method which links CCWC to the FAO-56 framework for predicting yield ratio using a previously established relationship between leaf water content (LWC) and available soil water content (ASWC) (Zhou et al. 2021).

The hypothetical N_s parameter is one of the largest sources of uncertainty for inverting the leaf level model, PROSPECT, because it is the only parameter which does not represent a biophysical quantity (Ceccato et al. 2001; Ollinger 2011). The results from the leaf-level inversion experiment (Chapter 1) showed a significant relationship between crop species type and phenology with N_s. To our knowledge, this was the first detailed phenology dependent record of N_s for both monocotyledon and dicotyledon leaves. The research in Chapter 1 also illustrated that irrigation regime did not impact N_s, which provided important evidence that crop water status and the N_s parameter are independent from one another. Further data collection should be done to include a wider range of crop species in both monocotyledon and dicotyledon plant types, as the study was limited to four plant species. A continuation of research can also be done to test whether constraining the range of variation of N_s can

reduce uncertainty in retrieving leaf level variables from PROPSECT inversion of hyperspectral data, which may advance research in non-invasive leaf sampling techniques.

The lessons that phenology and crop species type may be able to improve inversion of PRO4SAIL for CCWC estimation was tested in Chapter 2. The inversion of PRO4SAIL for CCWC estimation was improved from an RMSE of 0.58 x 10^3 g m^{-2} to 0.46 x 10^3 g m^{-2} when including information about growth timing difference between species types and resulted in the first HLS-based CCWC product generated through radiative transfer model inversion. The most constrained approach also resulted in a regression slope, intercept, and coefficient of determination of 0.78, 0.07, and 0.76, respectively, which demonstrates potential in the retrieval of CCWC using HLS surface reflectance. Constraining N_s for canopy level inversions did not improve the inversion of PRO4SAIL, confirming previously published outcomes from a PRO4SAIL parameter sensitivity analysis (Jacquemoud et al. 2009). A major benefit of the field data collected for validation in Chapter 2 is the record of biophysical parameters encompassing the full phenological cycle of multiple crops, which enabled the assessment of inversion results throughout the entire growing season. It is recommended that future research is done to examine the inversion during early and late phenological growth stages through soil reflectance constraining strategies and consider ranges of the average leaf angle (ALA) parameter for each growth stage.

In the final chapter, the relationship between CCWC and yield ratio was established using FAO-56 crop water use definitions and a previously published relationship between LWC and ASWC (Zhou et al. 2021). The theoretical link between CCWC and yield ratio was evaluated using published information of an independent irrigation experiment in Inner Mongolia, China. The research demonstrated the first steps towards a 30 m yield ratio product which can be produced at any time during the growing season. A time series analysis of satellite derived CCWC estimates and NDVI from Landsat-8 also showed that CCWC was more sensitive to the different irrigation treatments of the experiment, which created drought stress conditions during late vegetative, reproductive, and maturation stages in maize and strengthened evidence that NDVI is ineffective to detect drought stress during late drought events. The study is limited in that a daily average of water inputs and ET was used to model CCWC and yield for each treatment period, which ignores the possibility of soil water recharge during watering events. The satellite derived yield ratio was also limited in that days between overpasses were ignored during the cumulative yield computation, which may contribute to an overestimation of yield. The results of chapter 3 should be used as the preliminary justification for a follow-up study which repeats the analysis using daily meteorological measurements and yield data to

test the FAO-56 yield ratio framework, and then assimilate satellite derived CCWC into the modeled yield ratio time series to produce a 30 m yield ratio map of the experimental field. The implications that CCWC may be able to be integrated into the FAO-56 framework would enable integration of remotely sensed conditions of surface characteristics, thereby enabling field-level yield prediction meeting the spatial requirements for agricultural monitoring.

Considering the findings of each chapter in this dissertation, research is recommended to 1) widen the representation of crop species in published biophysical leaf measurements datasets, including representation of leaf measurements taken throughout early, middle, and late growth stages, and 2) test the link between CCWC and yield ratio in maize through validation with ground measured yield. Limited published data exists which characterize the biophysical properties of a plant throughout the growing season. The research from this dissertation has demonstrated that leaf and canopy properties have a significant relationship with phenology, and the independent data which is used to characterize the *a priori* information used to constrain PRO4SAIL inversion should include phenology. A large-scale field experiment study with water treatment control, meteorological measurements, comprehensive leaf and canopy measurements through the season, and ground measured yield, would also be beneficial for improving inversion of PRO4SAIL for CCWC estimation and testing the link proposed in this dissertation for a yield ratio prediction.

References

Allen, R.G., Pereira, L.S., Raes, D., & Smith, M. (1998). Crop evapotranspiration-Guidelines for computing crop water requirements-FAO Irrigation and drainage paper 56. *Fao, Rome, 300*, D05109

Boyer, J.S. (1982). Plant productivity and environment. *Science, 218*, 443-448

Ceccato, P., Flasse, S., Tarantola, S., Jacquemoud, S., & Grégoire, J.-M. (2001). Detecting vegetation leaf water content using reflectance in the optical domain. *Remote sensing of environment, 77*, 22-33

Jacquemoud, S., Verhoef, W., Baret, F., Bacour, C., Zarco-Tejada, P.J., Asner, G.P., François, C., & Ustin, S.L. (2009). PROSPECT+ SAIL models: A review of use for vegetation characterization. *Remote sensing of environment, 113*, S56-S66

Ollinger, S. (2011). Sources of variability in canopy reflectance and the convergent properties of plants. *New Phytologist, 189*, 375-394

Zhou, H., Zhou, G., He, Q., Zhou, L., Ji, Y., & Lv, X. (2021). Capability of leaf water content and its threshold values in reflection of soil–plant water status in maize during prolonged drought. *Ecological Indicators, 124*, 107395